Analyse, conception et contrôle de robots collaboratifs

Thèse

Jérôme Landuré

Doctorat en génie mécanique
Philosophiæ doctor (Ph. D.)

Québec, Canada

Analyse, conception et contrôle de robots collaboratifs

Thèse

Jérôme Landuré

Sous la direction de:

Clément Gosselin, directeur de recherche

Résumé

Le projet derrière cette thèse porte sur l'amélioration des conditions de travail des ouvriers sur les chaînes d'assemblage. Une équipe de Général Motors est venue à notre rencontre avec la problématique que les ouvriers sur leurs chaînes d'assemblage doivent souvent adopter des postures inconfortables lors de l'exécution de certaines tâches. Répétées de nombreuses fois, ces postures peuvent engendrer des problèmes de santé sur le long terme. Une solution proposée pour pallier à ce problème est de permettre à l'ouvrier d'effectuer son travail depuis une zone éloignée de la zone d'assemblage, où il ne devrait pas adopter de postures gênantes et pourrait être isolé de bruits, chaleurs ou dangers induits par la proximité avec la chaîne d'assemblage. Pour faire le lien entre cette zone sécuritaire et la zone de travail, la solution d'un robot a été proposée. Cette thèse présente le travail effectué pour concevoir ce robot.

Cette thèse est composée de quatre chapitres qui sont autant d'articles abordant chacun un sujet différent. Le chapitre 1 porte sur deux types d'assemblages courant, en fait l'analyse et propose des solutions pour mécaniser ces tâches. Un outil est conçu et testé dans le cas des clips aussi appelés 'snap-fit'. Des stratégies de trajectoire et l'usage de mécanismes vibrants sont explorés pour l'insertion de tuyaux. Les phases de test et de mesure sont présentées en vidéo.

Dans le chapitre 2, la notion de difficulté d'accomplir une tache de loin est abordée. En effet, la distance augmente considérablement la concentration et la perception nécessaires à un opérateur humain pour accomplir une tâche d'assemblage, résultant en un échec ou au moins un temps d'exécution plus grand et donc une efficacité moindre. Les mécanismes de correction de précision sont donc abordés. Des solutions impliquant l'usage de ressorts sont tout d'abord présentées pour permettre aux mécanismes d'être compliants tout en maintenant une position neutre définie. Ces solutions ont pour particularité d'introduire des seuils de force pour activer la compliance qui garantissent un comportement du mécanisme prévisible dans une utilisation générale. Puis, la notion de correction de position est introduite au travers de la famille de mécanismes des *Remote Centre of Compliance* (RCC) que l'on peut traduire par centre de mobilité distant. Différentes architectures en rotation et en translation sont présentées pour proposer des alternatives au RCC plus adaptées au contexte de travail avec un opérateur humain. Des tests sont effectués et une vidéo appuie la démonstration.

Après la conception des mécanismes passifs, le plan du projet était de se tourner vers des solutions actives. La recherche d'une architecture adaptée aux besoins a mené à l'élaboration du chapitre 3. Ce dernier présente une architecture de robot parallèle à six degrés de liberté de type 6-PUS. La cinématique du robot est étudiée, puis une méthode analytique de détermination de son espace de travail géométrique est présentée. Une étude de ses lieux de singularité et de ses capacités en force complète son analyse. Même si cette architecture ne fut pas celle retenue pour le prototype, les méthodes développées pour cette architecture furent utilisées pour la conception du robot fabriqué.

Après de multiples itérations, une architecture pour le robot actif fut choisie. Cette dernière est présentée au chapitre 4 et s'accompagne de la présentation de trois schémas de contrôle développés pour répondre à la problématique. Les étapes de conception développées dans le chapitre 3 sont présentées au préalable. Le premier schéma de contrôle exploré est un contrôle en position, qui sert de base au contrôle du robot et permet de développer et valider les outils essentiels au bon contrôle du robot. Le second schéma de contrôle introduit des concepts présentés dans les architectures passives précédentes, en présentant l'avantage d'être reconfigurable au besoin. Un modèle simulant le comportement d'un RCC est d'ailleurs présenté. Le dernier schéma de contrôle exploré introduit de la vision numérique. Un marqueur ARUCO est placé sur le robot et les informations qu'il fournit sont incluses et traitées dans le schéma de contrôle. L'objectif est de simuler un environnement où le robot peut détecter de façon efficace et indépendante les positions des pièces à assembler et ajuster en temps réel les erreurs de positionnement de l'opérateur humain.

Abstract

The project behind this thesis is about improving the working conditions of workers on assembly lines. A research team from General Motors came to us with a problem to work on: the workers on their assembly lines must use body postures that are difficult to bear when performing some tasks. These postures can become health hazards because of the repetitive nature of their work. The proposed solution to this problem is to make the operator work in a safe remote area from the assembly area, where he can keep a comfortable posture and remain far from the potential hazards of the assembly line. To make the link between the safe area and the assembly area, the solution of using a robot has been suggested. This thesis presents the work accomplished to design such robot.

This thesis is composed of four chapters, each corresponding to an article dealing with a different subject. Chapter 1 deals with two different types of assembly tasks, presents their analysis and discusses solutions to introduce mechanisms in their process. A tool is designed and tested to perform snap-fit assembly tasks. Motion strategies are explored as well as vibrating mechanisms to deal with hose assembly tasks. Test phases and data measurements are presented in a video.

In chapter 2, the issues associated with performing a task remotely are raised. Indeed, distance enhances greatly the required concentration and perception for a human operator to perform the task, resulting in a failure or a greater operating time, reducing productivity. Therefore, the accuracy correction mechanisms were considered. First, solutions with springs are presented to design compliant mechanisms that return to a neutral configuration when unloaded. These solutions bring the originality to introduce force thresholds to keep the compliance passive when not needed. Then, accuracy correction mechanisms are introduced through RCC mechanisms. Several rotational and translational mechanisms adapted to human collaboration are presented. Tests to validate the concept are shown in a video.

After the design of passive mechanisms, the scope of the project turned to active solutions. The search for an effective architecture led to the contents of chapter 3. It presents a six-degree-of-freedom 6-PUS parallel robot. The kinematic analysis of the robot is presented, followed by an algorithm to determine the geometrical workspace of the robot. A singularity locus analysis and a force capability analysis are then presented. Even if this architecture

was not selected in the end, the methods developed were used for the design of the final architecture.

After several iterations, an architecture was chosen for the active robot. This architecture is presented in chapter 4. After a design process based on the work shown in chapter 3, three control schemes are presented. The first one is a classical position control which is a requisite for more advanced schemes. The second control scheme introduces concepts previously raised with the passive mechanisms discussed in chapter 2. The model simulates a RCC mechanism with the advantage of being reconfigurable without hardware modifications. The last control scheme introduces computer vision. An ARUCO marker is placed on the robot and the information it provides are injected in the control scheme. The objective is to simulate an environment where the robot detects the pose of the parts to assemble and adjusts itself in real time to compensate for the errors of the human operator.

Table des matières

Liste des tableaux

Liste des figures

À ma famille, aux beaux jours à venir...

Être libre, ce n'est pas pouvoir faire ce que l'on veut, mais c'est vouloir ce que l'on peut.

Jean-Paul Sartre

Remerciements

Ce sont de longues études qui s'achèvent ici, longues dues à une part d'indécision et d'appréhension du futur combinée à un cadre de vie étudiant agréable. Je tiens à remercier mes parents pour leur soutien permanent et leur patience. Les études longues retardent l'entrée dans le monde du travail et sont souvent mal comprises, mais elles apportent une diversité de profils essentielle sur le marché du travail qui pousse à l'innovation et au progrès.

Je remercie Clément, mon superviseur de recherche et directeur du laboratoire de robotique, pour son aide précieuse dans l'exercice compliqué de la recherche et sa supervison efficace. Travailler avec Clément fut une expérience formatrice et très plaisante.

Je remercie les membres de chez General Motors que j'ai côtoyés, en particulier Muhammad, pour l'expérience de projet en entreprise que j'ai reçue.

Je tiens aussi à remercier tout particulièrement Thierry et Simon, pour leur aide précieuse avec laquelle la fabrication de pièces, l'utilisation des logiciels du laboratoire, ainsi que les précieux conseils et toutes les petites aides quotidiennes qui sont si précieuses.

Enfin, je remercie les membres du laboratoire de robotique, avec qui j'ai passé beaucoup de mon temps à Québec. Je garderai un bon souvenir de ces instants.

Le COVID-19 me laisse tout de même un goût amer, un sentiment d'inachevé et d'année gâchée qui je pense est partagé avec beaucoup d'autres personnes. Pour tout dire, j'ai pensé à plusieurs reprises cette année que je ne verrais jamais un dénouement heureux à mon doctorat, mais je suis content de m'être trompé. Ainsi, je souhaite remercier tous ceux qui m'ont aidé de prêt ou de loin à terminer cette aventure par une fin heureuse.

Avant-propos

La thèse présentée ici est sous la forme d'une thèse par article. Il est donc nécessaire de donner le statut des articles en date du dépôt de la thèse ainsi que ma contribution à chacun d'eux. Pour une lecture plus efficace, les informations relatives à chaque chapitre, c.-à-d., chaque article, sont données en points de forme.

— Chapitre 1 :
Titre : *Modelling and development of assistive tools for the assembly of press-fit components*
Type d'article : Article de journal, Proceedings of the Institution of Mechanical Engineers, Part B : Journal of Engineering Manufacture
Statut : soumis le 14/08/2020
Contribution : Auteur principal. Écriture, conception et expérimentation faites par l'auteur principal.
Coauteurs : Prof. Clément Gosselin a supervisé activement la réalisation et la finalité de cet article. Thierry Laliberté à supervisé la conception de l'impacteur et est le premier à avoir travaillé sur les mécanismes de force retour avec seuil présentés dans l'article. Muhammad E. Abdallah a fourni des informations importantes sur le contexte de travail sur les chaînes d'assemblage et a contribué lors de rencontres sur le projet.

— Chapitre 2 :
Titre : *Modelling and development of passively adaptive assistive tools for the assembly of press-fit components*
Type d'article : Article de journal, Journal of Mechanical Design
Statut : soumis le 14/08/2020
Contribution : Auteur principal. Écriture, conception et expérimentation faites par l'auteur principal. **Coauteurs** : Prof. Clément Gosselin a supervisé activement la réalisation et la finalité de cet article. Thierry Laliberté a supervisé la conception des différents mécanismes présentés dans l'article et a conçu l'attache du tuyau utilisée dans la dernière partie de la vidéo de démonstration de l'article. Muhammad E. Abdallah a fourni des tuyaux utilisés dans la vidéo et est à l'origine de l'intérêt pour les RCC utilisés

pour la base de l'étude présentée dans l'article.

— Chapitre 3 :
Titre : *Kinematic and workspace modelling of a 6-$\underline{P}$US parallel mechanism*
Type d'article : Article de conférence, ASME 2018
Statut : Publié, 02 Novembre 2018
Contribution : Auteur principal. Écriture, conception et expérimentation faites par l'auteur principal.
Coauteurs : Prof. Clément Gosselin a supervisé activement la réalisation et la finalité de cet article.

— Chapitre 4 :
Titre : *Synthesis and prototyping of a 6-dof parallel mechanism for the automatic performance of assembly tasks*
Type d'article : Article de journal, Journal of Robotics and Mechatronics
Statut : soumis le 14/08/2020
Contribution : Auteur principal. Écriture, conception et expérimentation faites par l'auteur principal. **Coauteurs** :Prof. Clément Gosselin a supervisé activement la réalisation et la finalité de cet article. Thierry Laliberté a activement supervisé la conception du prototype de robot présenté dans l'article. Muhammad E. Abdallah a contribué aux idées présentées pour l'élaboration des schémas de contrôle du robot.

Introduction

Contexte et problématique générale

Contexte

Actuellement un nombre non négligeable de pièces dans les chaînes d'assemblage des véhicules chez General Motors sont assemblées dans des conditions qui sont peu ergonomiques pour les opérateurs. En effet, les obstacles et les espaces qui permettent l'accessibilité aux endroits d'assemblage sont souvent des sources de difficultés pour les ouvriers car ils les obligent à prendre des postures peu confortables ou aux limites de leur portée, ce qui complique l'application des efforts nécessaires pour effectuer l'assemblage. L'objectif de ce projet de doctorat est de concevoir un robot collaboratif conçu comme extension de la capacité de travail des ouvriers sur les chaînes d'assemblage. Suite à plusieurs entrevues avec des représentants du département recherche de GM, plusieurs tâches d'assemblage particulièrement problématiques ont été identifiées : les habillages clipsés ou 'snap-fit', les tuyaux insérés puis verrouillés par un collier de serrage, les bougies, les connecteurs électriques et les modules boulonnés. Il a été décidé de séparer le travail en deux grandes parties : la conception d'un manipulateur passif, peu encombrant et léger mais focalisé sur une tâche principale, puis la conception d'un manipulateur actif qui remplit plusieurs tâches de façon modulaire, au détriment d'une complexité accrue ainsi que d'un certain nombre de compromis à identifier.

L'objectif est de concevoir un robot d'assistance sur les chaines de montage automobiles. La figure 0.1 montre la chaine de montage GM à Fairfax qui est un environnement typique pour l'intégration du robot.

Défis

La conception du robot suit des contraintes qui ne sont pas définies entièrement, ce qui laisse de la liberté de choix mais implique un travail supplémentaire sur l'établissement des performances recherchées. Par exemple le volume, la masse ou l'espace de travail du mécanisme sont très libres. Les contraintes majeures définies à ce jour concernent l'environnement dans lequel le robot doit être implanté ainsi que les performances actuelles des opérateurs. Les tâches d'assemblage sont actuellement effectuées à la main, les pièces à assembler sont donc

FIGURE 0.1 – Chaine de montage GM à Faifax (US).

fabriquées et les processus d'assemblage conçus pour être utilisés à la main. Ceci comprend les formes des pièces prévues pour être agrippées, l'espace laissé près des zones d'assemblage ainsi que le processus d'assemblage. Par exemple les connecteurs électriques se montent en les poussant sur la fiche d'insertion jusqu'à un point où une came dans le connecteur autorise l'actionnement d'un levier qui termine et verrouille le montage. Ce mouvement est simple à effectuer avec des mains mais la plupart des outils de préhension utilisés par des robots ne possèdent pas la dextérité nécessaire à la bonne exécution de cette tâche. De plus l'espace disponible pour la main et surtout les doigts est petit, ce qui ne facilite pas l'utilisation d'un mécanisme. Comme tout robot opérant en environnement industriel, les solutions sensibles à la poussière, à faible durée de vie, trop complexes d'utilisation ou potentiellement dangereuses pour les humains évoluant autour sont à éviter.

Objectifs de recherche

1. Établissement d'un modèle général
   1.1. Choix et conception des mécanismes
   1.2. Fabrication de prototypes
   1.3. Tests dans des contextes vraisemblables et validation
2. Développer un prototype de mécanisme collaboratif passif
   2.1. Peu ou pas d'éléments actifs
   2.2. Ergonomique et dédié à une partie des tâches seulement
3. Développer un prototype de mécanisme collaboratif actif

3.1. Plus général que le passif

3.2. Introduit des concepts plus poussés dans son shéma de contrôle comme la vision numérique

Méthodologie et plan de la thèse

Les principaux objectifs du projet portent sur l'élaboration de mécanismes conçus pour répondre à des besoins. La première étape du projet est donc d'analyser ces besoins pour explorer des pistes de solutions potentielles. Les premiers travaux seront donc de délimiter le cadre de recherche à quelques tâches d'assemblage, et de se concentrer sur une à la fois pour tenter d'apporter une solution satisfaisante dans son contexte particulier. Les analyses seront visuelles principalement, se reposeront sur du contenu fourni par General Motors et des pièces jugées représentatives du contexte des lignes d'assemblage. Des capteurs seront aussi utilisés pour appuyer les observations par des données. Une recherche bibliographique sur des études sur des pièces impliquées dans des tâches d'assemblage aidera sûrement à collecter des informations complémentaires.

Une première étape de conception commencera alors en se basant sur les observations obtenues. L'objectif sera de concevoir le mécanisme passif spécifié dans la commande du projet. Pour ce faire, un travail sur le comportement voulu du mécanisme ainsi qu'une étape de conception rapide sous un logiciel de conception seront nécessaires pour alimenter les discussions qui permettront au projet de converger vers une architecture spécifique. Une nouvelle recherche bibliographique pourra aussi donner des idées de solutions potentielles. Plusieurs itérations seront sûrement nécessaires pour obtenir un résultat satisfaisant. Les données obtenues lors de la phase précédente se révéleront particulièrement utiles au moment de dimensionner les différents éléments du mécanisme.

La fabrication du mécanisme passif sera suivie de phases de test. Des ajustements de conception seront sans doute nécessaires à ce moment là.

Ensuite, le projet se concentrera sur la conception du mécanisme actif. Les étapes de discussions préliminaires mentionnées précédemment reprendront et seront sans doute plus longues du fait de la complexité accrue attendue de la part d'un mécanisme actif par rapport à un mécanisme passif. Les discussions et recherches devraient aboutir à la fabrication d'un robot suffisamment générique dans ses possibilités pour permettre d'explorer différents schémas de contrôle. La dernière étape du projet portera sur le contrôle du robot. Le contrôle développé devra simuler des comportements crédibles dans le contexte des chaînes d'assemblage et répondre à des problématiques soulevées lors des phases de discussion.

Chapitre 1

Modelling and development of assistive tools for the assembly of snap-fit and press-fit components

1.1 Résumé

Cet article fut écrit à partir des travaux préliminaires du projet sur certaines des tâches d'assemblage visées. Cet article présente l'étude de deux types de tâches d'assemblage, les 'snap-fit', des assemblages par déformations locales, et les insertions de tuyaux. Des données et analyses des assemblages 'snap-fit' sont présentées et utilisées pour la conception d'un outil conçu dans le but de réaliser ces tâches simplement pour permettre des utilisations impliquant le minimum d'implication de la part d'un opérateur humain. Le travail de conception de l'outil est présenté ainsi que des tests qui valident son fonctionnement. Ensuite, les assemblages de tuyaux sont analysés dans le but de trouver des moyens de faciliter ce type de tâche. Pour ce faire, un capteur d'effort six-axes est utilisé. Une première approche fut de considérer différents mouvements lors de l'insertion du tuyau test et de mesurer leur impact sur les mesures de force. Une seconde approche est aussi présentée, cette fois-ci en utilisant un pot vibrant dans le but de mesurer l'impact des vibrations lors de l'exécution de la tâche.

1.2 Abstract

This article studies two types of assembly tasks, snap-fit and hose insertions. Data and analysis of a snap-fit assembly are used to design a tool that can manage the snap-fit task effectively. The design process of the tool is presented as well as tests to validate its effectiveness. Data are collected in order to find easier means to perform hose assembly tasks : a motion primitive strategy is first explored, followed by a vibration oriented strategy. A video recording of the data measurements is presented at the end.

1.3 Introduction

Assembly is a major part of the tasks performed in the industrial manufacturing. Although assembly is still often performed manually, actuated mechanisms are more and more being introduced to improve quality and productivity while decreasing the human effort required and ease the task of human operators. This work is part of a more global research initiative that aims at developing assistive devices to help operators to perform assembly tasks. Tools and devices to handle the parts to assemble is a major challenge in the project. Grippers (for example Kang and Wen (2006); Guo et al. (2017)) and position and orientation correcting mechanisms are considered. Among the existing architectures, six-degree-of-freedom architectures such as the one proposed in Abtahi et al. (2008) are often considered for their high dynamic output to reach fast reactivity. Monsarrat and Gosselin (2001) presents an interesting architecture, especially for the absence of prismatic joints. Carretero et al. (2000) presents a compact architecture where all the actuators are placed on fixed frames. Machining architectures are also interesting for their robustness, for instance Zoppi et al. (2010); Bi and Jin (2011) present very rigid mechanisms.

This work presents a design analysis and an experimental validation of tools for snap-fit and press-fit type assembly tasks. Snap-fit and press-fit are a class of assembly tasks which consist in the elastic deformation of at least one of the components that ensures a proper link between the parts involved based on their shape. Therefore, performing this kind of assembly requires to cross the elastic deformation energy threshold of the deformed parts, which can be measured and gives reasonably reliable data to guarantee the success of consecutive tasks. Many articles deal with snap-fit assembly tasks such as Luscher et al. (1998) where a model to describe snap-fit assembly motions is proposed, Baek et al. (2006) explores methods to use snap-fit assemblies for microscopic objects, Rónai and Szabó (2020) investigates a method to perform a snap-fit task on a battery with a robot and an adequate use of a force sensor. This paper is structured as follows. Section 1.4 describes the snap-fit assembly task used as an example task in this work. Section 1.5 investigates the mechanics of snap-fit tasks using the concepts of energy and momentum. An impactor designed to perform snap-fit assembly is proposed in Section 1.6 and analyzed in Section 1.7. A prototype of the impactor is described in Section 1.8 and experimental validation is presented in Section 1.9. Section 1.10 discusses the press-fit insertion of hoses, a second example task used in the paper. A strategy based on motion primitives for the insertion of hoses is proposed and illustrated in Section 1.11 while Section 1.12 investigates the use of vibrations to perform such insertions. A video demonstrating the concepts presented in the paper is introduced and commented in Section 1.13 and conclusions are drawn in Section 1.14.

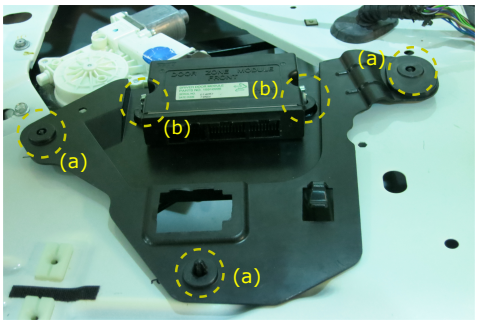

FIGURE 1.1 – Example of snap-fit assembly. The areas where the deformations occur are shown with the dashed-line circles. (a) indicates the 'Christmas trees' used to mount the trim on the car's door and (b) indicates the 'Christmas trees' used to mount additional electric components.

1.4 Snap-fit assembly tasks

The parts chosen to illustrate the snap-fit assemblies are shown in Figure 1.1. The black coloured plastic part assembles on the white painted metal part underneath it through three 'Christmas tree' shaped plastic modules. This assembly is mounted on a car door and is a support for the control sensors and motors of the window. The Christmas trees used for the assembly are the two on the top on each side and the one in the bottom, indicated with the letter '(a)' in Figure 1.1. In this picture, the two at the top correspond to an incomplete assembly, the tree not having crossed the trim, and the one at the bottom corresponds a complete assembly, the tree being entirely visible. Two other snap-fits are visible at the top middle (indicated with the letter '(b)' in Figure 1.1), they are used to mount another part on top of the trim whose purpose is to carry other electric components for the actuation. The trees are metallic in this case and do not require the same force to be deformed but their behaviour is the same as the plastic ones.

The second part of this article deals with hose assembly tasks. Specific devices to help perform hose assembly tasks can be found for instance in Jahanian et al. (2003). Because the task of inserting hoses appeared more challenging than snap-fit tasks, a deeper analysis is performed before diving into the design of a tool, and the result of this analysis is presented here. Measurements for assembly tasks can be found in Godin et al. (2008) for example. The problem of finding appropriate insertion motions, as presented in Grieshaber et al. (2009), could be very beneficial for robots because they can efficiently produce consistent motions that makes a good motion strategy even so more important.

Wang et al. (2014); Grieshaber and Armstrong (2007) study the force perception during a hose insertion for ergonomic purposes. These works have provided inspiration for the approach proposed in this paper.

1.5 Characterization of insertion tasks

Preliminary work for the design of a device to achieve insertion tasks consists in identifying the main parameters that affect the performance of the assembly. Two different fundamental quantities are considered in this analysis, namely momentum and mechanical energy. Momentum is often used to analyze collision problems in order to predict the kinematic behaviour of the bodies involved. Indeed, in a closed system with an inertial frame, the total momentum of the bodies in the system is the same before and after the collision (conservation of momentum). Since the insertion is performed using collisions, it can be assumed that momentum is conserved. The second quantity that is used in the analysis is mechanical energy. Although energy is not necessarily conserved in a collision, this concept can be used to infer the behaviour of a mechanical system. Also, assuming conservation of energy provides useful approximations. In order to investigate the relevance of these two concepts in an insertion operation, an example of a press fit insertion is studied. The two parts are represented schematically in Figure 1.4. The conical part is commonly referred to as a 'Christmas tree' component, to be inserted (press fit) into the hole of the second part, referred to as the 'trim to assemble'. As a first experiment, the conical component is placed over the hole and objects of known mass are dropped on it from a measured height until the height is sufficient to perform the insertion. Three different round shaped objects are used. It is assumed that all the potential energy of the dropped object is transferred to the part to cross the elastic deformation energy threshold. The equations used to compile the experimental results are the following :

$$v_i = 0 \tag{1.1}$$

$$v_f = \sqrt{2gh} \tag{1.2}$$

$$q = mv_f \tag{1.3}$$

$$e_k = \frac{1}{2}mv_f^2 \tag{1.4}$$

$$e_g = mgh \tag{1.5}$$

with v_i and v_f the initial velocity of the dropped object and its velocity at impact, q the momentum of the dropped mass at impact, e_k the kinetic energy at impact, h the height from which the mass m is dropped, g the gravitational acceleration and e_g the initial potential energy of the mass. As mentioned above, three different masses were used to verify whether the results are consistent. For a same mass, the minimal successful height — the height from which the insertion is successfully performed — is consistent for several trials and, as expected, the larger the mass, the lower is the required height. Figure 1.2 shows the linear momentum required to perform the insertion under different conditions (different holes and different masses). Variations are noticeable, indeed the momentum model is valid in a friction-free system which explains why the measured value is not consistent. Figure 1.3 shows the potential energy requi-

red to perform the assembly, for the same tasks and the same masses. It can be observed that the results are more consistent, giving more credibility to the energy based model. Therefore, the concept of energy was used as a design tool in this work.

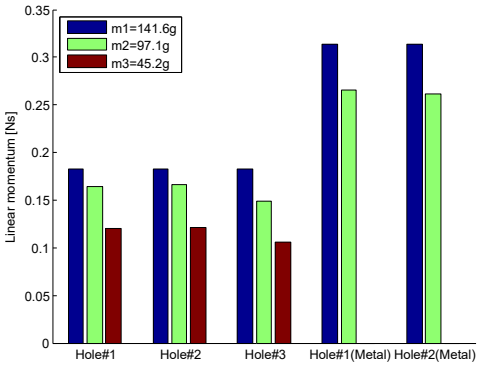

FIGURE 1.2 – Estimation of the linear momentum involved during a snap-fit insertion for 5 different assembly items (referred to as holes on the graph) and 3 different objects (3 different masses).

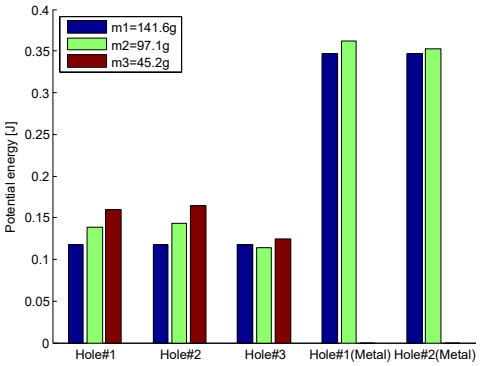

FIGURE 1.3 – Estimation of the energy involved during a snap-fit insertion for 5 different assembly items (referred to as holes on the graph) and 3 different objects (3 different masses).

1.6 Kinematic principle of the assistive impactor

In industry, the insertion of snap-fit components is commonly done by hand (thumb pressed) or using wooden or rubber hammers. Such tasks induce ergonomic stress on the operators. The objective of this work is to design a tool that can be used to reduce the ergonomic stress, provide better controlled assembly conditions and be eventually transferable to automated work. The ergonomic tool is referred to as an impactor. Similar work on tolls to lessen ergonomic stress can be found in Wu et al. (2016).

Using simple components such as springs, a large impact force can be generated from a reasonably low torque. This approach is taken here. The design of the tool is based on the impact

tests reported in the preceding section. Indeed, it was shown that producing impacts on one of the parts with sufficient energy is a feasible approach to perform the insertion. Moreover, since not all tasks require the same amount of energy, it is useful to be able to adjust the energy of the impact.

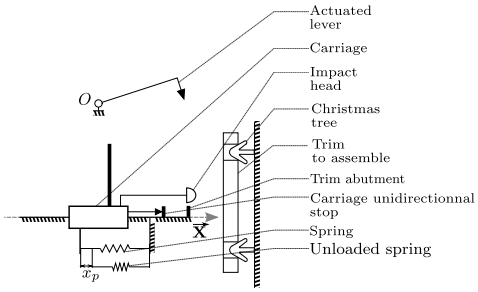

FIGURE 1.4 – Schematic representation of the impactor device and the parts involved in a snap-fit assembly task.

Figure 1.4 shows the main components of the device. The actuated lever revolves around point O and is the input motion of the mechanism. The carriage slides along the X axis. The continuous rotation motion of the lever produces an intermittent translational motion of the carriage whose operation is described in Figure 1.5.

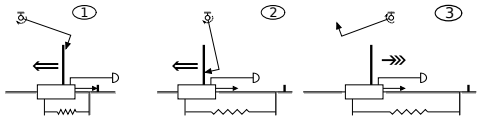

FIGURE 1.5 – Successive phases of a working cycle of the impactor device.

The operation of the device can be described as follows. During the first step, the lever comes in contact with the carriage. Then, during step 2, this new interaction makes the carriage move backward and extend the spring. Finally, during step 3, the contact between the carriage and the lever is lost and the energy stored in the spring is released and moves the carriage back to its initial position with a high velocity, thereby generating the impact.

1.7 Mechanical analysis of the impactor

The impactor was designed to achieve two main goals, namely, to provide a source of energy close to the task to be performed — and possibly far from the human operator — and to generate forces that are large enough to overcome the static force threshold, i.e., the minimum force required to perform the task. Powerful actuators are needed to directly produce the force threshold required for typical insertions. However, such actuators tend to be heavy and bulky, which is an issue in the design of assistive tools, where light and compact solutions must be

favoured. Therefore, spring mechanisms are used in this work to produce large forces, possibly at the expense of a longer execution time (time needed to accumulate energy in the spring).

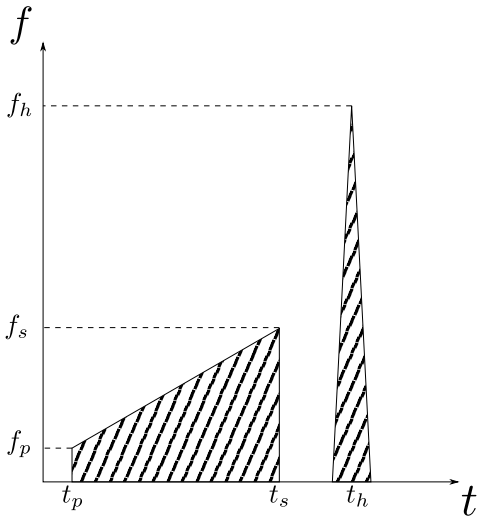

FIGURE 1.6 – Representation of the forces applied on the carriage over time.

The force profiles of the linear force required to crank the carriage and the linear force delivered by the release of the spring are represented in Figure 1.6. f_p is the preload force, f_s is the maximum force applied by the spring and f_h is the impact force. The dashed areas represent respectively the energy stored in the spring during the crank phase and the energy released during the impact phase. In a frictionless environment, these energies are equal.

Basically, the system described above stores potential energy in the spring and releases it by letting the spring free to return to its initial state. For the example task described above, the targeted value of the stored energy is $0.11J$, which corresponds to the energy measured during the collision tests for the three plastic holes (see Figure 1.3). To reach this goal, one must choose the correct stiffness and stroke for the spring. For the case described above, considerations on the impact lead us to choose a 50 mm stroke. Indeed, the impact is applied to the trim because it is the mobile part and on the experimental test set-up, the displacement of the trim has been measured to be approximately 10 mm. Ideally, the impact must occur when the spring reaches its initial state when all the potential energy has been converted to kinetic energy. However, in order to drive the part until the end of the insertion, the device is designed for the spring to reach its initial state at the end of the insertion instead of at the beginning. This consideration leads us to choose a stroke which minimizes the loss of transferred energy, which is why a stroke of 5 times the driving length has been chosen. Indeed, the velocity of the mobile part follows a sinusoidal behaviour and as demonstrated below the speed and kinetic energy are very close to their maximum value with such a choice (see the computations reported after Equation 1.15). Then, the stiffness of the spring must be chosen. Another parameter, noted

x_p, which represents a preload length of the spring, is introduced as an adjustment parameter. The stroke parameter, noted x_s, represents the maximum elongation of the spring during its working cycle. The expression of the stored energy can be derived as :

$$E = \int_{x_p}^{x_s+x_p} kxdx \tag{1.6}$$

$$= \frac{1}{2}k((x_s + x_p)^2 - x_p^2) \tag{1.7}$$

$$= \frac{1}{2}kx_s(x_s + 2x_p) \tag{1.8}$$

and then :

$$k = \frac{2E}{x_s(x_s + 2x_p)} \tag{1.9}$$

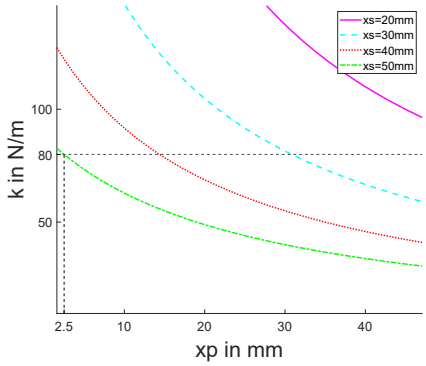

FIGURE 1.7 – Ideal spring stiffness as a function of the required preload for an energy $E = 0.11J$ and different strokes.

Figure 1.7 shows the stiffness computed from Equation 1.9 for a stored energy of $0.11J$ with different strokes as a function of the required preload. The graph shows that shorter strokes quickly increase the stiffness needed to unreasonable values, validating the $50mm$ stroke chosen earlier. Then, for a chosen stroke, and for given available stiffnesses, the ideal preload can be determined from the graph. For example, for the case represented in Figure 1.7, if a stiffness of $80N/m$ is selected (available spring) together with a $50mm$ stroke, the preload found from the graph is approximately $2.5mm$.

In practice, the following approach can be used to choose a spring. First, Equation 1.9 is used to compute the stiffness with $x_p = 0$. Then, the closest lower value of stiffness commercially available is selected and the preload is adjusted accordingly. For instance here, with a value of $x_p = 0$ and with $x_s = 50mm$, Equation 1.9 yields :

$$k = \frac{2 \times 0.11}{0.05 \times (0.05 + 2 \times 0)} \tag{1.10}$$

$$= 88\,N/m \tag{1.11}$$

We choose 80 N/m which is the closest lower stiffness available and set the preload to :

$$x_p = \frac{1}{2}\left[\frac{2E}{kx} - x\right] \tag{1.12}$$

$$= 2.5mm \tag{1.13}$$

which corresponds to the dashed lines in Figure 1.7. In the current design, the preload is set by the choice of the attachment points of the spring. On Figure 1.8, 4 attachment points can be seen on the carriage and 2 on the fix part.

This mechanism simulates successive hits similar to a mallet used by a human operator. Therefore, some information must be gathered on the hit frequency. The operation of the mechanism involves three different phases discussed before and represented in Figure 1.5. To be functional, the lever must not interfere with the carriage during its return motion induced by the spring. This represents an upper limit for the impact frequency. Indeed, such an interference happens if the lever is fast enough compared to the time spent for the carriage to make the hit. The dynamics of the spring-loaded carriage can be represented as

$$m\frac{d^2x}{dt^2} + kx = 0 \tag{1.14}$$

with m the mass of the mobile mass, k the stiffness of the spring, x the position of the carriage and its origin 0 the position where the spring is unloaded. Solving this equation yields

$$x\,(t) = x_i \cos(\omega t) \tag{1.15}$$

with x_i the position where the lever lets the carriage go and

$$\omega = \sqrt{\frac{k}{m}}. \tag{1.16}$$

Taking the derivative of Equation 1.15 with respect to time yields an expression for the velocity. Then, solving Equation 1.15 for ωt and substituting in the velocity equation, one has

$$v = v_{max} \sin\left(\arccos\left(\frac{x_p}{x_i}\right)\right). \tag{1.17}$$

As mentioned above, this equation can be used to justify the choice of the stroke. In the example discussed above, we have

$$v = v_{max} \sin\left(\arccos\left(\frac{1}{5}\right)\right) = 0.98 v_m ax \tag{1.18}$$

which is very close to the maximum value.

Returning to the issue of the operation frequency, based on Equation 1.15, the largest displacement that the carriage can undergo in this phase is from its initial position to when it

reaches the mechanical stop. This situation happens when the impactor works free of target and it corresponds to the longest time that this phase can last. From Equation 1.15, one has

$$t_f = \frac{1}{\omega} \arccos\left(\frac{x_p}{x_i}\right). \tag{1.19}$$

With the numerical values given in the example discussed above, one has

$$= \frac{1}{23.1} \arccos\left(\frac{0.0025}{0.0525}\right) \tag{1.20}$$

$$= 0.0660\,s. \tag{1.21}$$

As mentioned above, one critical limit of this design is that if the lever rotates too fast for the spring, the carriage as a chance to hit the lever instead of the part to assemble, which would waste the energy stored in the spring, defeating the purpose of the design.

During the time that the carriage makes the impact, the lever must travel around 180° before reaching the carriage again. Hence, if it is desired to prevent the carriage from hitting the lever during the release phase of the spring, it must be ensured that the lever does not travel more than half a turn, i.e.,

$$\theta_f = \omega t_f \leq \pi \tag{1.22}$$

which limits the maximum working frequency of the input to

$$f \leq \frac{1}{2t_f} = 7.6\,Hz. \tag{1.23}$$

1.8 Prototyping

The CAD model of a prototype of an impactor designed and built as part of this work is shown in Figure 1.8 and a photograph of the prototype is shown in Figure 1.9. The prototype can be operated manually or using an actuator. Indeed, the version of the prototype shown in the figures includes a handle for manual operation but the handle can easily be replaced with an actuator. All the parts of the prototype are made of 3D-printed ABS plastic except for the spring, the screws and especially a ball bearing carriage and its guide rail which yield a low friction motion and determine the overall size of the device.

As mentioned above, the device stores the energy for the impact in the extended spring. However, the prototype does also store gravitational potential energy due to the movement of the sliding impact head whose mass is not negligible. Depending on the orientation in which the device is used, the effect of gravity is different. For example, impacting upwards reduces

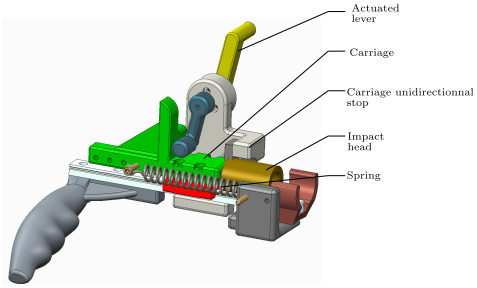

FIGURE 1.8 – Computer Assisted Design (CAD) model of the impactor with major components identified.

the energy of the impact because a portion of the potential energy stored in the spring is used to move the impact head upwards while impacting downwards increases the impact energy for the opposite reason. Other orientations yield results that are comprised between these two extreme cases. In the prototype, the mass of the impact head (moving mass) is 72 grams, which leads to a maximum energy loss/gain of :

$$E = mg\Delta h \tag{1.24}$$

$$= 0.072 \times 9.81 \times 0.05 \tag{1.25}$$

$$= 0.035\,J \tag{1.26}$$

This value is not negligible compared to the $0.11J$ required for the insertion completion.

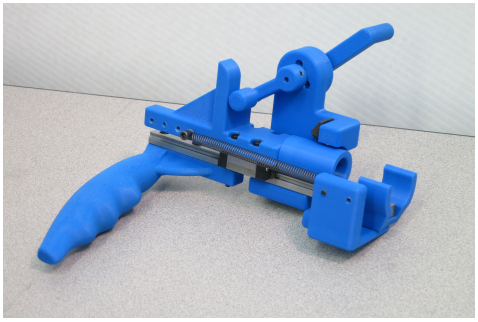

FIGURE 1.9 – Photograph of the 3D printed impactor.

1.9 Experimental validation

A video demonstrating the operation of the device is discussed in Section 1.13.

It should be noted that, when operating the device manually, the impact is barely noticed by the user, because the reaction force is mostly transferred in the axis of the prismatic joint. Therefore, the reaction force displaces the carriage backwards, which is compensated for by the spring.

1.10 Press-fit assembly of deformable hoses

The second type of assembly task addressed in this paper is the hose assembly. Many challenges appear when inserting a hose over a cylindrical shape. The flexibility of the hose can be an issue during the operation. Hoses are often used for their great expansion rate to make them fit in a wide variety of positions but this comes at the cost of many potential behaviours that make the design of a tool with limited movements to perform the task with a high success rate more difficult.

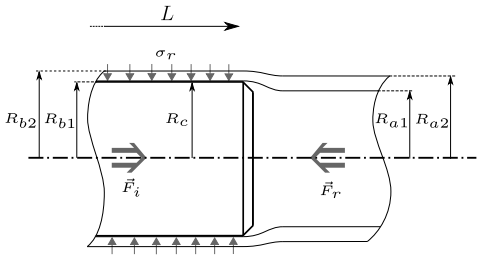

FIGURE 1.10 – Modelling of the hose assembly for the determination of the required insertion force.

Figure 1.10 presents a simple model to estimate the the axial force behaviour. The goal is to help validate the data measured in the next section. According to observations, to reach a sustainable hose assembly, the objects to assemble must be rigid and larger than the hose. Therefore, when an object is being inserted in the hose, the hose is deformed and as a result of its elastic material properties, it applies a pressure on the object. The goal is to generate an input force F_i strong enough to overcome the resistive force F_r. R_{a1} and R_{a2} are respectively the inner and outer radius of the hose before deformation. Similarly, R_{b1} and R_{b2} are respectively the inner and outer radius of the hose after deformation. R_c is the radius of the object being inserted, L the length of the object already inserted and σ_r is the pressure resulting of the deformation of the hose. Based on the fact that R_{b1} is matching R_c to wrap the object and on the fact that the volume of the hose is conserved before and after deformation, one obtains

$$R_{b1} = R_c \tag{1.27}$$

$$R_{b2} = \sqrt{R_c^2 + R_{a2}^2 - R_{a1}^2}. \tag{1.28}$$

The pressure applied by the hose on the object depends mostly on the elastic behaviour of the hose characterized by its Young modulus E, and the relative radial deformation of the hose ϵ_r. The resulting pressure σ_r is

$$\sigma_r = E\epsilon_r. \tag{1.29}$$

The radial deformation is the dimension variation of the hose in the radial direction. With e_i and e_f the undeformed and deformed thickness of the hose, one can write

$$\epsilon_r = \frac{e_f - e_i}{e_i} = \frac{(R_{b2} - R_{b1}) - (R_{a2} - R_{a1})}{(R_{a2} - R_{a1})} \tag{1.30}$$

which yields this expression for the resistive force,

$$F_r = \mu \times \sigma_r \times S = \mu E \epsilon_r 2\pi R_c L \tag{1.31}$$

$$= \frac{2\pi\mu E L R_{b1} \left[(R_{b2} - R_{b1}) - (R_{a2} - R_{a1})\right]}{(R_{a2} - R_{a1})}. \tag{1.32}$$

This means that the resistive force in the axis of the hose linearly increases with the length inserted, with a rate dependent on the parameters introduced above. To verify this assumption, a test setup composed of a plastic hose, a 3D printed insert and a six-axis force sensor is designed. The set-up is the one shown in Figure 1.19 without the piezo actuator in the centre. The values of the parameters are widely dependent on the objects involved, their material and shapes and thus does not provide general results on the hose behaviour. Therefore, the main focus is to search for the expected linear behaviour. The data for a straight forward push to insert the hose is shown in the graph in the right side of Figure 1.20. Considering the task was performed manually with a rather constant insertion speed, the linear behaviour measured here tends to support the linear behaviour assertion and validate the model of Equation 1.32.

1.11 Assembly strategies based on relative motion primitives

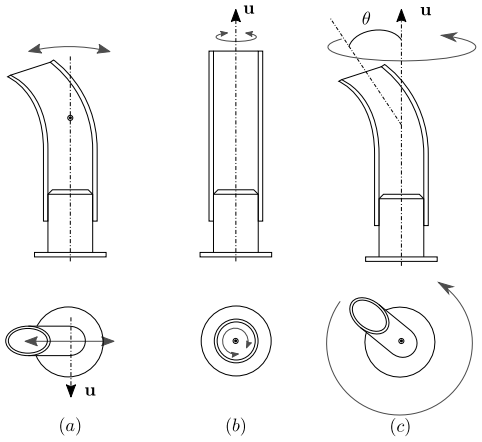

FIGURE 1.11 – Schematic representation of the relative motion primitives for insertion. For each motion, **u** is the direction of the axis of rotation. (a) is the shake, (b) the twist and (c) the vortex. the difference between (b) and (c) lies in the angular offset θ used in (c).

The assembly of hoses is generally difficult when attempted with a straight forward motion in the axis of the hose. It is the most instinctive method to perform the insertion due to the

basic shapes involved. However, after many trials on real hoses, it is also instinctive to try different methods of insertion that seem more optimal, meaning that the total required force is lessen. The test setup described above is used to verify this assumption. Six different motion primitives are executed while performing the insertion and the sensor is used to collect data. The selected motions are : shake, twist and vortex, each for a lower speed/frequency and a higher one. Figure 1.11 illustrates these motions. The shake is a periodic rotational motion whose axis is orthogonal to the axis of the cylinder. The twist is a periodic rotation motion whose axis is along the axis of the cylinder. The vortex motion is also a periodic rotation motion whose axis is along the axis of the cylinder, but for which the hose is given an initial offset angle.

Figure 1.12 shows the data measured during a straight forward insertion. The Z axis is the revolution axis of the hose and, as expected the maximum required force is along this axis. For this particular hose and insert, a force of approximately $50N$ is required to perform the assembly. It can be clearly observed in Figure 1.20, on the plot on the right, which is a measurement of the force along the Z axis with a straight forward insertion at a scale tuned to observe the maximum force reached during the straight forward motion. Figure 1.12 and Figures 1.13 to 1.18 are kept on a same scale to facilitate comparisons and the chosen scale favours the observation of data on the Z axis up to $-25N$ to get a clear view of the majority of measurements because they all fit in this scale except the straight forward data.

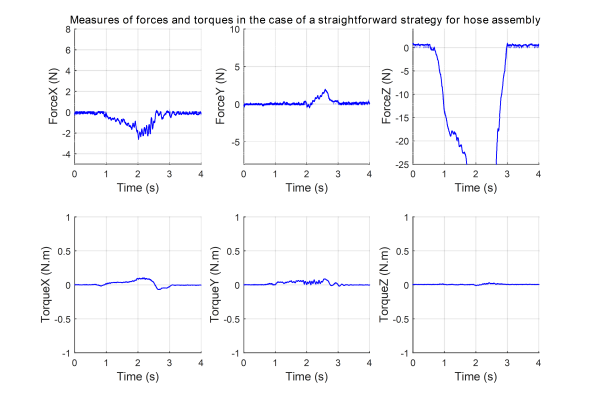

FIGURE 1.12 – Output of the ATI mini 45 - six-axis force sensor during a straight forward insertion of a hose/insert assembly.

The test process for the measures is to perform the assembly task with a similar effort in a similar span of time. Figure 1.12 serves as a reference to compare other results.

Figure 1.13 shows the sensor output while performing the insertion with a high-amplitude shake motion. The shake motion is a back and forth rotational motion around an axis on the plane orthogonal to the hose's axis. The video referenced at Section 1.13 shows an example of this motion. The shake motion creates oscillations of the X and Y forces with rather small

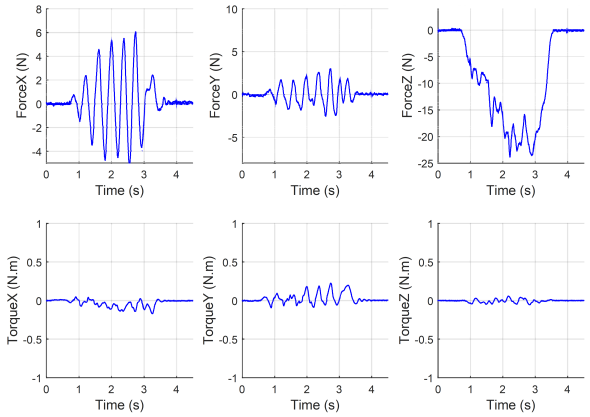

FIGURE 1.13 – Output of the ATI mini 45 - six-axis force sensor during a high-amplitude motion shake insertion of a hose/insert assembly.

amplitude. Small oscillations can also be seen on torque outputs, especially on the X and Y axes. The most noticeable difference when comparing to the reference plot of Figure 1.12 is that the force along Z (the direction of insertion) is halved. The feeling during the task is that the task is easier to perform than with the straight forward motion. The shake motion is a very intuitive solution to ease the manual insertion.

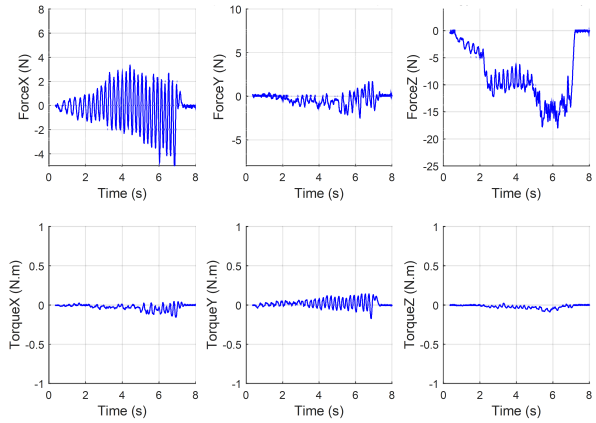

FIGURE 1.14 – Output of the ATI mini 45 - six-axis force sensor during a low-amplitude motion shake insertion of a hose/insert assembly.

Figure 1.14 shows the sensor output while performing the insertion with a low-amplitude shake motion. The scale is kept the same on the plots so as to facilitate the comparisons. As it can be observed, the amplitude of the oscillating forces are lowered by the low-amplitude motion. Moreover, the maximum force required in the Z direction is further lowered. However, the motion requires more total energy because the duration of the task is increased. The amplitude of the vibrations are lowered but the frequency is increased and so the increased

velocity requires some added effort.

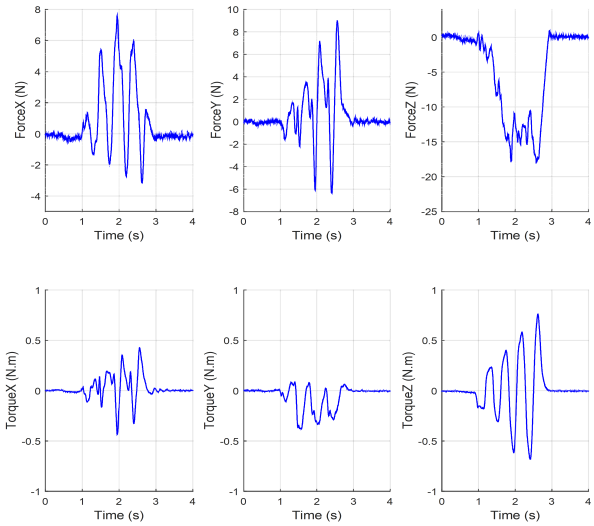

FIGURE 1.15 – Output of the ATI mini 45 - six-axis force sensor during a high-amplitude motion twist insertion of a hose/insert assembly.

Figure 1.15 shows the sensor output while performing the insertion with a high-amplitude twist motion. The twist motion is a back and forth rotational motion around the axis of the hose. The video referenced in Section 1.13 shows an example of this motion. On the output data, we can notice an expected significantly larger torque around the Z axis. The Z force is still significantly lowered, however, the X and Y forces as well as the X and Y torques are higher than with the preceding strategy.

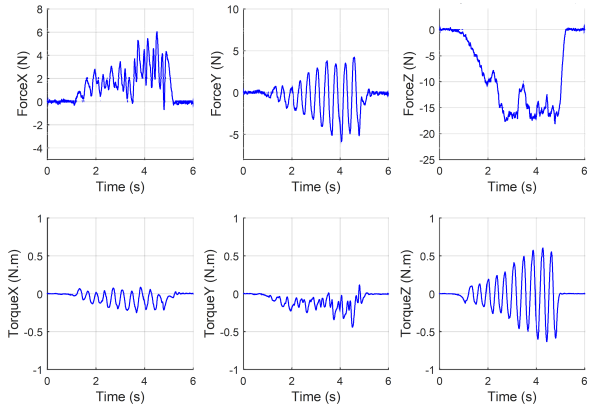

FIGURE 1.16 – Output of the ATI mini 45 - six-axis force sensor during a low-amplitude motion twist insertion of a hose/insert assembly.

Figure 1.16 shows the sensor output while performing the insertion with a low-amplitude twist motion. We notice a recurring pattern with the use of low-amplitude compared to high-

amplitude motions. The amplitude of the insertion force is lowered but the effort required by the user is not necessarily reduced. The lowered amplitude induces a larger number of oscillations which requires added energy.

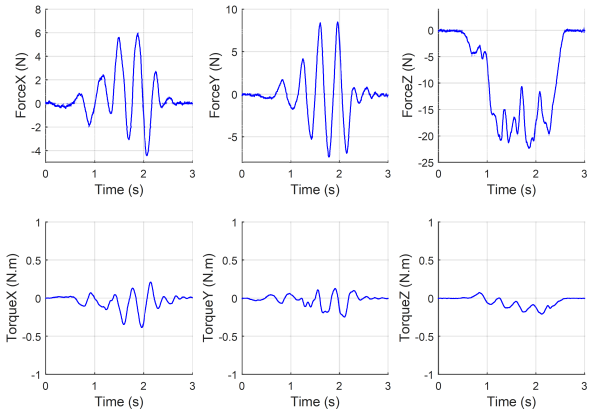

FIGURE 1.17 – Output of the ATI mini 45 - six-axis force sensor during a high-amplitude motion vortex insertion of a hose/insert assembly.

Figure 1.17 shows the sensor output while performing the insertion with a high-amplitude vortex motion. The vortex motion is a spiral motion around the axis of the insert on which the hose is intended to be mounted. The video referenced in Section 1.13 shows explicitly this also very natural movement. The results are similar to those obtained with the twist motion.

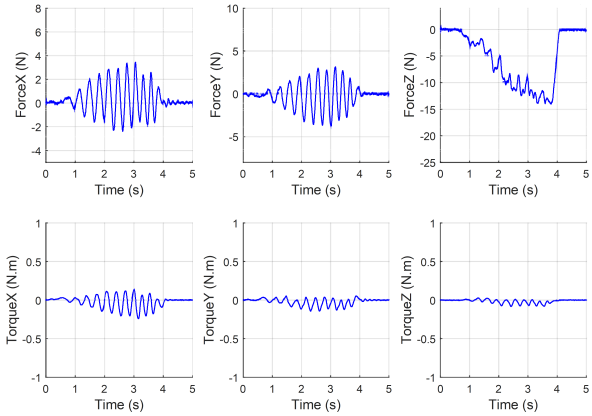

FIGURE 1.18 – Output of the ATI mini 45 - six-axis force sensor during a low-amplitude motion vortex insertion of a hose/insert assembly.

Figure 1.18 shows the sensor output while performing the insertion with a low-amplitude vortex motion. Based on user feedback and on the force/torque data, this method is the best among those tested. The force along the Z direction is the lowest recorded so far and other components of force/torque are also low. Nevertheless, although this strategy is the best for a manual assembly, it is not easy to replicate with a mechanical device.

1.12 Assembly strategies based on vibrations

The motion primitives described in the preceding section have been shown to ease the insertion. However, it may not be easy to translate this approach into a practical mechanism. Another possible approach consists in using vibrations. The expected behaviour is that vibrations would break the friction between the hose and the insert, which would greatly reduce the required force for the assembly. This approach is akin to that used in ultrasonic knifes Wiksell (1990). This assumption has been tested with three vibrating mechanisms mounted rigidly on the insert part. These mechanisms generate vibrations of various amplitude and frequency. These mechanisms also have various inertia, volume, cost and easiness of use.

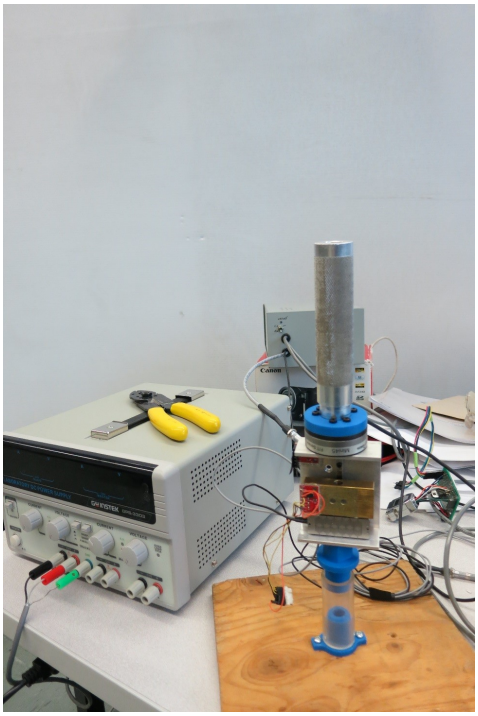

FIGURE 1.19 – Setup used to generate vibrations with a piezo actuator during a hose insertion.

The first mechanism is a piezo electric element. The complete setup is shown in Figure 1.19. The handle is at the top, the force sensor is beneath it, the piezo actuator is the bronze coloured box located beneath the force sensor and the insert is mounted just below. The whole assembly mounts on the hose shown here at the bottom, partly assembled on the picture. The method chosen here is to perform a straight forward insertion with the piezo actuator vibrating and then perform the same insertion again with the piezo actuator turned off and compare the behaviour and the force output measured. Obviously, a human operator still has to perform the insertion motion but the goal is to determine whether the vibrating component helps to lessen the required force or helps the process by any other means.

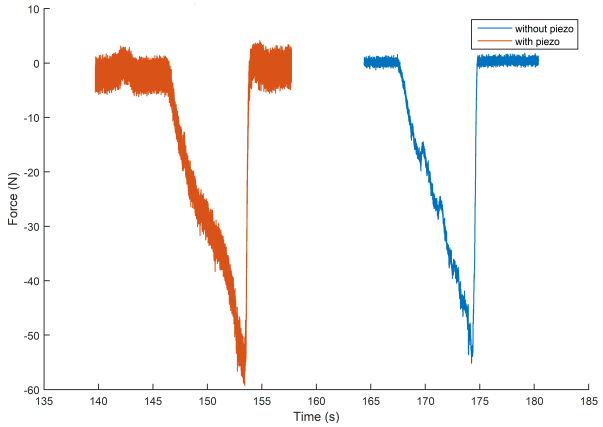

FIGURE 1.20 – Z force outputs of the ATI mini 45 - six-axis force sensor with the piezo actuator on (left) and with the piezo actuator off (right).

The sensor output is shown in Figure 1.20. The plot on the right is the measurement with the piezo off and the plot on the left is the measurement with the piezo on. The piezo actuator is rather small and easy to use but, as observed on the force output, even at maximum power the piezo actuator does not help much. The effect of the piezo can be noted with the oscillations around the visible original profile.

FIGURE 1.21 – Presentation of the setup used to generate vibrations with an unbalanced mass and a motor during a hose insertion.

The piezo would have been a convenient device to implement as a helping tool for insertion tasks but it has proven to lack power. In order to increase the power of the vibrations, a standard light commercial motor and an unbalanced mass are used so that vibrations are generated when the motor is on. The motor and mass assembly is fixed on the insert part of the hose/insert assembly. This is a low-cost and easy solution, which is not as compact as

the piezo actuator and which offers limited control over frequency and amplitude but which provides stronger vibrations. Two different modes were tested : one that produces vibrations in the plane orthogonal to the axis of the hose and one that produces vibrations along the axis. Figure 1.21 shows the setup in which the vibrations are generated along the axis of the hose.

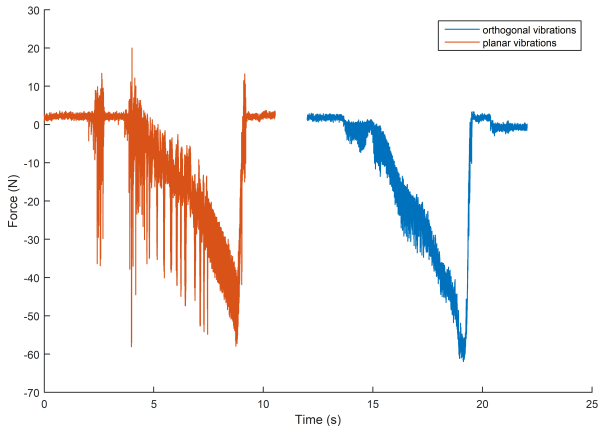

FIGURE 1.22 – Z force outputs of the ATI mini 45 - 6 axis force sensor with the motor and mass with the planar mode (left) and with orthogonal mode (right).

Figure 1.22 shows the sensor outputs for the planar vibrations on the left and the orthogonal vibrations on the right. First, it is noticed that planar vibrations produce significantly more noticeable vibrations on the data than the piezo actuator solution. However, neither the planar vibrations nor the orthogonal ones produced a significant ease during the insertion of the hose.

The first two devices (piezo actuator and unbalanced motor) were tried because they would

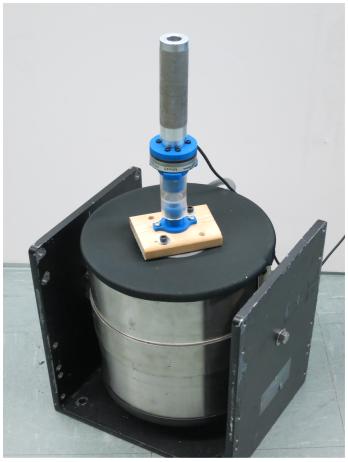

FIGURE 1.23 – Presentation of the setup used to generate vibrations with a shaker during a hose insertion.

be convenient solutions to implement. However, they showed a clear lack of power and are therefore not effective. Moreover, the lack of control over the frequency and force amplitude makes it difficult to find appropriate parameters. Therefore, a third device was tested, in order to further investigate the use of vibrations. Although this device does not constitute a practical solution for an insertion task, it is used to investigate the tuning of the vibration parameters with enough range to include working parameters. This device is a laboratory shaker, used for vibration test benches. Figure 1.23 shows the setup. The first part of the assembly is fixed on the shaker and the second is composed of the handle and the force sensor.

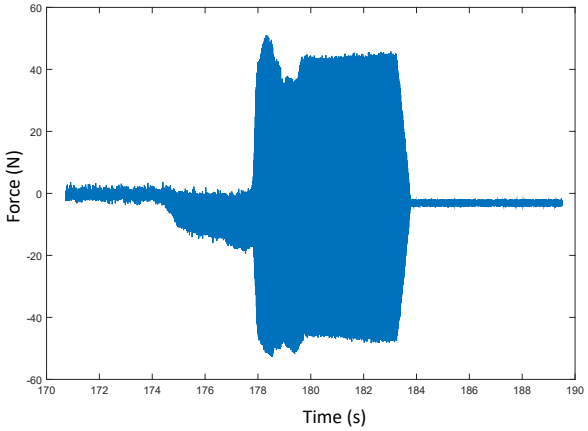

FIGURE 1.24 – Z force outputs of the ATI mini 45 - six-axis force sensor with a shaker.

Figure 1.24 shows the output of the sensor along the Z axis for a working insertion. The behaviour can be seen in the video referenced in Section 1.13. The controlled parameters are the vibration frequency and the input current, which is directly related to the force amplitude. The working parameters shown are a 80 Hz frequency and 1 A current. The obtained behaviour is that the insertion is so easy that almost no force is required to perform it. In fact, the gravity force on the handle is sufficient to produce the insertion. Not surprisingly, and as observed in Figure 1.24, the amplitude of the force generated by the shaker exceeds 40 N and is approximately equal to the maximum force measured to perform the insertion. In other words, the shaker produces a force that is sufficient to break the friction and perform the insertion. Therefore, the force required from the operator is very small. As mentioned above, although the use of a shaker such as the one used here may not be practical, it is nevertheless interesting to note that vibrations could be used for the purpose of facilitating insertions.

1.13 Video documentation.

A video accompanies this article, it can be found at [Video hosted on Youtube] (clickable link, if it does not work, enter the URL : $https://youtu.be/M8GztBgY_os$). The video illustrates the different measurements presented above. In the first part of the video, the impactor mechanism

is used to perform a snap-fit assembly task. The part used for the demonstration is a battery and servos module which is assembled on the door of a car. The module powers and controls electronic devices in the door such as the window or the rearview mirrors. The impactor manages to effectively perform the assembly in one swing, demonstrating the adequate design of the springs for this task. Then, a variant of the impactor is used for a hose assembly task. The impactor applies impacts on a part that fits in the selected plastic hose. The lever has been modified : more instances of the lever has been added on the rotating part so that the frequency of the impacts is increased, at the cost of a reduced stroke for the spring and therefore less energy per impact. The intent was to get closer to a vibrating behaviour, assumed more effective than the strong less frequent impacts. The result was not really conclusive and led to the following study with the shaker. The next segment of the video shows the acquisiition of the data presented above. The next clips present the motion strategy measurements and show clearly the motions described in the text. The last clips in the video show the tests performed with the shaker. The amplitude of the shaker being very low, the high pitch sound produced by it helps to notice when it is activated.

1.14 Conclusion

This article shows data measured on hose and snap-fit assembly tasks. These data are used to design a reliable and easy to use tool for the snap-fit assembly. The measurements on the hose assembly are used to study different motions during the insertion and provide interesting force data. Finally, the use of vibrations as a means of facilitating insertions has been investigated. It was shown that vibrations can indeed facilitate insertions, their use in practical applications remains challenging.

1.15 Bibliographie

Mansour Abtahi, Hodjat Pendar, Aria Alasty, and Gholamreza Vossoughi. Kinematics and singularity analysis of the hexaglide parallel robot. In *ASME 2008 International Mechanical Engineering Congress and Exposition*, pages 37–43. American Society of Mechanical Engineers, 2008.

Jong-Ho Baek, Sun-Uk Hwang, Jong-Hyun Lee, and Yong-Gu Lee. Snap-fit assembly of microscopic components by optical tweezers. In *Optical Trapping and Optical Micromanipulation III*, volume 6326, page 632610. International Society for Optics and Photonics, 2006.

Zhuming M Bi and Y Jin. Kinematic modeling of exechon parallel kinematic machine. *Robotics and Computer-Integrated Manufacturing*, 27(1) :186–193, 2011.

JA Carretero, RP Podhorodeski, MA Nahon, and Clement M Gosselin. Kinematic analysis and optimization of a new three degree-of-freedom spatial parallel manipulator. *ASME Journal of mechanical design*, 122(1) :17–24, 2000.

Christina Godin, Joshua Cashaback, Joel Cort, Jim Potvin, and Allison Stephens. An estimation of supporting hand forces for common automotive assembly tasks. Technical report, SAE Technical Paper, 2008.

D Christian Grieshaber and Thomas J Armstrong. Insertion loads and forearm muscle activity during flexible hose insertion tasks. *Human factors*, 49(5) :786–796, 2007.

D Christian Grieshaber, Thomas J Armstrong, Don B Chaffin, W Monroe Keyserling, and James Ashton-Miller. The effects of insertion method and force on hand clearance envelopes for rubber hose insertion tasks. *Human factors*, 51(2) :152–163, 2009.

Menglong Guo, David V Gealy, Jacky Liang, Jeffrey Mahler, Aimee Goncalves, Stephen McKinley, Juan Aparicio Ojea, and Ken Goldberg. Design of parallel-jaw gripper tip surfaces for robust grasping. In *Robotics and Automation (ICRA), 2017 IEEE International Conference on*, pages 2831–2838. IEEE, 2017.

S Jahanian, Chris David, D Goodwin, J Bearden, V Baharian, T Poplin, Dan Gerpheide, Clinton Roy, and Troy Simmons. Design of a sprinkler head and hose assembler for physically challenged workers. In *International Design Engineering Technical Conferences and Computers and Information in Engineering Conference*, volume 37017, pages 1027–1033, 2003.

Byoung Hun Kang and John T Wen. Design of compliant mems grippers for micro-assembly tasks. In *Intelligent Robots and Systems, 2006 IEEE/RSJ International Conference on*, pages 760–765. IEEE, 2006.

Anthony Luscher, Gaurav Suri, and Douglas Bodmann. Enumeration of snap-fit assembly motions. In *Technical papers of the annual technical conference-society of plastics engineers incorporated*, volume 3, pages 2677–2683. SOCIETY OF PLASTICS ENGINEERS INC, 1998.

Bruno Monsarrat and Clément M Gosselin. Singularity analysis of a three-leg six-degree-of-freedom parallel platform mechanism based on Grassmann line geometry. *The International Journal of Robotics Research*, 20(4) :312–328, 2001.

László Rónai and Tamás Szabó. Snap-fit assembly process with industrial robot including force feedback. *Robotica*, 38(2) :317–336, 2020.

Xuguang Wang, Nancy Black, Sonia Duprey, and Christophe Roybin. An experimental investigation on push force and its perception during a flexible hose insertion task encountered in a truck assembly line. *Ergonomics*, 57(9) :1416–1426, 2014.

Hans Wiksell. Ultrasonic knife, December 4 1990. US Patent 4,974,581.

Tsung-Liang Wu, Chin-Chia Mai, Jih-Hsiang Yeh, Yu-tsung Chiu, and Ping-Hsin Shen. Preliminary study on utilization of impact force for snap-fit assembly. In *Information Storage and Processing Systems*, volume 49880, page V001T07A004. American Society of Mechanical Engineers, 2016.

Matteo Zoppi, Dimiter Zlatanov, and Rezia Molfino. Kinematic analysis of the exechon tripod. *ASME Paper No. DETC2010-28668*, 2010.

Chapitre 2

Modelling and development of passively adaptive assistive tools for the assembly of press-fit components

2.1 Résumé

Cet article présente les travaux effectués lors de la première partie du projet portant sur les mécanisme passifs de correction de position. La précision a été jugée comme un facteur critique lors de l'assemblage rapide de pièces à distance. Cet article présente des architectures passives ayant pour but d'aider à réaliser des tâches d'assemblage de façon précise. Une solution spécifique pour la génération passive de forces avec des seuils est présentée. Ensuite, la cinématique de plusieurs mécanismes de rotation et de translation est analysée en utilisant la théorie des torseurs. Puis, un cas spécifique est choisi et la conception d'un prototype de mécanisme de correction de précision est présentée ainsi que les résultats de tests d'insertion d'un connecteur de bougie de moteur.

2.2 Abstract

This article discusses passive mechanical architectures for accuracy correction during assembly operations. A specific solution for passive force generation with thresholds is presented. Then, the kinematics of several rotational and translational mechanisms is presented using torsor theory. Afterwards, a case study is introduced and the design of a prototype is presented together with some tests performed on a spark plug assembly task.

Introduction

Assembly tasks consist in making the connection between two or more separate parts to build another part or mechanism composed of the previous parts. Complex objects are generally composed of several simpler ones, which need to be assembled. Assembly can provide the advantage of transporting parts that are lighter and smaller than the final assembled product as well as easing logistics. However, the assembly operation itself involves additional operations which may require dexterity. Reference Angerer et al. (2012) raises the potential advantages of mobile robots to assist in assembly operations in the automotive industry and Michalos et al. (2010) presents an exhaustive summary of the assembly research field for automotive assembly. This topic is still an active research area. For instance, Blazevski and Haslwanter (2017); Haslwanter and Blazevski (2018); Chen and Chan (2019) deal with methods to improve the operations in assembly lines. Several articles present devices designed to help operators to perform tasks on the assembly lines (see for instance Jahanian et al. (2003); Grosu et al. (2017); Campeau-Lecours et al. (2017); Farahmand et al. (2005); Lee et al. (2011)) or to improve efficiency (see for instance Modaresahmadi et al. (2018); Movassagh-Khaniki et al. (2016); Mohammed et al. (2017); Shrivastava and Joshi (2016); Gao et al. (2019)).

The repetitive nature of assembly tasks, combined with the long work shifts make such tasks rather tedious, which is a challenge for industry. Indeed, studies highlight (Wagner et al. (2018); de Negreiros et al. (2019); Weber (2013); Baraldi and Paulo C (2011) for example) the impact of such tasks on the operators' health over time. Assembly tasks often have to be performed in cluttered environments, which leads to operators adopting uncomfortable poses that constitute ergonomic stressors. A possible solution to improve these conditions is to allow operators to work remotely from where the assembly is physically performed, in an environment that is free of obstacles and constraints, where natural favorable postures can be adopted. Such an approach can be implemented by designing mechanisms that make the link between the task area and the operator's area. This concept is illustrated schematically in Fig. 2.1.

One of the issues that arise with the above mentioned approach is that of accuracy. Indeed, performing moderately agile tasks from a distance is expected to be more difficult, especially if the execution time is short. Accuracy problems during assembly tasks is a popular research topic (see for instance Fukushima et al. (2010); Zhehan et al. (2013); Liu (2013); Tian and Whitehouse (2003)). When working remotely, human visual and haptic feedback is less effective and hence sensors should be used to compensate for this reduced accuracy. The combination of the mechanism and the sensors aims at maintaining the level of productivity, or even improve it. To this end, two main methods exist in the literature : the first focuses on the strategy chosen for the assembly while the second consists in the development of assistive mechanisms.

An example of the first method is shown in Stemmer et al. (2007) where the assembly of thin

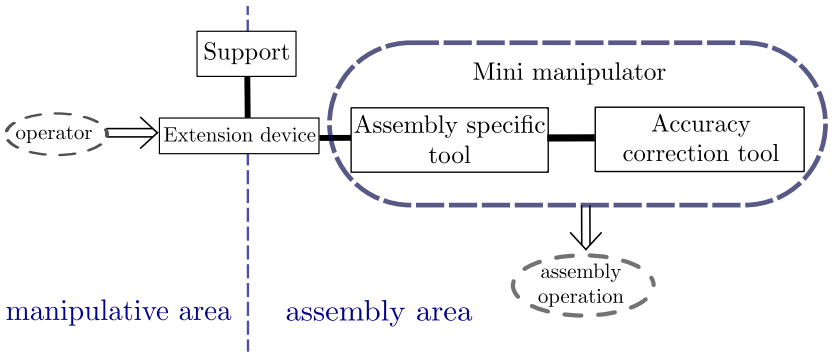

FIGURE 2.1 – Schematic concept of the interaction between the operator and the mechanism to perform the assembly task remotely.

parts is made faster using a control scheme for a robot that includes the stiffness of the involved parts and simulations for prior adjustments of the trajectories. Reference Kim et al. (2002) presents a similar method for the insertion of cylindrical parts in holes with robotic hands composed of several actuated fingers. Reference Kang et al. (1997) explores more complex methods for more complex assembly tasks.

The second method introduces a mechanism that is specifically designed to address the accuracy problem. The most common such mechanism used with robots is the "Remote Centre of Compliance" mechanism or RCC. This mechanism introduces a centre of rotation whose location is chosen. The mechanism is driven by the external reaction forces produced by a position error and the induced motion tends to push the end-effector in the adequate configuration for the assembly. The concept of RCC was first introduced in Whitney (1982). The mechanism presented in this reference is composed of rigid bars with spring elements called shear pads for the neutral configuration and the return behaviour. More generalized mechanisms of this type appeared more recently. For example, reference Ciblak and Lipkin (2003) describes a RCC design methodology and proposes the use of low stiffness parts instead of joints and springs, which is proven useful for small motions. Other articles describe passive correction mechanisms such as Kim et al. (2000),Liu et al. (2019), Zhao and Wu (1998), Chng et al. (2016) or Ang and Andeen (1995). Reference Zong et al. (2008) generalizes this family of mechanisms as "Remote Centre of Motion" or RCM, and describes the main architectures that fit in this classification.

In this paper, the development of passive adaptive elastic mechanisms for press fit assembly is addressed. The concept of RCC mechanism is first revisited. Elastic mechanisms are described that can be used to correct for translational or rotational errors. The mechanisms are then analyzed using torsor theory. Alternative architectures of mechanisms are proposed and analyzed. A new architecture of RCC mechanism with a fixed centre of rotation is presented. A case study related to the assembly of spark plug connectors is then used as an illustrative

example. A mechanism is designed and analyzed for this application and a prototype is built. Finally a video demonstration of the prototype is provided.

2.3 Elastic mechanisms for the design of adaptable mechanisms

The kinematic motion of a corrective mechanism must be related to the assembly task for which it is intended. Both translations and rotations are necessary in most cases, but the elastic mechanisms presented here are separated between translation and rotation mechanisms because they have different features to highlight.

2.3.1 Translational mechanisms

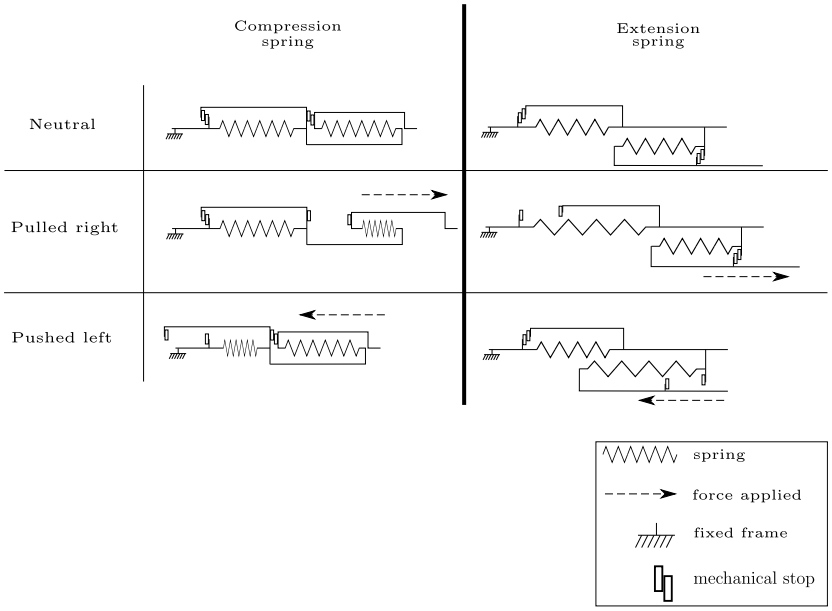

FIGURE 2.2 – Two different designs of translational elastic mechanisms with compression springs (left) and extension springs (right) using two springs.

In order to provide robustness in an assembly operation, elastic mechanisms with force thresholds can be used. Such mechanisms greatly reduce the positioning accuracy required to perform a given task and can be referred to as adaptable mechanisms. The adaptable mechanisms should allow movements when needed to adjust for any inaccurate placement of the end tool. The mechanisms should require as few features as possible in order to be robust, reliable and easy to use. Passive mechanisms should therefore be favoured.

Elastic components can be used to construct passive adaptive mechanisms. Figure 2.2 shows two examples of designs for passive translational return mechanisms with force thresholds. The

springs provide the desired elastic behaviour. They also provide the mobility for the mechanism to correct the position of the end tool and generate a force to return to the neutral position when the mobility is not required (when no external force is applied). Moreover, as shown in Fig. 2.2, the use of mechanical stops combined with the springs yields a force threshold, such that small forces such as low acceleration inertial forces do not affect the configuration of the mechanism, thereby ensuring a stable and reliable behaviour. This is accomplished by preloading the spring in a working state in the neutral position of the mechanism. In Fig. 2.2, two springs are used. Each spring is preloaded, thereby providing a force preload in each direction of the axis of the translation. The force threshold is determined by the preload of the spring in the neutral state. Then, the slope describing the increase of the force relative to the deformation of the spring along the translation axis corresponds to the stiffness of the spring.

The threshold force value can be estimated as :

$$f = E\Delta x_0 \tag{2.1}$$

where E is the stiffness of the spring and Δx_0 the deformation of the spring in the neutral state of the mechanism. The preload can be either compression or extension depending on the type of spring used. The initial deformation is controlled by the stops, as shown in Fig. 2.2.

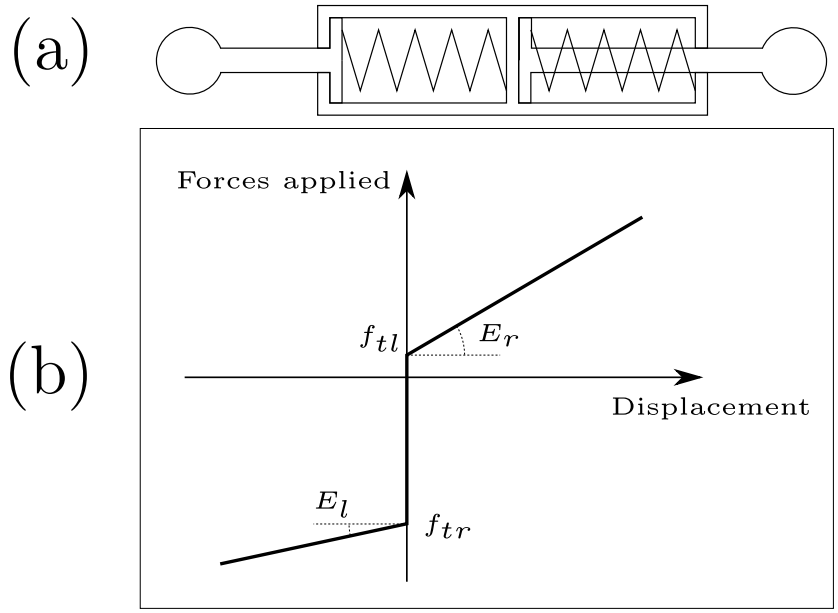

FIGURE 2.3 – (a) Schematic representation of the mechanism. (b) Illustration of the force threshold induced by the elastic mechanism.

Figure 2.3 illustrates the force/displacement behaviour of the mechanism. In each direction of the axis of translation, one of the springs is involved. In the right direction, the force

threshold f_{tr} must be overcome and the slope E_r represents the stiffness of the mechanism in this direction.

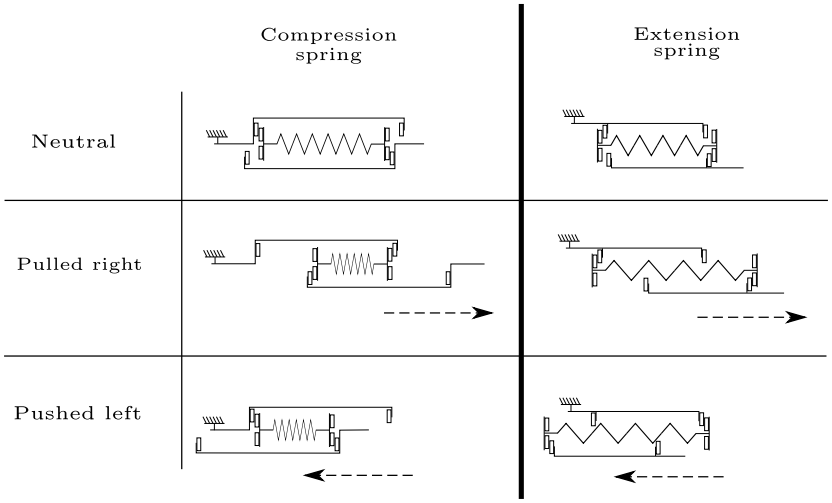

FIGURE 2.4 – Two different designs of translational elastic mechanisms with a compression spring (left) and an extension spring (right) using a single spring.

Figure 2.4 shows two examples of elastic mechanisms that work similarly to the ones shown in Fig. 2.2 but requiring only one spring. The mechanism still works in both directions but the same spring is active for both directions of the translation axis. Therefore, using the notation of Fig. 2.3, one has in this case $f_{tr} = f_{tl}$ and $E_r = E_l$. Such a mechanism is noticeably more compact and requires fewer springs but, as shown in Fig. 2.4 it includes an extra moving carriage and the left and right threshold and stiffness cannot be adjusted independently.

2.3.2 Rotational mechanisms

The above mechanisms work for translational motions. However, in the case of rotational motions, the design must be modified. First, torsional springs are used instead of linear springs. Then, the parts must be designed to rotate around a common axis. The mechanisms are presented here with compression springs but they can easily be adapted for extension springs similarly to what was done above for translational mechanisms.

The mechanism shown in Fig. 2.5 is the rotational equivalent of the one shown in Fig. 2.2. The mechanism is composed of two stages, referred to arbitrarily as an upper stage and a lower stage. This is required to stack the different parts on the same axis one onto another. Each stage has a different spring. An intermediate part is also required to make the connection between the two stages. This part is used as a mobile extension for the mechanical stops. It is shown through the clockwise and counterclockwise sections of Fig. 2.5. Part 1 is the reference part and is fixed. Part 2 is presented in the neutral configuration (unmoved), in a moved counterclockwise configuration and in a moved clockwise configuration. In the counterclockwise

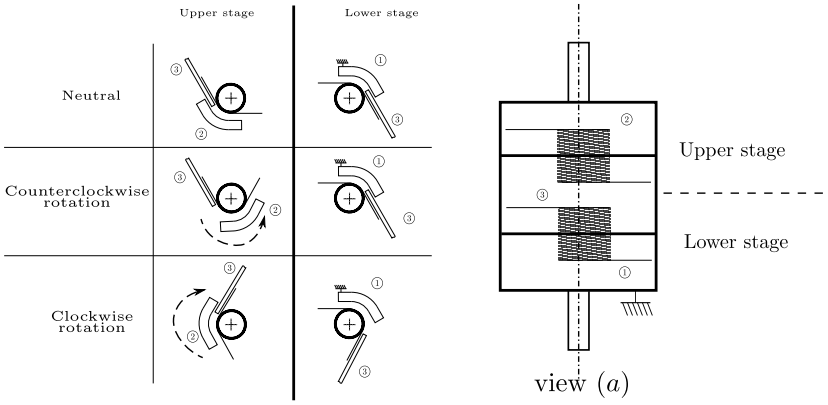

FIGURE 2.5 – Rotational elastic mechanism with preload. The upper and lower stages are connected by the rotating shaft. Two springs are used. (1) is the reference part, (2) is the connecting part and (3) is the intermediate part. View (a) shows a side view of the mechanism, it shows clearly the stages and how the three parts are connected.

configuration, part 3 extends the stop of part 1 while in the clockwise configuration it extends the stop of part 2.

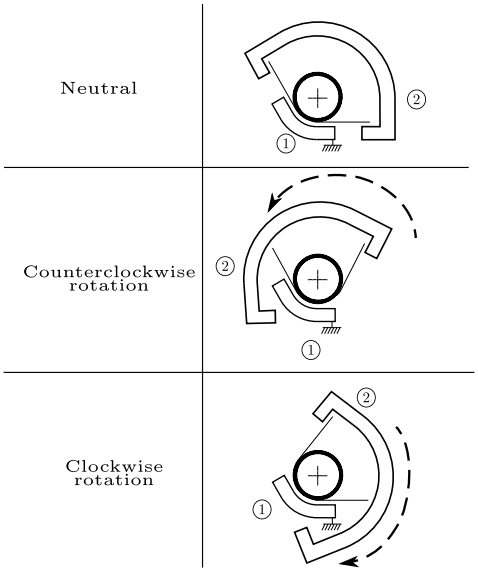

FIGURE 2.6 – One specific design of a torsional elastic mechanism with preload. A single spring is used. (1) is the reference part and (2) is the connecting part.

Alike for the translational mechanisms, a single spring equivalent can be designed. The mechanism shown in Fig. 2.6 is the rotational equivalent of the one shown in Fig. 2.4. It is conceptually simpler than the translational mechanism but the parts require unusual shapes. No stages are necessary in this design, which is a significant advantage over the two-spring mechanism.

2.4 Kinematic architectures

The preloaded elastic mechanisms described above and other similar modules can be used to construct multi-dof adaptive mechanisms. Therefore, many architectures are possible and several can be considered in the context of press-fit assembly tasks. A few promising designs are presented in this section.

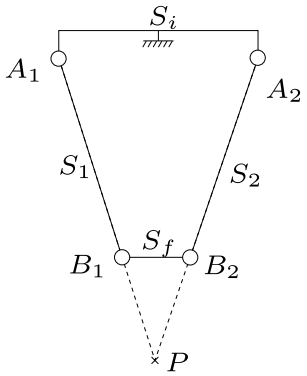

FIGURE 2.7 – Planar model of the rotational part of the classical Whitney Remote Centre of Compliance (RCC) mechanism.

2.4.1 Analysis of the original RCC mechanism

First, the mechanism used as the first designed RCC mechanism Whitney (1982) is considered. Figure 2.7 shows the notation used to describe the behaviour of a planar equivalent of the Whitney RCC mechanism. Four different bodies connected with revolute joints are involved and are referred to as S_i, S_f, S_1 and S_2. S_i is the reference frame (fixed) body of the model. S_f is the end working body, the one which must satisfy the desired behaviour for the mechanism to be effective. S_1 and S_2 are intermediate bodies. Four revolute joints are included in the mechanism, in A_1, A_2, B_1 and B_2. The centre of compliance is located at point P, which is the intersection of the lines defined by the pairs of revolute joints connected respectively to bodies S_1 and S_2. In the spatial mechanism, the centre of compliance is at the intersection of three lines, one extra leg being involved. This raises one first issue, that is that the intersection of lines in a plane is guaranteed, but this is not the case in the spatial case, where lines can be skewed. Therefore, additional design considerations must be dealt with in the spatial case.

First of all, we will demonstrate that the centre of compliance is actually at the assumed location shown in Fig. 2.7. Kinematic torsors are used for this demonstration. The velocity decomposition is written as

$$\{\mathcal{V}(P{\in}S_f/S_i)\} = \{\mathcal{V}(P{\in}S_f/S_1)\} + \{\mathcal{V}(P{\in}S_1/S_i)\} \tag{2.2}$$

$$= \{\mathcal{V}(P{\in}S_f/S_2)\} + \{\mathcal{V}(P{\in}S_2/S_i)\} \tag{2.3}$$

which should be read as follows : the velocity of point P attached to body frame S_f relative to the body frame S_i can be decomposed as the sum of the velocity of P attached to S_f relative to S_1 and the velocity of P attached to S_1 relative to S_i or the sum of the velocity of P attached to S_f relative to S_2 and the velocity of P attached to S_2 relative to S_i.

The brackets around $\mathcal{V}$ indicate that a kinematic torsor is used, namely a six-dimensional vector combining angular and translational velocities. The developed form of the torsor is as follows :

$$\{\mathcal{V}(P{\in}S_f/S_1)\} = {}_P\left\{ \begin{array}{c} \boldsymbol{\omega}_{S_f/S_1} \\ \boldsymbol{v}_{P\in S_f/S_1} \end{array} \right\}_{S_f/S_1} \tag{2.4}$$

with $\boldsymbol{\omega}$ the angular velocity and $\boldsymbol{v}$ the velocity of point P. The notation refers to the notation used in Fig. 2.7.

The kinematic torsor theory requires the definition of one torsor for each joint involved in the kinematic chain. The mechanism is composed of two parallel chains. The first chain is composed of joints A_1 and B_1, the torsors at these points are :

$$\{\mathcal{V}(B_1{\in}S_f/S_1)\} = {}_{B_1}\left\{ \begin{array}{c} \boldsymbol{\omega}_{S_f/S_1} \\ \boldsymbol{v}(B_1 \in S_f/S_1) \end{array} \right\}_{S_f/S_1} \tag{2.5}$$

$$\{\mathcal{V}(A_1{\in}S_1/S_i)\} = {}_{A_1}\left\{ \begin{array}{c} \boldsymbol{\omega}_{S_1/S_i} \\ \boldsymbol{v}(B_1 \in S_1/S_i) \end{array} \right\}_{S_f/S_1} \tag{2.6}$$

where :

$$\boldsymbol{\omega}_{S_f/S_1} = \begin{bmatrix} 0 & 0 & \omega_{S_f/S_1} \end{bmatrix}^T \tag{2.7}$$

$$\boldsymbol{\omega}_{S_1/S_i} = \begin{bmatrix} 0 & 0 & \omega_{S_1/S_i} \end{bmatrix}^T \tag{2.8}$$

$$\boldsymbol{v}_{B_1\in S_f/S_1} = \mathbf{0} \tag{2.9}$$

$$\boldsymbol{v}_{A_1\in S_1/S_i} = \mathbf{0}. \tag{2.10}$$

Then, we must express the torsors at the same point to apply the torsor principles. The angular velocity remains unchanged by this operation but the translational velocity must be recomputed as follows :

$$\boldsymbol{v}_{P\in S_1/S_i} = \boldsymbol{v}_{A_1\in S_1/S_i} + (\mathbf{a}_1 - \mathbf{p}) \times \boldsymbol{\omega}_{S_1/S_i} \tag{2.11}$$

$$\boldsymbol{v}_{P\in S_f/S_1} = \boldsymbol{v}_{B_1\in S_f/S_i} + (\mathbf{b}_1 - \mathbf{p}) \times \boldsymbol{\omega}_{S_f/S_i}. \tag{2.12}$$

where $\mathbf{a}_1$, $\mathbf{b}_1$ and $\mathbf{p}$ are respectively the position vectors of points A_1, B_1 and P. The second kinematic chain is similar and leads to similar results :

$$\boldsymbol{v}_{P\in S_2/S_i} = \boldsymbol{v}_{A_2\in S_2/S_i} + (\mathbf{a}_2 - \mathbf{p}) \times \boldsymbol{\omega}_{S_2/S_i} \tag{2.13}$$

$$\boldsymbol{v}_{P\in S_f/S_2} = \boldsymbol{v}_{B_2\in S_f/S_2} + (\mathbf{b}_2 - \mathbf{p}) \times \boldsymbol{\omega}_{S_f/S_2}. \tag{2.14}$$

The torsor principles state for a serial chain that the full mobility is the sum of the kinematic torsors and for parallel chains that the kinematic torsors are equal. Therefore, the mobility of the end body S_f expressed at point P is :

$$\{\mathcal{V}(P\in S_f/S_i)\} = {}_P\left\{ \begin{array}{c} \boldsymbol{\omega}_{S_f/S_i} \\ \boldsymbol{v}(P \in S_f/S_i) \end{array} \right\}_{S_f/S_i} \tag{2.15}$$

where,

$$\boldsymbol{\omega}_{S_f/S_i} = \boldsymbol{\omega}_{S_f/S_1} + \boldsymbol{\omega}_{S_1/S_i} \tag{2.16}$$

$$= \boldsymbol{\omega}_{S_f/S_2} + \boldsymbol{\omega}_{S_2/S_i} \tag{2.17}$$

$$\tag{2.18}$$

and,

$$\boldsymbol{v}_{P\in S_f/S_i} = \boldsymbol{v}_{P\in S_f/S_1} + \boldsymbol{v}_{P\in S_1/S_i} \tag{2.19}$$

$$= (\mathbf{b}_1 - \mathbf{p}) \times \boldsymbol{\omega}_{S_f/S_1} + (\mathbf{a}_1 - \mathbf{p}) \times \boldsymbol{\omega}_{S_1/S_i} \tag{2.20}$$

$$= \boldsymbol{v}_{P\in S_f/S_2} + \boldsymbol{v}_{P\in S_2/S_i} \tag{2.21}$$

$$= (\mathbf{b}_2 - \mathbf{p}) \times \boldsymbol{\omega}_{S_f/S_2} + (\mathbf{a}_2 - \mathbf{p}) \times \boldsymbol{\omega}_{S_2/S_i}. \tag{2.22}$$

The expressions of Eqn.2.20 and Eqn.2.22 can be projected along the direction of the links as follows.

$$\begin{aligned}(\mathbf{b}_1 - \mathbf{a}_1)^T \boldsymbol{v}_{P\in S_f/S_i} =& (\mathbf{b}_1 - \mathbf{a}_1)^T [(\mathbf{b}_1 - \mathbf{p}) \times \boldsymbol{\omega}_{S_f/S_1} \\ &+ (\mathbf{a}_1 - \mathbf{p}) \times \boldsymbol{\omega}_{S_1/S_i}].\end{aligned} \tag{2.23}$$

Because P, A_1 and B_1 are aligned, $(\mathbf{b}_1 - \mathbf{a}_1)$, $(\mathbf{b}_1 - \mathbf{p})$ and $(\mathbf{a}_1 - \mathbf{p})$ are collinear. Therefore, based on the properties of the cross product , one has

$$(\mathbf{b}_1 - \mathbf{a}_1)^T[(\mathbf{b}_1 - \mathbf{p}) \times \boldsymbol{\omega}_{S_f/S_1} + (\mathbf{a}_1 - \mathbf{p}) \times \boldsymbol{\omega}_{S_1/S_i}] = 0. \tag{2.24}$$

Similarly, because P, A_2 and B_2 are aligned, one has

$$(\mathbf{b}_2 - \mathbf{a}_2)^T[(\mathbf{b}_2 - \mathbf{p}) \times \boldsymbol{\omega}_{S_f/S_2} + (\mathbf{a}_2 - \mathbf{p}) \times \boldsymbol{\omega}_{S_2/S_i}] = 0. \tag{2.25}$$

In summary,

$$(\mathbf{b}_1 - \mathbf{a}_1)^T \boldsymbol{v}_{P \in S_f/S_i} = 0 \tag{2.26}$$

$$(\mathbf{b}_2 - \mathbf{a}_2)^T \boldsymbol{v}_{P \in S_f/S_i} = 0 \tag{2.27}$$

Except for some avoided specific design choices and configurations, $(\mathbf{b}_1 - \mathbf{a}_1)$ and $(\mathbf{b}_2 - \mathbf{a}_2)$ span the whole planar space. Then, the projection of $\boldsymbol{v}_{P \in S_f/S_i}$ on these axes being equal to zero necessarily yields :

$$\boldsymbol{v}_{P \in S_f/S_i} = \mathbf{0}. \tag{2.28}$$

This shows that P is, as expected, the centre of rotation of the end body.

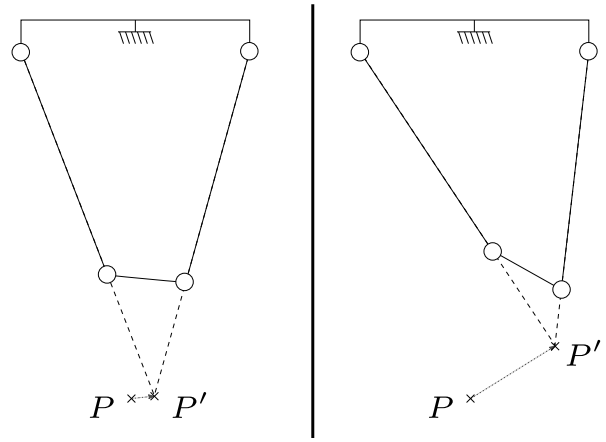

FIGURE 2.8 – Presentation of the displacement of the centre of rotation in a close to neutral configuration (left) and further to neutral configuration (right).

Figure 2.8 shows the displacement of the centre of rotation for two configurations of the mechanism. The centre of rotation in the neutral configuration is noted P and the centre of

rotation in a different configuration is noted P'. Both P and P' are presented in the figure to show the displacement of the centre of rotation. In the configuration shown on the left-hand side, the mechanism is close to its neutral configuration, working only to correct a small orientation error. The displacement of the centre of rotation is then rather small and the effectiveness of the mechanism is satisfactory. However, in the configuration shown on the right-hand side, the mechanism is far from the neutral configuration. As it can be observed, the centre of rotation is then much further from its locus in the neutral configuration. As a result, the mechanism does not necessarily work as intended. The displacement of the centre of rotation makes the behaviour of the mechanism very uncertain and so the mechanism works properly in a very small range of operation and is not necessarily robust to larger positioning or orientation errors. The extension of the classical RCC to a three-dimensional mechanism is

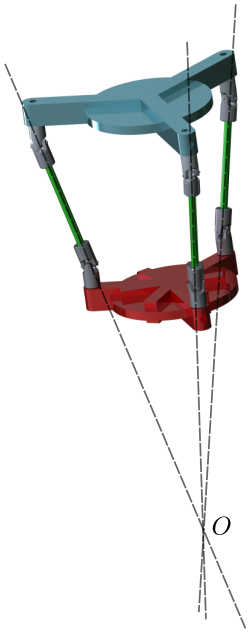

FIGURE 2.9 – Spatial model of the classical RCC mechanism, whose architecture is 3-HH, where H stands for a Hooke joint.

illustrated in Fig. 2.9.

2.4.2 Analysis of a novel RCC mechanism

In practical applications involving insertion tasks, it is desired to design mechanisms that can operate in mesoscopic workspaces. In other words, appropriate mechanisms should be capable to compensate for orientation errors in the tens of degrees and positioning errors of the order of the overall mechanism's size. For instance, a device whose size is in the order of centimetres should be able to compensate for positioning errors in the order of centimetres. The deviation of the centre of rotation discussed above is an angular limitation for the classical

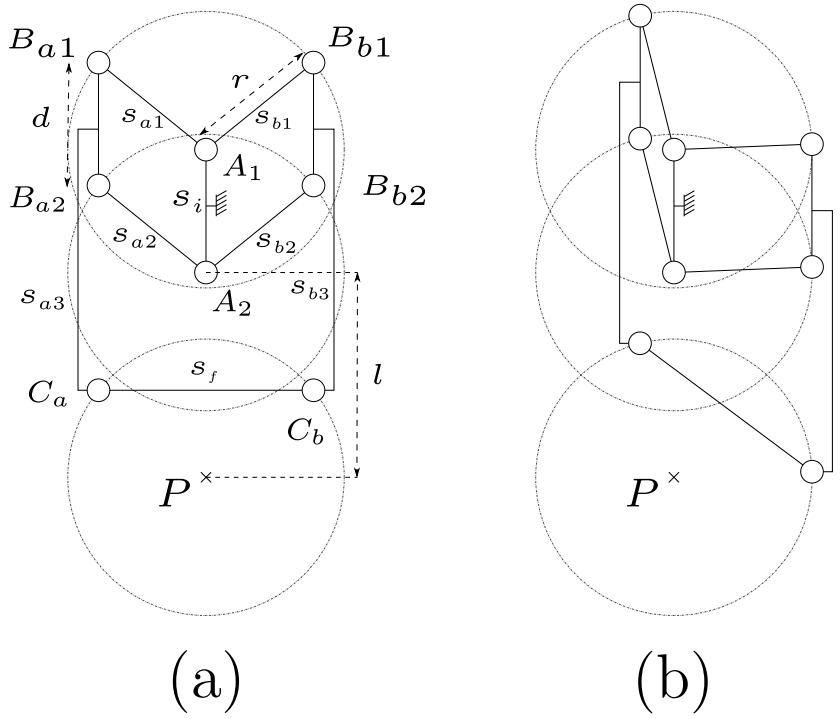

FIGURE 2.10 – Schematic representation of the behaviour of the novel planar Remote Centre of Rotation (RCR). (a) reference configuration (b) displaced configuration. It can be observed that the centre of rotation of the terminal link is fixed, i.e., independent from the configuration of the mechanism.

mechanism that renders it generally insufficient for assembly applications. Hence, alternative architectures are explored in this work in order to find better suited mechanisms. In order to demonstrate how these architectures can be investigated, the analysis of one of the most promising architectures is now presented here. In section 2.5, a case study will be presented where yet another type of architecture will be used.

A schematic representation of the mechanism studied in this section is shown in Fig. 2.10. It consists of two parallelogram mechanisms mounted on common revolute joints located on the base link. The coupler links of the parallelogram mechanisms are connected via a four-bar linkage that constitutes a parallelogram in the reference configuration of the mechanism. The mechanism is studied using its planar variant but the corresponding spatial architecture is shown afterwards. The demonstration, albeit more complex due to the introduction of the third dimension, is fairly similar. Similarly to what was done above for the original RCC mechanism, it is desired to demonstrate that the remote point P is a centre of rotation for the end part S_f. P is defined as the intersection of the line parallel to A_1B_{a1} passing through C_a, and the line parallel to A_1B_{b1} passing through C_b. Link S_i is the fixed link. Two different kinematic chains connect link S_i to the terminal link S_f. Each kinematic chain is composed of a parallelogram and an extension bar. In the architecture studied in the preceding sub-section,

the remote centre of rotation was obtained as the intersection of lines that crossed with an acute angle, with more acute angles rendering the position of the centre less stable. In the case of the mechanism of Fig. 2.10, the centre of rotation is displaced using a combination of a parallelogram architecture and an extension bar. The parallelogram in the first kinematic chain is formed by the revolute joints A_1, A_2, B_{a1} and B_{a2}. The extension bar is the link S_{a3} that connects to the end part through the revolute joint located at C_a. The second kinematic chain is similar, as shown in Fig. 2.10. Each kinematic chain constrains a point attached to the end part to rotate around the remote point P. The terminal link is fully constrained in translation. Therefore, constraining two different points to rotate around the same point is sufficient to constrain the terminal link to a pure rotation motion around this point. The distance at which the centre of rotation is displaced is dependent on the length of the bars of the parallelogram, r (see Fig. 2.10) and the length l of the extension bar. It is more difficult to displace the centre of rotation far from the base with this design than with the classical one. However, the main advantage is that the location of the centre of rotation is guaranteed to be fixed, i.e, independent from the configuration of the mechanism, and therefore the mechanism is functional for a much wider range of motions. In Fig. 2.10, circles show the possible motion of some points of interest. It can be observed that the revolute joints on the terminal link are constrained to move on the same circle, which in this planar case constrains the terminal link to undergo pure rotations around the centre of the circle. The impact of the parameters of the architecture on the behaviour of the mechanism is illustrated in Fig. 2.11. Model 1 shows the effect of reducing the length of the terminal link S_f. The location of the centre of rotation is not moved with respect to the fixed base, but it is further from the terminal link. As a consequence, the parallelograms are then in a configuration closer to their "flat" state which is a singular configuration that should be avoided, and hence the working range of the mechanism is limited. Model 2 illustrates the effect of increasing the length of the bars that compose the parallelogram. The circles describing the motion are consequently larger and so the centre of rotation is effectively moved away from the mechanism. However, the global size of the mechanism is significantly increased. Nevertheless, modifying this parameter is a good option to adjust the location of the centre of rotation. Model 3 illustrates the effect of increasing the length of the extension bar. Increasing the length of this bar is the simplest way to increase the distance between the centre of rotation and the fixed base while limiting the size of the mechanism. However, varying this length does not change the position of the centre of rotation with respect to the terminal link.

Referring to the notation introduced in Fig. 2.10 and using torsors and the velocity decomposition as in the above derivations, one can write

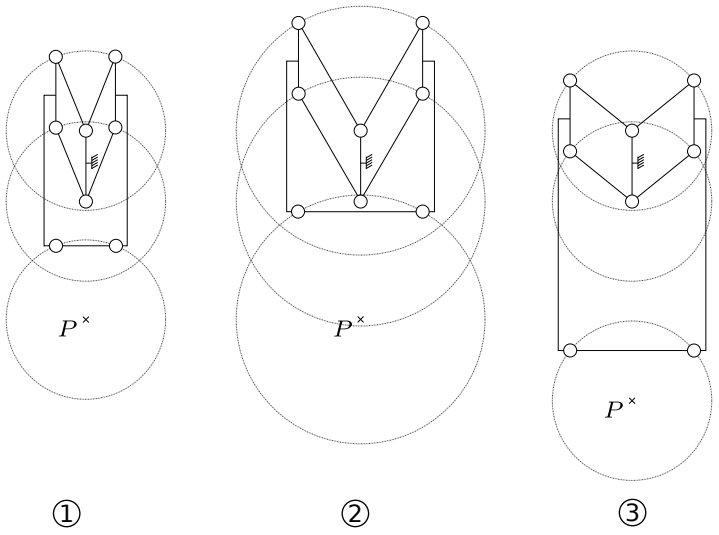

FIGURE 2.11 – Presentation of the models used to describe the behaviour of the planar Remote Centre of Rotation (RCR).

$$\begin{aligned}\{\mathcal{V}(P{\in}S_f/S_i)\} &= \{\mathcal{V}(P{\in}S_f/S_{a3})\} + \{\mathcal{V}(P{\in}S_{a3}/S_{a1})\} \\ &\quad + \{\mathcal{V}(P{\in}S_{a1}/S_i)\} \qquad (2.29) \\ &= \{\mathcal{V}(P{\in}S_f/S_{a3})\} + \{\mathcal{V}(P{\in}S_{a3}/S_{a2})\} \\ &\quad + \{\mathcal{V}(P{\in}S_{a2}/S_i)\} \qquad (2.30)\end{aligned}$$

which represents the velocity decomposition for each kinematic chain.

The angular velocity decomposition can be written as

$$\begin{aligned}\boldsymbol{\omega}_{S_f/S_i} &= \boldsymbol{\omega}_{S_f/S_{a3}} + \boldsymbol{\omega}_{S_{a3}/S_{a1}} + \boldsymbol{\omega}_{S_{a1}/S_i} \qquad (2.31) \\ &= \boldsymbol{\omega}_{S_f/S_{a3}} + \boldsymbol{\omega}_{S_{a3}/S_{a2}} + \boldsymbol{\omega}_{S_{a2}/S_i} \qquad (2.32) \\ &= \boldsymbol{\omega}_{S_f/S_{b3}} + \boldsymbol{\omega}_{S_{b3}/S_{b1}} + \boldsymbol{\omega}_{S_{b1}/S_i} \qquad (2.33) \\ &= \boldsymbol{\omega}_{S_f/S_{b3}} + \boldsymbol{\omega}_{S_{b3}/S_{b2}} + \boldsymbol{\omega}_{S_{b2}/S_i} \qquad (2.34)\end{aligned}$$

The objective is to show that the velocity of point P of link S_f is zero. Similarly to the analysis presented above, the method consists in projecting the velocity vectors on two vectors that form a base for the motion in the plane if they are not collinear. The two chosen vectors are $(\mathbf{c}_a - \mathbf{p})$ and $(\mathbf{c}_b - \mathbf{p})$ because they provide a faster and more obvious kinematic result and because, albeit being on a mobile part, they can never be parallel. First, the velocity of point P can be expressed as

$$\boldsymbol{v}_{P\in S_f/S_i} = \boldsymbol{v}_{C_a\in S_{a3}/S_i} + (\mathbf{c}_a - \mathbf{p}) \times \boldsymbol{\omega}_{S_f/S_i} \tag{2.35}$$

by noticing that $\boldsymbol{v}_{C_a\in S_f/S_i} = \boldsymbol{v}_{C_a\in S_{a3}/S_i}$ because C_a is the location of the joint between S_f and S_{a3}.

Then, the projection on $(\mathbf{c}_a - \mathbf{p})$ can be written as

$$(\mathbf{c}_a - \mathbf{p})^T \boldsymbol{v}_{P\in S_f/S_i} = 0 + (\mathbf{c}_a - \mathbf{p})^T \boldsymbol{v}_{C_a\in S_{a3}/S_i} \tag{2.36}$$

and

$$\boldsymbol{v}_{C_a\in S_{a3}/S_i} = (\mathbf{b}_{a1} - \mathbf{c}_a) \times \boldsymbol{\omega}_{S_{a3}/S_{a1}} + (\mathbf{a}_1 - \mathbf{c}_a) \times \boldsymbol{\omega}_{S_{a1}/S_i}. \tag{2.37}$$

Then, using the fact $\mathbf{a}_1 - \mathbf{c}_a = \mathbf{a}_1 - \mathbf{b}_{a1} + \mathbf{b}_{a1} - \mathbf{c}_a$, one has

$$\boldsymbol{v}_{C_a\in S_{a3}/S_i} = (\mathbf{b}_{a1} - \mathbf{c}_a) \times \boldsymbol{\omega}_{S_{a3}/S_i} + (\mathbf{a}_1 - \mathbf{b}_{a1}) \times \boldsymbol{\omega}_{S_{a1}/S_i}. \tag{2.38}$$

Moreover, the parallelogram architecture gives the obvious result

$$\boldsymbol{\omega}_{S_{a3}/S_i} = \mathbf{0} \tag{2.39}$$

and because by definition $(\mathbf{c}_a - \mathbf{p})$ and $(\mathbf{a}_1 - \mathbf{b}_{a1})$ are collinear, we can write

$$(\mathbf{c}_a - \mathbf{p})^T((\mathbf{a}_1 - \mathbf{b}_{a1}) \times \boldsymbol{\omega}_{S_{a1}/S_i}) = \boldsymbol{\omega}_{S_{a1}/S_i}^T((\mathbf{c}_a - \mathbf{p}) \times (\mathbf{a}_1 - \mathbf{b}_{a1})) \tag{2.40}$$

$$= 0. \tag{2.41}$$

Therefore,

$$(\mathbf{c}_a - \mathbf{p})^T \boldsymbol{v}_{P\in S_f/S_i} = 0. \tag{2.42}$$

A similar reasoning can be applied to obtain

$$(\mathbf{c}_b - \mathbf{p})^T \boldsymbol{v}_{P\in S_f/S_i} = 0. \tag{2.43}$$

Finally, because $(\mathbf{c}_a - \mathbf{p})$ and $(\mathbf{c}_b - \mathbf{p})$ form a base of the planar space since they are never collinear, we have

$$\boldsymbol{v}_{P \in S_f/S_i} = \mathbf{0}. \tag{2.44}$$

Therefore, S_f is constrained to undergo pure rotations around P relative the base frame attached to S_i.

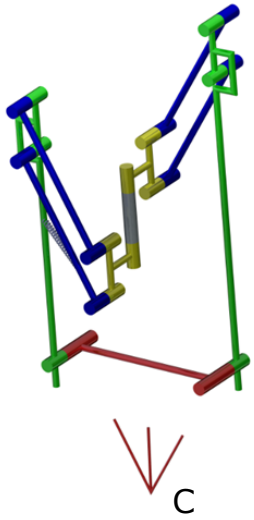

FIGURE 2.12 – CAD model of the novel planar RCC mechanism. The architecture of the mechanism is 2-ΠR, where Π stands for a parallelogram joint. The fixed link is shown in gray colour, the parallelograms are shown in blue, the extension links are shown in green and the end link is shown in red.

A computer aided design (CAD) model of the mechanism is shown in Fig. 2.12.

The mechanism presented above is a planar 2-πR mechanism, where Π stands for a parallelogram joint and R stands for a revolute joint. It is possible to extend the concept to a spatial mechanism by adding another kinematic chain (leg) and modifying the architecture to a 3-πS mechanism, where S stands for a spherical joint. In this case, the terminal link is constrained to undergo pure rotations in 3D space. However, the use of spherical joints is not convenient in practice because of their limited range of motion. Figure 2.13 shows an alternative spatial mechanism that uses only two kinematic chains and that avoids the use of spherical joints. It consists of a 2-RΠH mechanism, where H stands for a Hooke joint. The geometric design of the mechanism is such that the axes of the last revolute joints of the Hooke joints intersect at the centre of the sphere around which the terminal link is constrained to rotate. Although somewhat complex, this solution shows some promising properties. Figure 2.14 shows a possible practical implementation of this concept.

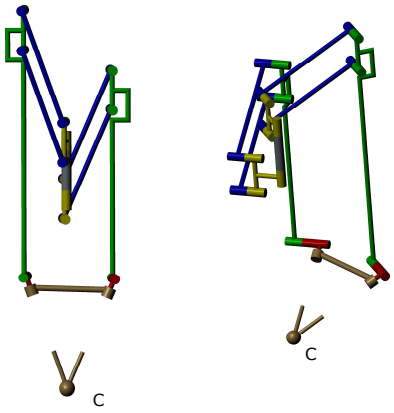

FIGURE 2.13 – CAD model of the novel spatial RCC mechanism. The architecture of the mechanism is 2-RΠRR. The fixed link is shown in gray colour, the parallelograms are shown in blue, the extension links are shown in green and the end link is shown in red. The centre of rotation is indicated.

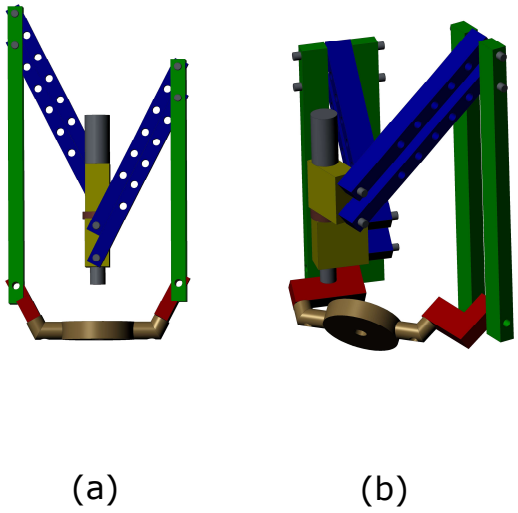

FIGURE 2.14 – CAD model of the novel spatial RCC mechanism. The architecture of the mechanism is 2-RΠRR. The fixed link is shown in gray colour, the parallelograms are shown in blue, the extension links are shown in green and the end link is shown in red.

2.5 CASE STUDY : DESIGN OF A TOOL FOR THE INSERTION OF A SPARK PLUG CABLE IN AN ENGINE ASSEMBLY OPERATION

In order to test the concept of the accuracy correction mechanisms, a specific case of assembly task is studied. The insertion of a spark plug cable on an engine was chosen. This task is rather straightforward along an axis of revolution. The two parts involved are shown in Fig. 2.15. The part on the right-hand side (part B) is screwed to the case of the engine and connects with the inner chamber of the crankrod system to produce the ignition sparks. The part on the left-hand side (part A) connects with the electric power supply and provides the electric energy required for the sparks. The two parts are assembled outside of the case of the engine.

Sensors were used to identify the force required to manually perform the assembly. Displacement was also measured in order to gather information on how much energy is spent during the insertion. The sensor used for the force measurement is an ATI 6-axis force/torque sensor Mini45. Only the magnitude of the force along the insertion axis was needed but this sensor was used for its performance and availability. The displacement was measured with an encoder mounted on a pulley to which a cable was attached. The cable was attached to part A, the encoder was rigidly attached on a fixed frame, one end of the cable is attached to the pulley

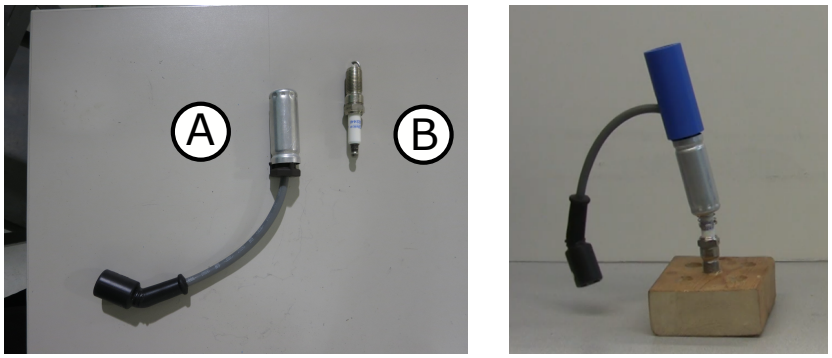

FIGURE 2.15 – The two parts involved in the spark plug assembly task. On the left is the cable (part A) and on the right is the spark plug (part B). The result when A and B are assembled is shown on the right-hand side picture.

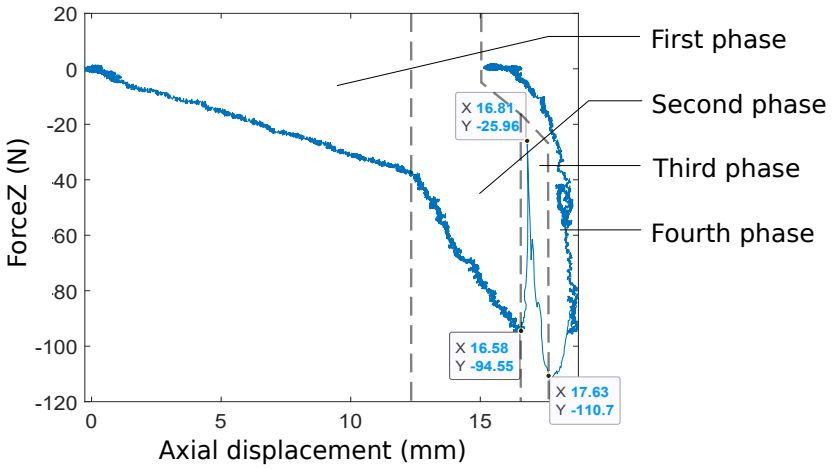

FIGURE 2.16 – Force/displacement behaviour measured during the insertion of the spark plug (a negative force represents a compression force).

of the encoder and wound on it.

The result of the measurements is shown in Fig. 2.16. Four different phases can be observed on the graph. The initial displacement is set to zero, the first phase is an elastic behaviour with a soft slope, the rubber of part A slides along the white plastic part of part B, resulting in the elastic motion resisting behaviour. The force required to continue the insertion increases proportionally to the displacement, the slope being dependent on the materials and on the geometry.

The second phase is another elastic behaviour with a steeper slope, the reason for the change of slope being that part A has then reached the metallic area of part B, which has a larger diameter and therefore produces a larger deformation of the rubber part. It is also possible

that the metallic area of part B induces more friction.

Then, the third phase is a sudden large decrease in the magnitude of the measured compression force accompanied by a fast advance in the displacement, followed by a sudden large increase in the magnitude of the measured force. A "clips" happens during this phase, : to finish the insertion a spherical metallic part in A must bend to close on the spherical shape on B. The variation of the force during this step can be explained as follows. This step requires a force threshold (measured at $95N$) to bend the part. Once this threshold is reached a displacement happens, reducing drastically the needed force until the end stop is reached. The maximum force measured, $110N$, is not really significant because the insertion reached an end stop and cannot go any further. Indeed, with several trials, this maximum force changes depending on the force applied by the operator at the end of the assembly.

The fourth and last phase is a decrease in force to the neutral state with a sharp slope that decreases the displacement. This return motion can be explained as follows : while the other phases were taking place, the rubber part accumulated energy and was deformed. This energy is released when the operator stops applying force and the rubber returns to its neutral undeformed state. When the operator has finished, the measured force reaches zero because no force is applied on the sensor.

2.6 Example mechanism

To study the performance of corrective mechanisms, a prototype has been designed and built. As discussed above, both translational and rotational mobilities can be included in adaptive mechanisms but angular correction devices are more complex to design. Given the insertion tasks targeted in this work, the focus is placed on translations. The targeted assembly task is the spark plug insertion presented in section 2.5, in which a force must be applied along one axis. No correction should be included along this axis to rigidly transfer this force.

The device used to generate the force is an impactor designed for a previous work and adapted to perform the assembly of the spark plug regarding the measurements presented in section 2.5. The detailed design of the impacting device is not described here, its main characteristic is that it generates periodic short span and high magnitude forces along an axis with control over the frequency and the maximum force.

The chosen architecture is a RRC mechanism, which means one serial linkage composed of a revolute joint, another revolute joint and a cylindrical joint. The axes of all three joints are parallel. The two revolute joints form a planar serial mechanism which serves as a two-dimensional positioning correction. The cylindrical joint has a translational axis of movement orthogonal to the plane of correction and conveys the motion provided by the tool to perform the insertion. The rotation allowed by the cylindrical joint helps with the design of the joint.

Indeed, a purely prismatic joint would require a more complex design. Moreover, a cylindrical joint does not conflict with the test parts that have an axial symmetry. Parts with no axial symmetry could require to remove this motion.

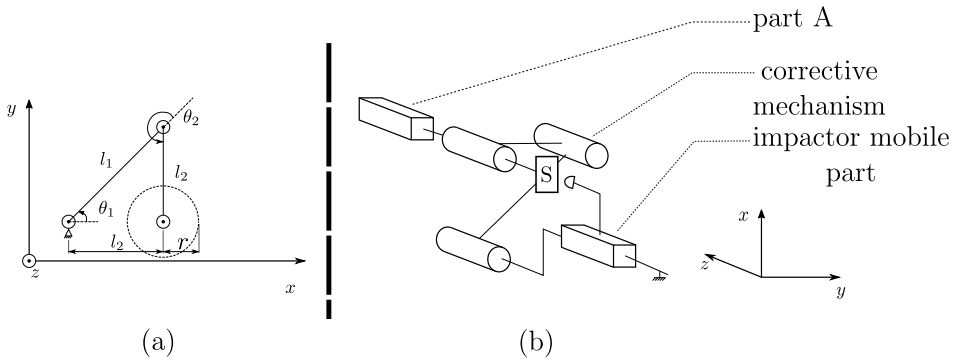

FIGURE 2.17 – Kinematic model of the corrective mechanism used for the assembly of the spark plug cable. (a) is a planar representation of the corrective design, it introduces the parameters used in the equations. The disc workspace is represented with the dashed circle of radius r. (b) is a spatial representation of the complete mechanism with the impactor and part A.

A model of the mechanism is shown in Fig. 2.17. The spatial kinematic model (Fig. 2.17(b)) presents the whole device with the impactor and the correction mechanism. A planar view in the (x, y) plane (Fig. 2.17(a)) shows the correction mechanism and introduces the parameters referred to in the next paragraphs. θ_1 is the angle between the x axis and the first bar, θ_2 is the angle between the first and the second bar, l_1 and l_2 are the respective lengths of these bars. The mechanism is presented in the configuration chosen according to the specifications discussed in the next paragraphs. A CAD model of the prototype is shown in Fig. 2.18.

The elastic return device described in section 2.3 is used in the prototype, more specifically the variant shown in Fig. 2.5. The springs are required to give a neutral position to the mechanism and must be preloaded to avoid unwanted motion from small external efforts such as the weight of the parts of the mechanism. Figure 2.19 shows the inside of the two revolute joints with cut views. The intermediate part, numbered 3 in Fig. 2.5, can be seen linking the two stages of springs in view (b) in Fig. 2.19.

The chosen designs for the mechanical stops for the preloading as well as the design choice to allow a simple assembly and reduced mechanical interferences are shown in Fig. 2.19. These figures also show the use of bearings to reduce friction and other design elements such as spacers. The use of additive manufacturing (3D printing) allowed for a reduced number of parts by combining several specification requirements in some parts.

One major design challenge is the selection of the properties for the springs. Aside from the mechanical design to build the device, the stiffness and the preload of the springs must be

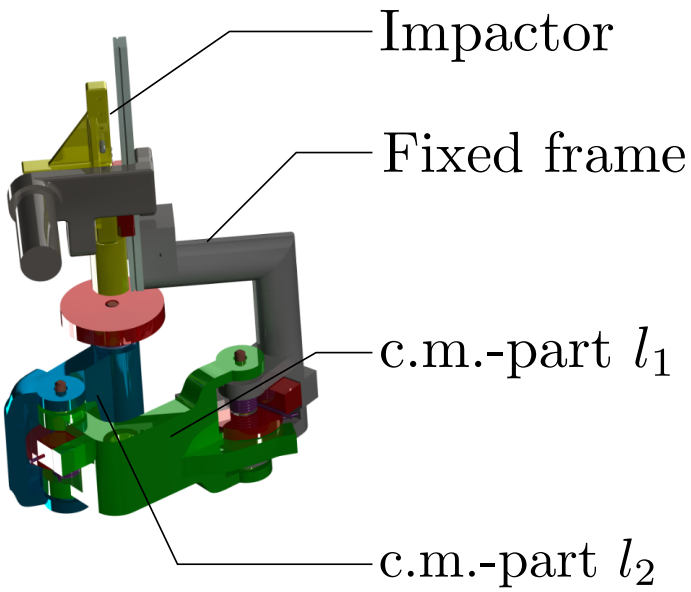

FIGURE 2.18 – Computer generated model of the corrective mechanism (c.m.).

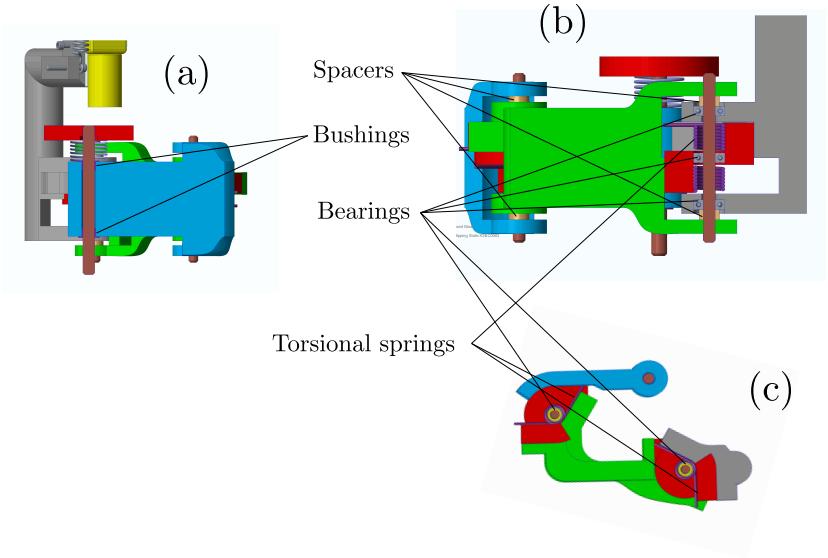

FIGURE 2.19 – View cuts of the torsional spring-loaded joints. (a) is a front view, (b) is a side view and (c) is a top view.

discussed. Considering the chosen mechanical design described above, the estimation of the torque that must be sustained by the springs requires the knowledge of the mathematical relationship between the efforts at the end part and the torques at the joints. To this end, the use of Jacobian matrices is convenient (see Waldron et al. (1985) for instance). The mechanism can be considered as a serial planar robot whose Jacobian matrix can be written as

$$\mathbf{J} = \begin{bmatrix} [-l_1 \sin\theta_1 - l_2 \sin(\theta_1 + \theta_2)] & -l_2 \sin(\theta_1 + \theta_2) \\ [l_1 \cos\theta_1 + l_2 \cos(\theta_1 + \theta_2)] & l_2 \cos(\theta_1 + \theta_2) \end{bmatrix} \tag{2.45}$$

$$\mathbf{t} = \mathbf{J}\dot{\boldsymbol{\theta}} \tag{2.46}$$

where $\mathbf{t}$ is the end link Cartesian velocity defined as $\mathbf{t} = [\dot{x}, \dot{y}]^T$ and $\dot{\boldsymbol{\theta}}$ is the joint velocity vector defined as $\dot{\boldsymbol{\theta}} = [\dot{\theta}_1, \dot{\theta}_2]^T$.

From this matrix, based on the principle of virtual work, the static forces at the joints can be obtained with the following formula

$$\mathbf{c} = \mathbf{J}^T\mathbf{f} \tag{2.47}$$

where $\mathbf{c}$ is the vector of joint torques defined as $\mathbf{c} = [\tau_1, \tau_2]^T$ where τ_i is the torque at joint i and $\mathbf{f}$ is the force vector applied by the end link defined as $\mathbf{f} = [f_x, f_y]^T$. This is a simplified expression of the generalized formula shown in Salisbury and Craig (1982).

The next step is to choose appropriate lengths for l_1 and l_2. These parameters define the workspace of the mechanism. The workspace of the device corresponds to the size of the maximum zone defined by the maximum positioning error that the device can handle. In the case of the spark plug insertion described above, it is estimated that the device should correct a position error corresponding to a disk having a radius of approximately $2.5cm$ around the neutral position. The radius of the disc is referred to as r in what follows. Hence, the Cartesian workspace of the device is a disc of $r = 2.5\ cm$ radius. The centre of the disc is chosen as the neutral configuration of the device so that the range of the device is the same in every direction. Moreover, the neutral configuration and the link lengths are chosen such that for any force applied, the joint torques are the same for each of the two joints(isotropic configuration).

These conditions lead to :

$$l_1 = \sqrt{2}l_2 \tag{2.48}$$

and at the neutral state :

$$\theta_2 = -135°. \tag{2.49}$$

Furthermore, to describe the whole disc without singular states, fully extended or fully folded configurations of the robot must be avoided, leading to the following inequalities

$$l_1 + l_2 \geq r + l_2 \tag{2.50}$$

to avoid the fully extended configuration, which can be reduced to

$$l_1 \geq r \tag{2.51}$$

and

$$l_2 - r \geq l_1 - l_2 \tag{2.52}$$

to avoid the fully folded configuration, which can be reduced to

$$2l_2 - l_1 = (2 - \sqrt{2})l_2 \geq r. \tag{2.53}$$

Moreover, another condition for the device to work properly is to reduce the range between the maximum and the minimum "worst" torques possible so the selection of the springs can be accomplished more carefully and, more importantly, the behaviour of the device can be more consistent. Indeed, when the mechanism is not in its neutral state due to an external force having a magnitude larger than the threshold of the preloaded springs, the joint torques may have very different magnitudes, meaning that the return effect of the springs would be different for each of the joints, which may not be desirable. The worst torque for the second joint is only dependent on the external force and the length of the second link, irrespective of the configuration of the device. The worst torque for the first joint varies with the configuration and with the link lengths. Therefore, the maximum worst torque happens in the farthest location from the joint of the end effector in the disc, with a length of $l_2 + r$, and the minimum worst torque happens in the closest location from the joint of the end effector in the disc, with a length of $l_2 - r$. Figure 2.17 introduces these parameters in view (a). If we denote the scale factor α, we get :

$$\alpha = \frac{c_{1max}}{c_{1min}} \tag{2.54}$$

$$= \frac{l_2 + r}{l_2 - r}. \tag{2.55}$$

This is the ratio of the highest torque divided by the lowest torque induced by the external force on the first joint. The second joint is ideal because the torque perceived only depends on the orientation and magnitude of the external force whereas the torque on the first joint also depends on the configuration of the mechanism. The stiffness of the springs must be chosen according to the maximum torques that we would like them to produce to set the threshold torque at an adequate value. However, it should be kept in mind that the torques produced by the springs must be overcome for the mechanism to move and therefore the intuitiveness when using the device can be very inconsistent if the torque produced by the springs varies too much. Therefore, this scale factor is considered as another design parameter to ensure that

the behaviour of the device does not change too significantly when working in its intended workspace.

A reasonable value for α would be 2 or less in order to obtain a relatively homogeneous behaviour between the joints. Denoting this limit α_{max}, we get :

$$\alpha \leq \alpha_{max} \tag{2.56}$$

which, combining with Eqn.2.55 leads to :

$$l_2 \geq r\left(\frac{\alpha_{max}+1}{\alpha_{max}-1}\right) \tag{2.57}$$

With $\alpha_{max} = 2$ we obtain a minimum value for l_2 of 7.5 cm. Therefore we choose :

$$l_2 = \frac{15}{2}\ cm \tag{2.58}$$

$$l_1 = 15\frac{\sqrt{2}}{2}\ cm \tag{2.59}$$

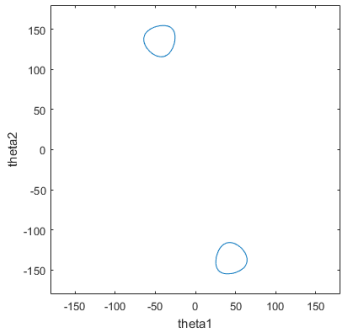

FIGURE 2.20 – Computation of the workspace in the joint space (θ_1, θ_2). The two distinct areas represent the two sets of solutions.

Finally, we obtain the workspace in the joint space, shown in Fig. 2.20. A disk of radius 2.5 cm centred on the neutral configuration in the Cartesian space is defined. Mapping this disk in the joint space using the solution to the Inverse Kinematic Problem (IKP) yields the result shown in Fig. 2.20. The IKP has two different solutions for each Cartesian position, corresponding to two configurations for the mechanism. These two configurations lead to the two areas shown in Fig. 2.20, one for each configuration. The real mechanism would only work in one of the two areas. As it can be observed in Fig. 2.20, a range of motion of approximately 40° is needed for

each joint. This result is very important for the design of the robot. Indeed, the range of motion should not be too restrictive but on the other hand it should not be too large, which would increase the risk of encountering ill-conditioned configurations or mechanical interferences.

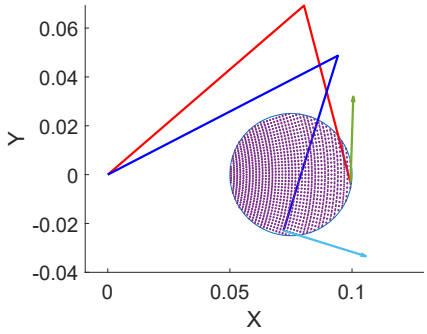

FIGURE 2.21 – Computational result of the numerical search for the largest static torques at the joints depending on the configurations of the mechanism and the orientation of the force. The circle represent the workspace of the device, the red and blue bars represent two different configurations of the mechanism and the arrows indicate the direction of the force. The dots show the end positions computed for the search.

The torques at the joints depend on the external forces on the end part as well as on the configuration of the mechanism. Since the Jacobian matrix of the robot is configuration dependent, the joint space is discretized in order to compute the joint torques for many configurations. The orientation of the force is also an important parameter. The component of the force that is not in the working plane of the mechanism does not influence the joint torques. Therefore, in order to consider the worst case scenario, the external force is assumed to lie in the working plane. The orientation of the force is also discretized. The result is shown in Fig. 2.21, where the circle is the Cartesian workspace described above and the dots are the positions obtained by discretizing the joint space. The external force is applied on the end part at a location referred to as the end point. Two particular configurations for the mechanism are represented, each corresponding to a maximum torque for one of the joints. At the end point of these configurations, the arrow shows the force and more specifically the orientation of the force for which the maximum torque occurs. The second joint goes through a maximum torque when the external force is perpendicular to the lever arm between the second joint and the point of application of the force. As such, the position shown is not unique and can occur in any position as soon as the external force is in the relative orientation described before. In the case of the first joint, the maximum torque happens when the lever arm length is maximum, which corresponds to the configuration where the end point is the furthest from the first joint and the orientation of the external force is perpendicular to the lever arm. Then, the maximum torques correspond to these maximum lever arms times the norm of the applied force.

The main force to be compensate for is the weight, set at 400g (the spark plug has a mass of

approximately $100g$, a safety factor of 4 is used to cover small inertial forces when manipulating the device), we get :

$$T_{1max} = 0.390Nm \tag{2.60}$$

$$T_{2max} = 0.305Nm \tag{2.61}$$

Therefore, the preload values for the springs should be equal or higher than these torques in order to compensate for the weight.

Once the design parameters are established, the prototype can be built. Most parts are made of 3D-printed ABS except for steel rods, springs, bushings and other specific off-the-shelf components. The operation of the prototype is demonstrated in the video presented in section 2.7. As shown in the video, the device works as intended with spark plug connectors and was also easily adapted for hose assembly tasks. The tasks were effectively made easier to perform remotely, within the range of correction designed and discussed above.

2.7 Video documentation

The prototype mechanism is presented in a video, it can be found at [Video hosted on youtube]. The first part of the video shows how the spark plug connector is handled for the tests. Two possible designs of the handler are presented. Each design has conical shapes at the locus of the contact with the spark plug to generate the forces that activate the correction of the position of the connector. The first design focuses on a proper grasp of the part while the force for the insertion is applied on it. A complete counter-shape is designed, opening in two parts using a pivot axis to insert the spark plug connector. A spring-actuated lever mechanically closes the handles firmly to prevent the connector from moving when the handler is closed. The main drawback of this design is that once the assembly task is finished, it is necessary to reach the handler to open it and release the mechanism for another use, which almost defeats the purpose of remote work. The second design addresses this issue. The handler is composed of three parts instead of two. Two symmetrical parts constitute the sides of the case. Torsional springs and mechanical stops produce a naturally open configuration for the handler. The case can slide along an axis parallel to the insertion axis, and carefully placed translational springs push the case upward. For the handler to close, the cases must be pushed back, then closed around the part, and pushed forward in the shape of the third part composing the handler. The translational springs ensure that the case does not fall down and the whole mechanism remains closed. The main advantage of this design is shown in the live test at the end of the video. With this design, when the assembly is completed, simply pulling in the opposite direction of the insertion opens the case and no direct interaction is required from the operator. A handler for hose-type parts is also presented. It works with two parallelogram mechanisms that clamp on the hose to hold it in place.

Afterwards, the corrective mechanism is shown. The force threshold is presented by moving the mechanism around and observing that this motion does not induce any relative motion of the parts. This behaviour is due to the use of preloaded springs. The joint used to convey the insertion force is also presented.

Finally, the whole device is shown in action, the power tool for the insertion being the impactor device mentioned in the article, actuated with a simple switch at the location where the operator is working. An additional test with a hose insertion is also shown. This assembly task was not as thoroughly studied as the spark plug insertion but it worked with minimal changes to the settings used with the spark plug connector. Another handler was designed for the hose insertion, which consists of two parallelograms that match at a configuration where they push against each other to keep the hose tightly held.

2.8 Conclusion

This article presented novel architectures to address accuracy issues in the context of remote, fast and agile assembly tasks. The task presented is a spark plug connector snap on the corresponding spark plug. The kinematic behaviour of several mechanisms was discussed, with a distinction between rotational and translational mechanisms. A prototype of translational mechanism was designed and built to illustrate the concept.

2.9 Bibliographie

MH Ang and Gerry B Andeen. Specifying and achieving passive compliance based on manipulator structure. *IEEE transactions on robotics and automation*, 11(4) :504–515, 1995.

Stefanie Angerer, Christoph Strassmair, Max Staehr, Maren Roettenbacher, and Neil M Robertson. Give me a hand—the potential of mobile assistive robots in automotive logistics and assembly applications. In *2012 IEEE international conference on technologies for practical robot applications (TePRA)*, pages 111–116. IEEE, 2012.

Emilio C Baraldi and Kaminski Paulo C. Ergonomic planned supply in an automotive assembly line. *Human factors and ergonomics in manufacturing & service industries*, 21(1) :104–119, 2011.

Boban Blazevski and Jean D Hallewell Haslwanter. User-centered development of a system to support assembly line worker. In *Proceedings of the 19th International Conference on Human-Computer Interaction with Mobile Devices and Services*, pages 1–7, 2017.

Alexandre Campeau-Lecours, Pierre-Luc Belzile, Thierry Laliberté, Simon Foucault, Boris Mayer-St-Onge, Dalong Gao, and Clément Gosselin. An articulated assistive robot for

intuitive hands-on-payload manipulation. *Robotics and Computer-Integrated Manufacturing*, 48 :182–187, 2017.

Po-Yu Chen and Kuei-Yuan Chan. Improving hole-searching accuracy for peg-in-hole assembly with manipulator harmonic drive uncertainty. In *International Design Engineering Technical Conferences and Computers and Information in Engineering Conference*, volume 59230, page V05AT07A059. American Society of Mechanical Engineers, 2019.

Chin-Boon Chng, Bin Duan, and Chee-Kong Chui. Modeling and simulation of a remote center of motion mechanism. In *Region 10 Conference (TENCON), 2016 IEEE*, pages 1755–1758. IEEE, 2016.

Namik Ciblak and Harvey Lipkin. Design and analysis of remote center of compliance structures. *Journal of Field Robotics*, 20(8) :415–427, 2003.

Alexandher Weslley FTRW de Negreiros, Patrícia Rodrigues da Silva, Pedro Miguel Ferreira Martins Arezes, Roberta Dangelino, and Rosimeire Simprini Padula. Manufacturing assembly serial and cells layouts impact on rest breaks and workers' health. *International Journal of Industrial Ergonomics*, 70 :22–27, 2019.

F. Farahmand, M. T. Pourazad, and Z. Moussavi. An intelligent assistive robotic manipulator. In *2005 IEEE Engineering in Medicine and Biology 27th Annual Conference*, pages 5028–5031, 2005.

Takafumi Fukushima, Eiji Iwata, Jichoel Bea, Mariappan Murugesan, K-W Lee, Tetsu Tanaka, and Mitsumasa Koyanagi. Evaluation of alignment accuracy on chip-to-wafer self-assembly and mechanism on the direct chip bonding at room temperature. In *2010 IEEE International 3D Systems Integration Conference (3DIC)*, pages 1–5. IEEE, 2010.

Dalong Gao, Ninja Huang, Lance Ransom, and Richard Janis. A new robotic hand for automotive sheet panels. In *International Design Engineering Technical Conferences and Computers and Information in Engineering Conference*, volume 59247, page V05BT07A005. American Society of Mechanical Engineers, 2019.

Victor Grosu, Carlos Rodriguez-Guerrero, Svetlana Grosu, Bram Vanderborght, and Dirk Lefeber. Design of smart modular variable stiffness actuators for robotic-assistive devices. *IEEE/ASME Transactions on Mechatronics*, 22(4) :1777–1785, 2017.

Jean D Hallewell Haslwanter and Boban Blazevski. Experiences with an assistive system for manual assembly. In *Proceedings of the 11th PErvasive Technologies Related to Assistive Environments Conference*, pages 46–49, 2018.

S Jahanian, Chris David, D Goodwin, J Bearden, V Baharian, T Poplin, Dan Gerpheide, Clinton Roy, and Troy Simmons. Design of a sprinkler head and hose assembler for physically challenged workers. In *International Design Engineering Technical Conferences and*

Computers and Information in Engineering Conference, volume 37017, pages 1027–1033, 2003.

Sung C Kang, Yong K Hwang, Mun S Kim, Chong-Won Lee, and Kyo-Il Lee. A compliant motion control for insertion of complex shaped objects using contact. In *Robotics and Automation, 1997. Proceedings., 1997 IEEE International Conference on*, volume 1, pages 841–846. IEEE, 1997.

Byoung-Ho Kim, Sang-Rok Oh, Byung-Ju Yi, and Il Hong Suh. Compliance planning for dextrous assembly tasks using multi-fingered robot hands. *Intelligent Automation & Soft Computing*, 8(1) :51–64, 2002.

Whee-kuk Kim, Byung-Ju Yi, and Whang Cho. Rcc characteristics of planar/spherical three degree-of-freedom parallel mechanisms with joint compliances. *ASME Journal of Mechanical Design*, 122(1) :10–16, 2000.

Songgi Lee, Xin Jiang, Koyu Abe, Satoko Abiko, Atsushi Konno, and Masaru Uchiyama. A human assistant robot system for handling heavy mechanical parts in assembly lines. In *2011 IEEE/SICE International Symposium on System Integration (SII)*, pages 732–737. IEEE, 2011.

Song Liu, Deng-Peng Xing, You-Fu Li, Jianwei Zhang, and De Xu. Robust insertion control for precision assembly with passive compliance combining vision and force information. *IEEE/ASME Transactions on Mechatronics*, 24(5) :1974–1985, 2019.

Xin Rong Liu. The accuracy analysis of parallel mechanism assembly robot. In *Applied Mechanics and Materials*, volume 423, pages 2769–2775. Trans Tech Publ, 2013.

G Michalos, S Makris, N Papakostas, D Mourtzis, and G Chryssolouris. Automotive assembly technologies review : challenges and outlook for a flexible and adaptive approach. *CIRP Journal of Manufacturing Science and Technology*, 2(2) :81–91, 2010.

Sina Modaresahmadi, Casey Nichols, and Wesley Williams. Mechanical design of magnetic gearboxes optimized for assembly. In *ASME International Mechanical Engineering Congress and Exposition*, volume 52071, page V06AT08A012. American Society of Mechanical Engineers, 2018.

Abdullah Mohammed, Bernard Schmidt, and Lihui Wang. Energy-efficient robot configuration for assembly. *Journal of manufacturing science and engineering*, 139(5), 2017.

Reza Movassagh-Khaniki, Neda Hassanzadeh, Abhijit Makhal, and Alba Perez-Gracia. Design of a multi-palm robotic hand for assembly tasks. In *International Design Engineering Technical Conferences and Computers and Information in Engineering Conference*, volume 50169, page V05BT07A079. American Society of Mechanical Engineers, 2016.

J Kenneth Salisbury and John J Craig. Articulated hands : Force control and kinematic issues. *The International journal of Robotics research*, 1(1) :4–17, 1982.

Khushboo Shrivastava and Suhas S Joshi. Design and development of compliant microgripper-based assembly station. In *ASME International Mechanical Engineering Congress and Exposition*, volume 50640, page V010T13A045. American Society of Mechanical Engineers, 2016.

Andreas Stemmer, A Albu-Schaffer, and Gerd Hirzinger. An analytical method for the planning of robust assembly tasks of complex shaped planar parts. In *Robotics and Automation, 2007 IEEE International Conference on*, pages 317–323. IEEE, 2007.

Li Siwei Huang Tian and Derek Chetwynd David Whitehouse. Orientation accuracy synthesis and assembly process design of a3-dof parallel kinematic machine with parallelogram struts. *Chinese Journal of Mechanical Engineering*, (7) :7, 2003.

Isabel Tacão Wagner, Jessica Nogueira Gomes e Silva, Vanessa Rezende Alencar, Nilo Antonio de Souza Sampaio, Antonio Henriques de Araujo Junior, Jose Glenio Medeiros de Barros, and Bernardo Bastos da Fonseca. Ergonomic analysis on the assembly line of home appliance company. In *Congress of the International Ergonomics Association*, pages 116–123. Springer, 2018.

KJ Waldron, Shih-Liang Wang, and SJ Bolin. A study of the jacobian matrix of serial manipulators. 107(2) :230–237, 1985.

Austin Weber. Ohio state tackles assembly line ergonomics. *Assembly*, 56(1) :72–72, 2013.

Daniel E Whitney. Quasi-static assembly of compliantly supported rigid parts. *Journal of Dynamic Systems, Measurement, and Control*, 104(1) :65–77, 1982.

Fuliang Zhao and Paul SY Wu. Vrcc : A variable remote center compliance device. *Mechatronics*, 8(6) :657–672, 1998.

Chen Zhehan, Du Fuzhou, and Tang Xiaoqing. Research on uncertainty in measurement assisted alignment in aircraft assembly. *Chinese Journal of Aeronautics*, 26(6) :1568–1576, 2013.

Guanghua Zong, Xu Pei, Jingjun Yu, and Shusheng Bi. Classification and type synthesis of 1-dof remote center of motion mechanisms. *Mechanism and Machine Theory*, 43(12) : 1585–1595, 2008.

Chapitre 3

KINEMATIC AND WORKSPACE MODELLING OF A 6-PUS PARALLEL MECHANISM

3.1 Résumé

Cet article fut conçu au moment du projet où le travail de conception du robot actif a commencé. Différentes architectures de robots ont été discutées à ce moment, des questions telles que combien de degrés de liberté sont nécessaires, quel format/taille serait idéal ou encore quelles tâches devrait-il accomplir. La question de son architecture est devenue assez vite centrale et le robot présenté dans cet article possède une architecture proche de l'architecture choisie. L'étude présentée ici est alors similaire à celle du robot construit présentée dans l'article suivant. Ainsi, la création de cet article a permis de prendre de l'avance sur les outils de conception utilisé pour le robot final.

L'objet de l'article est l'analyse cinématique d'un mécanisme parallèle six degrés de liberté conventionnellement désigné en tant qu'architecture 6-PUS. Tout d'abord, le problème géométrique inverse est présenté ainsi que les matrices Jacobiennes du robot. Ensuite, un algorithme pour la détermination géométrique de l'espace de travail, soit l'espace atteignable du robot, est présenté. Cet algorithme analytique produit un résultat rapide et précis. Les lieux de singularité du robot sont ensuite étudiés, ainsi que la capacité en force du robot au travers de l'analyse d'un concept de rapport de transmission, présenté au préalable. L'analyse présentée sert d'exemple de conception, les paramètres de conception pouvant être facilement ajustés pour correspondre à des applications spécifiques.

3.2 Abstract

This article presents the kinematic analysis of a six-degree-of-freedom six-legged parallel mechanism of the 6-PUS architecture. The inverse kinematic problem is recalled and the Jacobian matrices are derived. Then, an algorithm for the geometric determination of the workspace is presented, which yields a very fast and accurate description of the workspace of the mechanism. Singular boundaries and a transmission ratio index are then introduced and studied for a set of architectural parameters. The proposed analysis yields conceptual architectures whose properties can be adjusted to fit given applications.

INTRODUCTION

Parallel robots are a family of architectures that provide an alternative to the serial robots widely used in industry. Merlet (2006) deals with the topic of parallel robots generally. Their high dynamic efficiency comes at the expense of a trade-off on workspace and ease of control. Therefore, the architecture of a parallel robot must be carefully chosen depending on the task. Many parallel architectures have been studied over the last decades in order to expand the set of usable parallel robots in industry. Arguably, the most famous parallel robot architecture is the Gough-Stewart platform. This six-degree-of-freedom (dof) architecture has high dynamic capabilities but also complex kinematics and singularities, which explains the large number of papers dealing with it. Gough and Whitehall (1962) and Stewart (1965) are among the first papers dealing with this robot, while Husty (1996) derives a general polynomial solution to its forward kinematic problem. Parallel robots are still a relevant subject of research nowadays and many papers on the topic are published. For instance Bi and Jin (2011) and Zoppi et al. (2010) study a rigid parallel mechanism for milling tasks. The shorter kinematic chains between the fixed frame and the effector reduces the cumulative error on the actuated joints and generally makes parallel robots good contendents for high precision tasks like surgery(Pisla et al. (2008); Wang et al. (2013)). The Gough-Stewart platform has as many legs as the degrees of freedom at the effector with one actuator on each chain. However, many variations exist. Monsarrat and Gosselin (2001) presents a 6-DOF robot with only 3 legs and 2 actuators in each leg. Another variation is a blend of serial and parallel aspects like in Wu et al. (2015). DELTA robots are common robots in industry, Gritsenko et al. (2017) presents a solution to the forward kinematics and Maya et al. (2013) derives the workspace of a variant of the DELTA robot. Singular configurations are one of the main issues in the development and use of parallel mechanisms. Indeed, their complex kinematics easily produces many configurations where some direction of motion can no longer be controlled, thereby limiting the usable space of the robot. The answer to this problem requires a careful design and has been the topic of many articles on the subject like for instance Horin and Shoham (2008); Hsiao and Perng (1997); Yang et al. (2002); Hu et al. (2009). The fundamental work on robotic architectures is the derivation of the kinematic equations. Many works like Maldonado-Echegoyen et al. (2015);

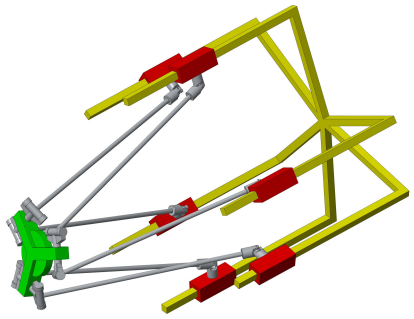

FIGURE 3.1 – EXAMPLE ARCHITECTURE FOR THE 6-PUS PARALLEL ROBOT.

Berbyuk and Johannesson (2005); Chen et al. (2013); Pierrot and Company (1999); Sun et al. (2004); Zhao et al. (2006); Li et al. (2010); Wu et al. (2007) present such equations for specific parallel mechanisms. In this paper, the kinematic analysis of a parallel robot similar to the one introduced in Abtahi et al. (2008); Merlet and Gosselin (1991); Benea (1996) is presented, the geometric equations to determine its workspace are derived and its advantages are discussed with a singularity and force transmission analysis. The architecture studied here can also be considered as an extension of the 3-DOF mechanism proposed in Carretero et al. (2000) to a 6-DOF mechanism.

ARCHITECTURE OF THE MANIPULATOR

An example of the architecture studied in this paper is presented in Fig. 3.1. It consists of a six-dof spatial parallel manipulator which can be described as $6-\underline{P}US$ manipulator, namely each leg includes, from base to platform, an actuated prismatic joint, a passive Hooke joint, an intermediate link and a passive spherical joint attached to the platform. No special geometry is assumed for the placement or orientation of the prismatic joints or for the arrangement of the joints on the platform. The architecture allows 3 independent translations and 3 independent rotations, controlled by 6 actuators, one in each leg.

KINEMATIC MODEL

The notation used in the kinematic model is shown in Fig. 3.2. Point O is arbitrarily chosen as a reference point on the fixed frame. Point P is the reference point for the mobile frame attached to the end effector. The legs are referred to using index i, where i varies from 1 to 6. A_i is the reference point on the axis of the prismatic actuator that sets the 0 for the

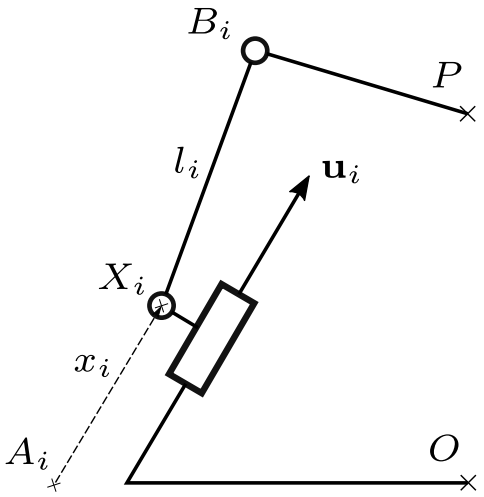

FIGURE 3.2 – KINEMATIC MODEL OF ONE LEG OF THE 6-DOF PARALLEL ROBOT.

corresponding length parameter x_i, it is a constant parameter. The constant vector $\mathbf{u}_i$ is the direction unit vector for the axis of the prismatic actuator. X_i is the point on the axis of the prismatic actuator whose position is determined by the length parameter x_i. X_i is also the location of the universal joint linking the mobile carriage mounted on the prismatic joint and the intermediate link. l_i is the length of this link. B_i is the location of the spherical joint connecting the intermediate link to the platform. The coordinates of point B_i are expressed in the mobile frame whose origin is P.

The joint coordinates are the displacement parameters along the prismatic joints referred to as x_i in Fig. 3.2.

The orientation of the platform (Cartesian coordinates) is represented by a matrix using the Tilt & Torsion angles as described in Bonev et al. (2002). The Tilt is an angle (referred to as θ in the mathematical model) around an axis in the $x-y$ base plane whose direction is defined by an angle ϕ and the Torsion is an angle (referred to as σ in the mathematical model) around an axis orthogonal to the plane defined by three attachment points on the effector (B_1, B_2 and B_3).

The matrix defining the orientation of the platform is then written as

$$\mathbf{R}(\phi,\theta,\sigma) = \begin{bmatrix} C_\phi C_\theta C_{\sigma-\phi} - S_\phi S_{\sigma-\phi} & -C_\phi C_\theta S_{\sigma-\phi} - S_\phi C_{\sigma-\phi} & C_\phi S_\theta \\ S_\phi C_\theta C_{\sigma-\phi} + C_\phi S_{\sigma-\phi} & -S_\phi C_\theta S_{\sigma-\phi} + C_\phi C_{\sigma-\phi} & S_\phi S_\theta \\ -S_\theta C_{\sigma-\phi} & S_\theta S_{\sigma-\phi} & C_\theta \end{bmatrix}, \tag{3.1}$$

where "C" stands for "cosine" and "S" stands for "sine".

Any point B_i on the platform has the resulting position vector $\mathbf{b}_i$, which can be written as

$$\mathbf{b}_i = \mathbf{R}(\mathbf{b}_{i0} - \mathbf{p}_0) + \mathbf{p} \tag{3.2}$$

with $\mathbf{b}_{i0}$ the position vector of B_i in a configuration chosen as the reference configuration, which is defined by $\phi = \theta = \sigma = 0$ and $\mathbf{p} = \mathbf{p}_0$ and where $\mathbf{p}$ the position vector of P, the origin of the mobile frame.

SOLUTION OF THE INVERSE KINEMATIC PROBLEM

Referring to the notations previously introduced, $\mathbf{a}_i$, $\mathbf{b}_i$ and $\mathbf{u}_i$ are point and direction vectors of symbols presented at Fig. 3.2. The inverse kinematic problem is derived using the following kinematic constraint equations

$$l_i^2 = (\mathbf{a}_i + x_i\mathbf{u}_i - \mathbf{b}_i)^T(\mathbf{a}_i + x_i\mathbf{u}_i - \mathbf{b}_i) \tag{3.3}$$

$$= \mathbf{a}_i^T\mathbf{a}_i + \mathbf{b}_i^T\mathbf{b}_i + x_i^2 + 2x_i\mathbf{a}_i^T\mathbf{u}_i - 2\mathbf{b}_i^T(\mathbf{a}_i + x_i\mathbf{u}_i) \tag{3.4}$$

hence the solution of this second degree polynomial equation gives 2 solutions for the articular coordinates, x_i. This applies to all 6 legs, yielding $2^6 = 64$ different combinations of solutions for the joint coordinates. The 2 solutions for each leg can be written as

$$x_{i1} = -\mathbf{u}_i^T(\mathbf{a}_i - \mathbf{b}_i) + \sqrt{\Delta} \tag{3.5}$$

$$x_{i2} = -\mathbf{u}_i^T(\mathbf{a}_i - \mathbf{b}_i) - \sqrt{\Delta} \tag{3.6}$$

$$\Delta = (\mathbf{u}_i^T(\mathbf{a}_i - \mathbf{b}_i))^2 - (\mathbf{a}_i^T\mathbf{a}_i + \mathbf{b}_i^T\mathbf{b}_i - l_i^2 - 2\mathbf{b}_i^T\mathbf{a}_i). \tag{3.7}$$

JACOBIAN MATRICES

The Jacobian matrices provide the relation between the joint velocities and the Cartesian velocities. Here these matrices can be obtained through the differentiation of Eqn. (3.4) with respect to time. The velocity of the points on the mobile frame can be expressed as

$$\dot{\mathbf{b}}_i = \dot{\mathbf{p}} + \boldsymbol{\omega} \times (\mathbf{b}_i - \mathbf{p}) \tag{3.8}$$

where $\boldsymbol{\omega}$ is the vector of angular velocity of the platform.

The architecture of the robot introduces constraint equations on which the derivation of the Jacobian matrices is based. The differentiation of Eqn. (3.4) with respect to time yields

$$0 = \dot{x}_i(x_i + \mathbf{a}_i^T\mathbf{u}_i - \mathbf{b}_i^T\mathbf{u}_i) + (\mathbf{b}_i^T - (\mathbf{a}_i + x_i\mathbf{u}_i)^T)\dot{\mathbf{b}}_i. \tag{3.9}$$

which can be written in matrix form as

$$\mathbf{K}\dot{\mathbf{x}} = \mathbf{J}\mathbf{t} \tag{3.10}$$

with

$$\dot{\mathbf{x}} = \begin{bmatrix} \dot{x}_1 & \dot{x}_2 & \dot{x}_3 & \dot{x}_4 & \dot{x}_5 & \dot{x}_6 \end{bmatrix}^T \tag{3.11}$$

$$\mathbf{t} = \begin{bmatrix} \boldsymbol{\omega}^T & \dot{\mathbf{p}}^T \end{bmatrix}^T \tag{3.12}$$

$$\mathbf{K} = diag(x_i + \mathbf{a}_i^T \mathbf{u}_i - \mathbf{b}_i^T \mathbf{u}_i) \qquad i \in [1, \ldots, 6] \tag{3.13}$$

$$\mathbf{J} = \begin{bmatrix} ((\mathbf{b}_1 - \mathbf{p}) \times (\mathbf{b}_1 - \mathbf{a}_1 - x_1\mathbf{u}_1))^T & (\mathbf{b}_1 - \mathbf{a}_1 - x_1\mathbf{u}_1))^T \\ ((\mathbf{b}_2 - \mathbf{p}) \times (\mathbf{b}_2 - \mathbf{a}_2 - x_2\mathbf{u}_2))^T & (\mathbf{b}_2 - \mathbf{a}_2 - x_2\mathbf{u}_2))^T \\ ((\mathbf{b}_3 - \mathbf{p}) \times (\mathbf{b}_3 - \mathbf{a}_3 - x_3\mathbf{u}_3))^T & (\mathbf{b}_3 - \mathbf{a}_3 - x_3\mathbf{u}_3))^T \\ ((\mathbf{b}_4 - \mathbf{p}) \times (\mathbf{b}_4 - \mathbf{a}_4 - x_4\mathbf{u}_4))^T & (\mathbf{b}_4 - \mathbf{a}_4 - x_4\mathbf{u}_4))^T \\ ((\mathbf{b}_5 - \mathbf{p}) \times (\mathbf{b}_5 - \mathbf{a}_5 - x_5\mathbf{u}_5))^T & (\mathbf{b}_5 - \mathbf{a}_5 - x_5\mathbf{u}_5))^T \\ ((\mathbf{b}_6 - \mathbf{p}) \times (\mathbf{b}_6 - \mathbf{a}_6 - x_6\mathbf{u}_6))^T & (\mathbf{b}_6 - \mathbf{a}_6 - x_6\mathbf{u}_6))^T \end{bmatrix} \tag{3.14}$$

where $\dot{\mathbf{x}}$ is the vector of joint velocities, $\mathbf{t}$ the vector of Cartesian velocities, $\mathbf{K}$ and $\mathbf{J}$ are the Jacobian matrices of the robot.

REACHABLE SPACE

One important topic in the analysis of a manipulator is the determination of the workspace that the manipulator can reach. This workspace is the union of the 6 workspaces allowed by each leg (sometimes referred to as the vertex spaces). The workspace of one leg is illustrated in Fig. 3.3. It is composed of one cylinder whose axis is the axis of the prismatic joint limited by the minimum and maximum values of the prismatic joint and one half-sphere at each end of the cylinder to close the volume. When the intermediate link is orthogonal to the prismatic axis, a type I singular configuration is reached. Therefore, the half-sphere is always on the same side of the plane orthogonal to the prismatic axis and hollows the volume at one end while extending it at the other end. This volume represents the reachable space of the point attached to the platform, namely point B_i. However for the union of the six volumes, the reference point must be the same. For a given orientation, this volume must be translated from point B_i to point P through vector $\mathbf{R}(\mathbf{b}_{i0} - \mathbf{p}_0)$.

The Cartesian equation of the cylinder is given by the limits of existence in $\mathbb{R}$ of the solution of the inverse kinematic problem which is equivalent to the discriminant of the polynomial in Eqn. (3.4) reaching 0, i.e.,

$$\Delta = (\mathbf{u}_i^T(\mathbf{a}_i - \mathbf{b}_i))^2 - (\mathbf{a}_i^T\mathbf{a}_i + \mathbf{b}_i^T\mathbf{b}_i - l_i^2 - 2\mathbf{b}_i^T\mathbf{a}_i) \tag{3.15}$$

$$= (\mathbf{u}_i^T(\mathbf{a}_i - \mathbf{b}_i))^2 - ((\mathbf{a}_i - \mathbf{b}_i)^T(\mathbf{a}_i - \mathbf{b}_i) - l_i^2) \tag{3.16}$$

$$= 0 \tag{3.17}$$

which can be rewritten as

$$(\mathbf{a}_i - \mathbf{b}_i)^T(\mathbf{a}_i - \mathbf{b}_i) - (\mathbf{u}_i^T(\mathbf{a}_i - \mathbf{b}_i))^2 = l_i^2 \tag{3.18}$$

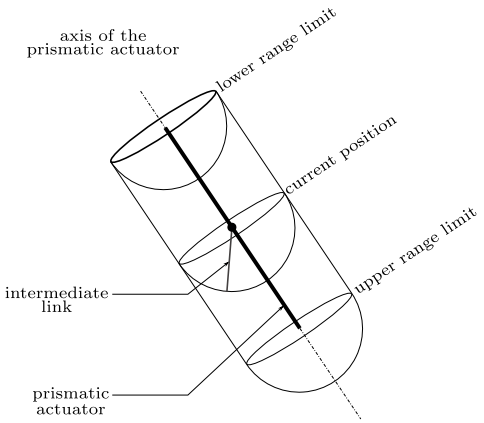

FIGURE 3.3 – REPRESENTATION OF THE REACHABLE WORKSPACE FOR ONE LEG.

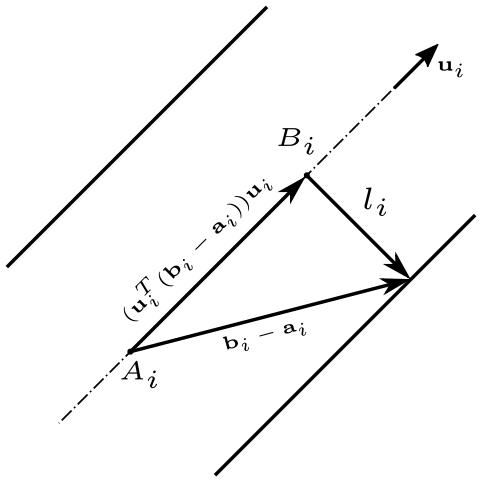

FIGURE 3.4 – ILLUSTRATION OF THE GEOMETRICAL MEANING OF EQN. (3.18).

which is the general equation of a cylinder. The geometrical interpretation of this equation is illustrated at Fig. 3.4, each point on the cylinder is described using the Pythagorean theorem.

The Cartesian equation for the half-sphere is the equation of the sphere around one of the end points along the prismatic joint limited to one side of the plane orthogonal to the prismatic axis. The limit points that define the range of the i_{th} prismatic actuator are referred to as X_{1i} and X_{2i}. The implicit equations of the spheres at these points are

$$(\mathbf{c} - \mathbf{x}_{1i})^T(\mathbf{c} - \mathbf{x}_{1i}) = l_i^2 \tag{3.19}$$

$$(\mathbf{c} - \mathbf{x}_{2i})^T(\mathbf{c} - \mathbf{x}_{2i}) = l_i^2 \tag{3.20}$$

where $\mathbf{x}_{ij}$ is the position vector of point X_{ij} and where one has $\mathbf{c} = [x \quad y \quad z]^T$. Similarly, the

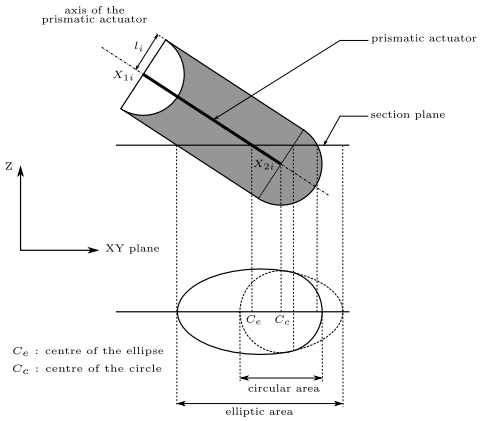

FIGURE 3.5 – SECTION OF THE REACHABLE WORKSPACE FOR ONE LEG.

equations for the limit planes are :

$$\mathbf{c}^T\mathbf{u}_i = \mathbf{x}_{1i}^T\mathbf{u}_i \tag{3.21}$$

$$\mathbf{c}^T\mathbf{u}_i = \mathbf{x}_{2i}^T\mathbf{u}_i. \tag{3.22}$$

In order to represent planar sections of the reachable workspace, it is desired to intersect the reachable volumes of the legs with a section plane. The reachable volume of one leg and the result of the intersection of such a volume with a plane is shown in Fig. 3.5. All the possible cases that can occur for a section of this volume are shown in Fig. 3.6. When slicing the volume, the two half-spheres can be encountered (case 9), the two half-spheres and the cylinder (cases 1, 2 and 3), one half-sphere and the cylinder (cases 4, 5 and 6), only the cylinder (case 7) or only one half-sphere (case 8). The volume of the reachable space of one leg has been described as an assembly of 3 distinct simple volumes, therefore a section of this volume is also an assembly of simple sections, respectively part of a disc, part of an ellipse and another part of a disc. Depending on where the section is placed, these sections can appear or not and can assemble in many variations as shown in Fig. 3.6. The transition between the volumes occurs on two parallel planes normal to $\mathbf{u}_i$ containing respectively X_{1i} and X_{2i}, therefore the transition between the sections occurs at the intersection of these planes with the section plane which generally produces two parallel lines. More precisely, only the situation in which the projection of each sphere on the corresponding plane, which are discs, are crossed by the section plane will result in a transition between the circle, obtained by intersecting the sphere, and the ellipse, obtained by intersecting the cylinder. The representation shown in Fig. 3.7 is obtained using the following process : does a sphere intersect with the section plane ? If it is the case, does the corresponding circle intersect with the transition line ? If it is the case the circle and the ellipse are derived in parametric polar form from Eqn. (3.19) or Eqn. (3.20) and Eqn. (3.18) and then drawn. If the circle does not intersect with the line, if it belongs to the

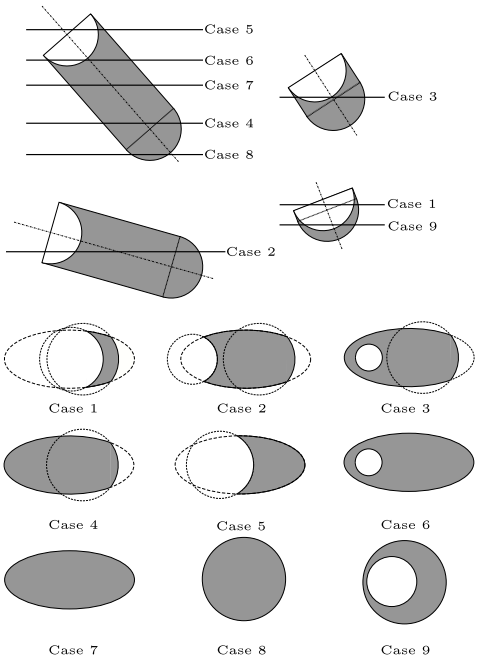

FIGURE 3.6 – PRESENTATION OF THE DIFFERENT CASES WHEN SLICING THE WORKSPACE OF ONE LEG.

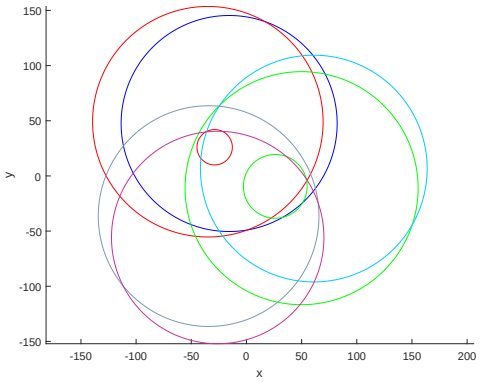

FIGURE 3.7 – REPRESENTATION OF A SECTION OF THE REACHABLE SPACE OF EACH OF THE LEGS FOR $z = 120$ AND ($\phi = 0°$,$\theta = 20°$,$\psi = 0°$).

right side of the line then it is drawn. For all the preceding cases not already implying the ellipse, detect if it belongs to the right area bounded by the lines and draw it if it is the case.

An example set of design parameters is given in Table 3.1. The sections of the reachable volumes of each leg are presented in Fig. 3.7, for a section plane defined as $z = 120$ and an orientation of the platform given by ($\phi = 0°$,$\theta = 20°$,$\psi = 0°$). The intersection of these planar regions are presented in Fig. 3.8 which shows a section of the reachable volume of the manipulator.

TABLE 3.1 – FIRST SET OF PARAMETERS FOR THE DESIGN OF THE ROBOT.

vector	coordinate x	coordinate y	coordinate z
$\mathbf{a}_1$	4	34	0
$\mathbf{a}_2$	-4	40	0
$\mathbf{a}_3$	-31	13.5	0
$\mathbf{a}_4$	-32.5	-23.5	0
$\mathbf{a}_5$	27.5	-20.5	0
$\mathbf{a}_6$	36.5	-16.5	0
$\mathbf{b}_{10}$	0	2.3	0
$\mathbf{b}_{20}$	2	-1.15	0
$\mathbf{b}_{30}$	-2	-1.15	0
$\mathbf{b}_{40}$	0	2.3	0
$\mathbf{b}_{50}$	2	-1.15	0
$\mathbf{b}_{60}$	-2	-1.15	0
$\mathbf{u}_1$	-0.18	0.29	0.94
$\mathbf{u}_2$	-0.28	0.2	0.94
$\mathbf{u}_3$	-0.16	-0.3	0.94
$\mathbf{u}_4$	-0.03	-0.34	0.94
$\mathbf{u}_5$	0.34	0.03	0.94
$\mathbf{u}_6$	0.31	0.14	0.94

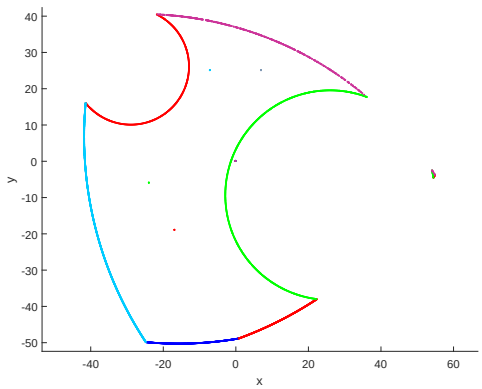

FIGURE 3.8 – SECTION OF THE WORKSPACE OF THE EXAMPLE MANIPULATOR FOR $z = 120$ AND ($\phi = 0°$,$\theta = 20°$,$\psi = 0°$).

The workspace analysis presented here is completely general and does not assume any special geometry. Moreover, it is based on geometric considerations and directly yields to analytical formulations. Therefore, no discretization is required and the computations are very efficient, which yields an interactive representation of the workspace that can be very useful to the designer.

Rendered representations made with a CAD software (CREO 3.0) show the 3D volume of the

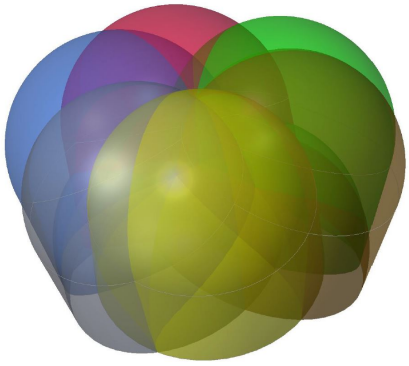

FIGURE 3.9 – RENDERED REPRESENTATION OF THE WORKSPACE VOLUMES OF EACH LEG FOR ($\phi = 0°$,$\theta = 0°$,$\psi = 0°$).

FIGURE 3.10 – RENDERED REPRESENTATION OF THE WORKSPACE VOLUME OF THE INTERSECTION OF EACH LEG WORKSPACE FOR ($\phi = 0°$,$\theta = 0°$,$\psi = 0°$).

workspace of the robot in Fig. 3.9 and in Fig. 3.10.

SINGULARITY ANALYSIS

Type 2 singularities are generally studied for parallel manipulators. They correspond to a loss of control over one or many of the degrees of freedom of the end-effector. Parallel robots are prone to such singular configurations and therefore a singularity analysis is required in order to complement the workspace analysis, i.e., in order to ensure that the workspace is free of singular configurations. Type 2 singularities can be tracked with matrix **J** which loses its full rank when a type 2 singularity is encountered. This can be measured through the determinant of this matrix which vanishes when the rank of the matrix is reduced. In order to obtain the locus of points in the workspace where the determinant of **J** vanishes, the sign of $Det(\mathbf{J})$ is checked and a boundary is detected when the sign changes. Results for two different given orientations are presented in Fig. 3.11 and in Fig. 3.12, in the left column. The value

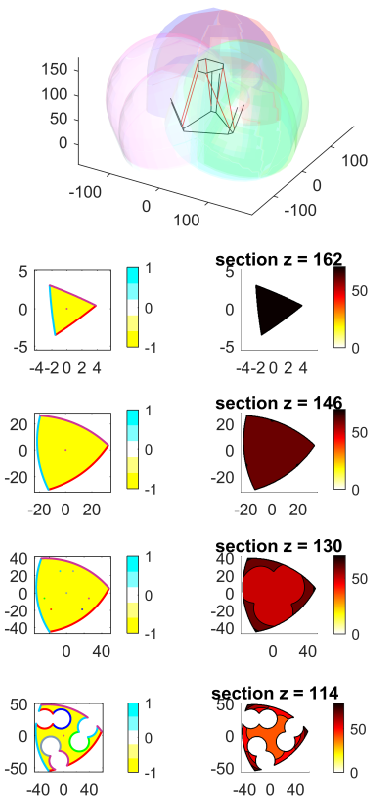

FIGURE 3.11 – ILLUSTRATION OF THE SINGULARITY LOCUS AND THE FORCE TRANSMISSION RATIOS OF THE ROBOT FOR AN INPUT FORCE ALONG THE Z AXIS FOR 4 EVENLY SPACED SECTIONS BETWEEN $z = 114$ AND $z = 162$ FOR A GIVEN ORIENTATION ($\phi = 0°$,$\theta = 0°$,$\psi = 0°$).

of $sign(Determinant(\mathbf{J}))$ is computed and the singularity loci can be observed. In the first orientation no singular configurations are met because in all the sections the color in the workspace is completely uniform therefore the sign of $Det(\mathbf{J})$ remains the same. Whereas in the second orientation singular configurations are met because two different colors exist in the workspace therefore a shift in the sign of $Det(\mathbf{J})$ occurs.

FORCE CAPABILITIES

Many indices exist to evaluate the efficiency of a robot, such as dexterity, kinematic sensibility or agility. Here it is proposed to evaluate the transmission ratio of the mechanism for chosen

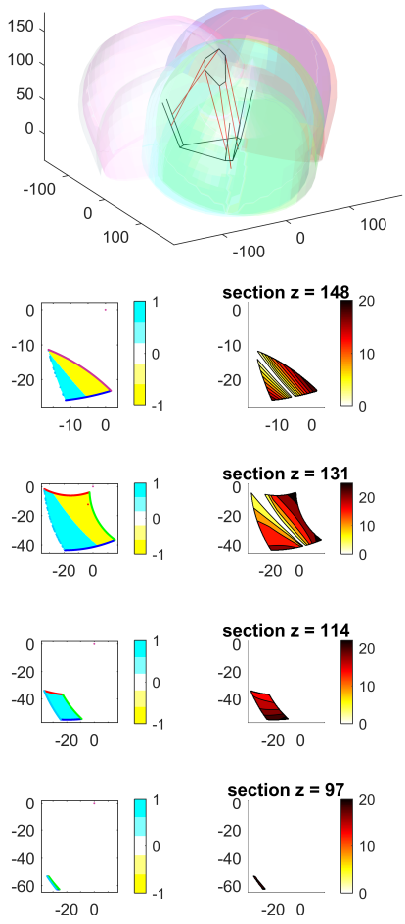

FIGURE 3.12 – ILLUSTRATION OF THE SINGULARITY LOCUS AND THE FORCE TRANSMISSION RATIOS OF THE ROBOT FOR AN INPUT FORCE ALONG THE Z AXIS FOR 4 EVENLY SPACED SECTIONS BETWEEN $z = 97$ AND $z = 148$ FOR A GIVEN ORIENTATION ($\phi = 25°$,$\theta = 70°$,$\psi = 0°$).

force and moment direction so that instead of tracking the worst aspect of the manipulator, its capabilities for dedicated tasks are determined. The process consists in choosing a unit vector as the direction of the effort to be generated at the end-effector, then calculate the corresponding required effort needed at the actuators with Eqn. (3.24), divide the value by the maximum absolute value of the actuated actuated joint efforts and finally calculate the corresponding end-effector efforts with Eqn. (3.25). The result gives the normalized potential maximum effort at the end-effector in the chosen direction. The relations used being linear,

multiplying the result by the maximum joint effort available (given by the specifications of the actuator) gives the force capability in the chosen direction in the considered configuration. However, if the actuators are not homogeneous (revolute and prismatic actuators) or if their specifications differ (different torque capabilities), coefficients should be applied when normalizing the joint efforts to keep the consistency of the results. Moreover, forces and moments at the end-effector should remain separated when choosing the direction because of their different nature.

The method used to determine the relations between the actuation efforts and the end-effector efforts is the conservation of power. It does not consider either non conservative efforts such as friction nor inertial effects. This relation is valid if the inertial forces are low (low mass/inertia parts) or during quasi-static motions. One has

$$\dot{\mathbf{x}}^T \boldsymbol{\tau} = \mathbf{t}^T \mathbf{f} \tag{3.23}$$

where $\boldsymbol{\tau}$ is the array containing the forces (or torques) at the actuated joints and $\mathbf{f}$ the wrench (forces and torques) at the end-effector. Combining this expression with Eqn. (3.10) yields

$$\boldsymbol{\tau} = \mathbf{K}^T \mathbf{J}^{-T} \mathbf{f} \tag{3.24}$$

and

$$\mathbf{f} = \mathbf{J}^T \mathbf{K}^{-T} \boldsymbol{\tau}. \tag{3.25}$$

Like with the singularity analysis, for each section of the workspace along the Z-axis, the transmission ratio is computed for each configuration for an input force along the Z axis. The results are shown in Fig. 3.11 and in Fig. 3.12, in the right column. The singular boundaries noticed in the left column correspond to curves where the transmission ratio is 0, which was expected.

DISCUSSION

The analytic equations developed in this article provide tools to compute quickly and efficiently the workspace of this robot architecture. It is useful when designing a robot with this architecture for a prescribed workspace in connection with a given application. Changing the direction of the $\mathbf{u}_i$ vectors enables to divide the distribution of the load on the actuators and the structure as desired. Unlike in the classical Gough-Stewart platform, in the architecture studied here, the direction of the prismatic actuators is fixed, leading to a reduction of the moving mass and therefore improving the efficiency.

CONCLUSION

The kinematic equations of the 6-PUS parallel robot have been presented. The equations for the generation of the workspace have been studied and the singularity boundaries within this

workspace have been computed. The force capability of the manipulator has also been discussed. The architecture presents interesting low mechanical interference issues and seemingly good usable workspace considering the reachable space and the singularity boundaries.

3.3 Bibliographie

Mansour Abtahi, Hodjat Pendar, Aria Alasty, and Gholamreza Vossoughi. Kinematics and singularity analysis of the hexaglide parallel robot. In *ASME 2008 International Mechanical Engineering Congress and Exposition*, pages 37–43. American Society of Mechanical Engineers, 2008.

Romulus Benea. *Contribution à l'étude des robots pleinement parallèles de type 6 R-RR-S*. PhD thesis, Université Savoie Mont Blanc, 1996.

Viktor Berbyuk and Lars Johannesson. Optimal kinematic design of gantry parallel robots. In *ASME 2005 International Design Engineering Technical Conferences and Computers and Information in Engineering Conference*, pages 1043–1050. American Society of Mechanical Engineers, 2005.

Zhuming M Bi and Y Jin. Kinematic modeling of exechon parallel kinematic machine. *Robotics and Computer-Integrated Manufacturing*, 27(1) :186–193, 2011.

IA Bonev, D Zlatanov, and CM Gosselin. Advantages of the modified euler angles in the design and control of pkms. In *2002 Parallel Kinematic Machines International Conference*, pages 171–188. Citeseer, 2002.

JA Carretero, RP Podhorodeski, MA Nahon, and Clement M Gosselin. Kinematic analysis and optimization of a new three degree-of-freedom spatial parallel manipulator. *ASME Journal of mechanical design*, 122(1) :17–24, 2000.

Qiaohong Chen, Zhi Chen, Xinxue Chai, and Qinchuan Li. Kinematic analysis of a 3-axis parallel manipulator : the p3. *Advances in Mechanical Engineering*, 5 :589156, 2013.

VE Gough and SG Whitehall. Universal tyre test machine. In *Proc. FISITA 9th Int. Technical Congress*, pages 117–137, 1962.

Igor Gritsenko, Askar Seidakhmet, Azizbek Abduraimov, Pavel Gritsenko, and Abay Bekbaganbetov. Delta robot forward kinematics method with one root. In *Robotics and Automation Sciences (ICRAS), 2017 International Conference on*, pages 39–42. IEEE, 2017.

Patricia Ben Horin and Moshe Shoham. A class of parallel robots practically free of parallel singularities. *ASME Journal of Mechanical Design*, 130(5) :052303, 2008.

Lin Hsiao and Ming-Hwei Perng. Inverse kinematic solutions for parallel robots with singularity robustness. In *Circuits and Systems, 1997. Proceedings of the 40th Midwest Symposium on*, volume 1, pages 501–504. IEEE, 1997.

Ying Hu, Zhong Wan, Junfeng Yao, and Jianwei Zhang. Singularity and kinematics analysis for a class of PPUU mobile parallel robots. In *Robotics and Biomimetics (ROBIO), 2009 IEEE International Conference on*, pages 812–817. IEEE, 2009.

Manfred L Husty. An algorithm for solving the direct kinematics of general stewart-gough platforms. *Mechanism and Machine Theory*, 31(4) :365–379, 1996.

Bin Li, Xinhua Zhao, and Guangzhu Meng. Kinematics analysis of a novel over-constrained parallel manipulator. In *Robotics and Biomimetics (ROBIO), 2010 IEEE International Conference on*, pages 489–494. IEEE, 2010.

R Maldonado-Echegoyen, Eduardo Castillo-Castañeda, and MA Garcia-Murillo. Kinematic and deformation analyses of a translational parallel robot for drilling tasks. *Journal of Mechanical Science and Technology*, 29(10) :4437–4443, 2015.

Mauro Maya, Eduardo Castillo, Alberto Lomelí, Emilio González-Galván, and Antonio Cárdenas. Workspace and payload-capacity of a new reconfigurable delta parallel robot. *International Journal of Advanced Robotic Systems*, 10(1) :56, 2013.

Jean-Pierre Merlet. *Parallel robots*, volume 128. Springer Science & Business Media, 2006.

Jean-Pierre Merlet and Clément Gosselin. Nouvelle architecture pour un manipulateur parallèle à six degrés de liberté. *Mechanism and Machine Theory*, 26(1) :77–90, 1991.

Bruno Monsarrat and Clément M Gosselin. Singularity analysis of a three-leg six-degree-of-freedom parallel platform mechanism based on Grassmann line geometry. *The International Journal of Robotics Research*, 20(4) :312–328, 2001.

Franqois Pierrot and O Company. H4 : a new family of 4-dof parallel robots. In *Advanced Intelligent Mechatronics, 1999. Proceedings. 1999 IEEE/ASME International Conference on*, pages 508–513. IEEE, 1999.

Doina Pisla, Nicolae Plitea, and Calin Vaida. Kinematic modeling and workspace generation for a new parallel robot used in minimally invasive surgery. In *Advances in robot kinematics : analysis and design*, pages 459–468. Springer, 2008.

Doug Stewart. A platform with six degrees of freedom. *Proceedings of the Institution of Mechanical Engineers*, 180(1) :371–386, 1965.

Lining Sun, Qingyong Ding, and Xinyu Liu. Optimal kinematic design of a 2-dof planar parallel robot. In *Robotics, Automation and Mechatronics, 2004 IEEE Conference on*, volume 1, pages 225–230. IEEE, 2004.

Weidong Wang, Litao Zhang, and Junlin Ma. Kinematic calibration of 6-ups surgical parallel robot. In *Complex Medical Engineering (CME), 2013 ICME International Conference on*, pages 369–374. IEEE, 2013.

Mengli Wu, Dawei Zhang, and Xingyu Zhao. Conceptual design and kinematic performance evaluation of a new asymmetrical parallel robot. In *Mechatronics and Automation, 2007. ICMA 2007. International Conference on*, pages 2854–2859. IEEE, 2007.

Y Wu, Z Fu, JN Xu, WX Yan, WH Liu, and YZ Zhao. Kinematic analysis of 5-dof hybrid parallel robot. In *International Conference on Intelligent Robotics and Applications*, pages 153–163. Springer, 2015.

Guilin Yang, Weihai Chen, and I-Ming Chen. A geometrical method for the singularity analysis of 3-RRR planar parallel robots with different actuation schemes. In *Intelligent Robots and Systems, 2002. IEEE/RSJ International Conference on*, volume 3, pages 2055–2060. IEEE, 2002.

Tie Shi Zhao, Yan Wen Li, Jiang Chen, and Jia Chun Wang. A novel four-dof parallel manipulator mechanism and its kinematics. In *Robotics, Automation and Mechatronics, 2006 IEEE Conference on*, pages 1–5. IEEE, 2006.

Matteo Zoppi, Dimiter Zlatanov, and Rezia Molfino. Kinematics analysis of the exechon tripod. In *ASME 2010 International Design Engineering Technical Conferences and Computers and Information in Engineering Conference*, pages 1381–1388. American Society of Mechanical Engineers, 2010.

Chapitre 4

Synthesis and Prototyping of a 6-dof Parallel Robot for the Automatic Performance of Assembly Tasks

4.1 Résumé

Cet article présente les derniers travaux effectués dans le projet. La fabrication d'un prototype a permis de travailler sur des schémas de contrôle. La conception et l'application d'un robot parallèle six degrés de liberté pour l'assemblage de pièces à distance dans un contexte humain-robot. L'architecture du robot est présentée dans un premier temps ainsi que son modèle cinématique. Les matrices Jacobiennes sont calculées et un algorithme de détermination de l'espace de travail est présenté. Les capacités en force du robot sont ensuite analysées. Un prototype est ensuite fabriqué pour l'étude de différents schémas de contrôle. Enfin, une vidéo montre les tests effectués.

4.2 Abstract

This paper presents the development of a 6-dof parallel robot for the performance of assembly tasks in a human-robot collaborative environment. The architecture of the robot is first described and its kinematic model is established. The Jacobian matrices are derived and an algorithm is presented for the determination of its workspace. The force capabilities of the robot are then established. A prototype of the robot is presented and control schemes are developed, including a controller based on a vision system. Finally, a video demonstrating the experimental validation of the robot accompanies this paper.

4.3 Introduction

Assembly tasks are involved in many industrial processes and humans are very effective at such tasks because of their adaptability. However, the repetitive nature of assembly tasks raises some issues in terms of ergonomy and comfort of the human operators. In order to alleviate these drawbacks, the concept of collaborative assembly, which involves humans and robots working together, has emerged (Krüger et al. (2009)). The main objective of collaborative assembly is to reduce the physical and cognitive load on the human operators, while maintaining their engagement in the work. Additionally, introducing robots in the process can improve the productivity and tracability.

Collaborative robotics is used in several industrial settings. For instance, Campeau-Lecours et al. (2017) presents a mechanism which helps for the intuitive lifting and moving of heavy objects. Luecke et al. (2001) presents several control schemes for actuated collaborative lifting mechanisms to improve their behaviour. Labrecque et al. (2017) presents an impedance control scheme with under-actuated degrees of freedom to improve the behaviour and bandwith of a mechanism compared to more conventional admittance methods. Also, several studies deal with the control of a robot working with a human operator in order to make collaborative work more intuitive. For instance, Rahman et al. (2011) presents a control scheme which introduces new parameters linked to the human perception such as the perceived weight and uses these human criteria as optimization factors.

The assistive robot must receive enough information to perform its task properly. Sensors coupled with a proper control strategy are a solution to entitle the robot to its needs to assess its environment. Computer vision is an attractive sensing approach because it is minimally invasive in a context of assembly task. The environment detection is a common vision problem, Liu et al. (2016) exposes a method of segmentation of the environment with 3D cameras to semantically identify the objects in the scene. Adiwahono et al. (2014) proposes a "on network" method to detect obstacles for a mobile robot to make the robot switch its configuration to adapt to its environment. In Mure-Dubois and Hügli (2008), the advantages of mounting a vision system on the mobile parts of a robot rather then on fixed components are discussed. Ahmad and Plapper (2016) introduces vision with a robotic arm to prevent unexpected collisions, with a human for instance.

One of the issues with assembly operations is that some of the tasks must be performed in cluttered or difficult to reach configurations, which may generate ergonomic stressors because human operators must then adopt unfavorable poses. In order to alleviate this problem, it is proposed to use a small six-degree-of-freedom robot mounted on a supporting moveable structure that is controlled — manually or through and interface — by a human operator. The operator brings the robot close to the task to be performed, the robot detects is location with respect to the task using a vision system and then performs the task. This approach

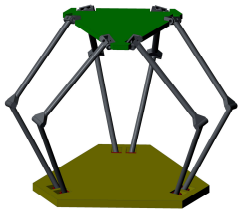

FIGURE 4.1 – Conceptual model of the spatial 6-URS robot.

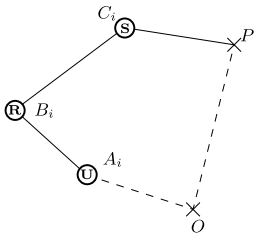

FIGURE 4.2 – Kinematic model of one left of the 6-URS robot.

allows to keep the human operator in favorable — e.g. standing upright — poses, thereby limiting the ergonimic stress. Since the robot is directly in contact with the task, it is desired to ensure that it has proper interaction capabilities. Thefore, the robot should be backdrivable and have a sufficient stiffness and force capabilities to perform assembly tasks.

This paper is structured as follows. In Section 4.4, the architecture and the kinematic model of the 6-dof parallel robot is described, including the solution to the inverse and direct kinematic problems. Section 4.5 presents the derivation of the Jacobian matrices and Section 4.6 provides an algorithm to determine the workspace of the robot, for design purposes. The force capabilities of the robot are then studied in Section 4.7. Section 4.8 describes the prototype that was built as part of this work and Section 4.9 presents the control algorithms that were developed. Finally, Section 4.10 briefly describes the experimental validation and presents an accompanying video and in Section 4.11 some conclusions are drawn.

4.4 Kinematic Architecture of the Robot

The robot is composed of 6 parallel kinematic chains or "legs", each of similar design and actuated by one motor.

The 6-dof robot is represented schematically in Fig.4.1 and the kinematic chain of one leg is presented at Fig.4.2. The i^{th} leg is attached to the fixed base of the robot at point A_i and to the moving platform (end-effector) at point C_i. The leg is composed of two rigid bars linked at point B_i. The architecture of the robot is described as $6 - \underline{U}RS$, namely the joint at A_i is a universal joint with its proximal dof actuated, the joint at B_i is a passive revolute joint and the joint at C_i is a passive spherical joint. It should be noted that the axis of the second (passive) revolute joint of the universal joint located at point A_i is oriented along the line connecting point A_i to point B_i. As a consequence, the position of point B_i is dependent only on the ith actuated joint coordinate and not on the motion of the passive dof of the U joint. Point P is the reference point on the end-effector while point O is the reference point on the base, i.e., the origin of the fixed reference frame. The position vector of point A_i with respect

to the origin of the fixed reference frame is noted $\mathbf{a}_i$. Similarly, the position vectors of points B_i and C_i are noted $\mathbf{b}_i$ and $\mathbf{c}_i$. To control the robot the solution of the inverse kinematic problem (IKP) as well as the Jacobian matrices of the robot (see Waldron et al. (1985) for instance) are needed.

4.4.1 Inverse Kinematic Problem (IKP)

The goal of the IKP is to determine the angles of the revolute joints at the motors for a given position and orientation of the end-effector. The IKP is derived from the constraint equation arising from the length of the distal part of each of the legs. Using the law of cosines on the triangle defined by points A_i, B_i and C_i, one has :

$$\begin{aligned}(\mathbf{c}_i - \mathbf{b}_i)^2 =&(\mathbf{b}_i - \mathbf{a}_i)^2 + (\mathbf{c}_i - \mathbf{a}_i)^2 \\ &- 2(\mathbf{c}_i - \mathbf{a}_i)^T \mathbf{Q}_i (\mathbf{b}_{i0} - \mathbf{a}_i)\end{aligned} \tag{4.1}$$

where :

1. $\mathbf{Q}_i$ is the rotation matrix describing the motion controlled by the ith actuator, i.e., the rotation associated with the first dof of the U joint at point A_i
2. $(\mathbf{c}_i - \mathbf{b}_i)^2 = (\mathbf{c}_i - \mathbf{b}_i)^T(\mathbf{c}_i - \mathbf{b}_i)$ is a constant value, referred to as h_i^2 in what follows. It is the square of the length of the distal link
3. $(\mathbf{b}_i - \mathbf{a}_i)^2 = (\mathbf{b}_i - \mathbf{a}_i)^T(\mathbf{b}_i - \mathbf{a}_i)$ is a constant value, referred to as b_i^2 in what follows. It is the square of the length of the proximal link
4. $\mathbf{b}_{i0}$ is the position vector of point B_i corresponding to the reference orientation of the ith actuator, used to set the 0 for the rotation angle of the actuated dof

In Eq.4.1 and in what follows, one has $i = 1, \ldots, 6$, unless otherwise specified. The rotation matrix $\mathbf{Q}_i$ can be written in terms of the ith joint coordinate θ_i as

$$\begin{aligned}\mathbf{Q}_i =&\mathbf{u}_i\mathbf{u}_i^T + \cos(\theta_i)\left[\mathbf{I}_3 - \mathbf{u}_i\mathbf{u}_i^T\right] \\ &+ \sin(\theta_i)\left[\mathbf{I}_3 \times \mathbf{u}_i\right]\end{aligned} \tag{4.2}$$

where $\mathbf{u}_i$ is a unit vector in the direction of the axis of the ith actuated joint and $\mathbf{I}_3$ stands for the 3×3 identity matrix.

Substituting Eq.4.2 into Eq.4.1, one obtains :

$$K_i + L_i \cos\theta_i + M_i \sin\theta_i = 0 \tag{4.3}$$

where :

$$K_i = h_i^2 - b_i^2 - (\mathbf{c}_i - \mathbf{a}_i)^2 + 2(\mathbf{c}_i - \mathbf{a}_i)^T(\mathbf{u}_i\mathbf{u}_i^T)(\mathbf{b}_{i0} - \mathbf{a}_i) \tag{4.4}$$

$$L_i = 2(\mathbf{c}_i - \mathbf{a}_i)^T \left(\mathbf{I}_3 - \mathbf{u}_i\mathbf{u}_i^T\right)(\mathbf{b}_{i0} - \mathbf{a}_i) \tag{4.5}$$

$$M_i = 2(\mathbf{c}_i - \mathbf{a}_i)^T (\mathbf{I}_3 \times \mathbf{u}_i)(\mathbf{b}_{i0} - \mathbf{a}_i) \tag{4.6}$$

Substituting the following identities in Eq.4.3 :

$$\cos(\theta_i) = \frac{1 - \tan^2(\theta_i/2)}{1 + \tan^2(\theta_i/2)} \tag{4.7}$$

$$\sin(\theta_i) = \frac{2\tan(\theta_i/2)}{1 + \tan^2(\theta_i/2)} \tag{4.8}$$

then yields

$$(K_i - L_i)\tan^2(\theta_i/2) + 2M_i\tan(\theta_i/2) + (K_i + L_i) = 0 \tag{4.9}$$

Therefore, the 2 solutions for the actuated joint coordinates are :

$$\theta_{i1} = 2\arctan\left(\frac{-M_i + \sqrt{M_i^2 + K_i^2 - L_i^2}}{K_i - L_i}\right) \tag{4.10}$$

$$\theta_{i2} = 2\arctan\left(\frac{-M_i - \sqrt{M_i^2 + K_i^2 - L_i^2}}{K_i - L_i}\right) \tag{4.11}$$

This means that the IKP has two solutions for each leg, and hence that for a given configuration (position and orientation) of the end-effector, the IKP for the whole mechanism has $2^6 = 64$ solutions.

4.4.2 Direct Kinematic Problem (DKP)

The IKP gives the joint coordinnates knowing the pose of the end-effector. However, some situations require the opposite, i.e., to obtain the pose of the end-effector knowing the joint coordinnates. This is the problem referred to as direct kinematic problem or DKP.

For convenience, the rotation matrix representing the orientation of the end-effector is partitioned into three column vectors as $\mathbf{Q} = \begin{bmatrix}\mathbf{q}_1 & \mathbf{q}_2 & \mathbf{q}_3\end{bmatrix}$ and a vector that includes 12 parameters is formed with the translations and rotation parameters, of the platform, namely

$$\mathbf{s} = \begin{bmatrix} \mathbf{p} \\ \mathbf{q}_1 \\ \mathbf{q}_2 \\ \mathbf{q}_3 \end{bmatrix}_{12\times 1} . \tag{4.12}$$

Vector $\mathbf{s}$ is a redundant representation of the pose, which introduces robustness in the solution of the direct kinematic problem (DKP). A set of constraint equations must then be written, including the loop closure equations and the constraint equations on the column vectors forming matrix $\mathbf{Q}$. These equations are written as

$$\mathbf{f}(\mathbf{x}) = \begin{bmatrix} (\mathbf{c}_1 - \mathbf{b}_1)^T(\mathbf{c}_1 - \mathbf{b}_1) - l_1^2 \\ (\mathbf{c}_2 - \mathbf{b}_2)^T(\mathbf{c}_2 - \mathbf{b}_2) - l_2^2 \\ (\mathbf{c}_3 - \mathbf{b}_3)^T(\mathbf{c}_3 - \mathbf{b}_3) - l_3^2 \\ (\mathbf{c}_4 - \mathbf{b}_4)^T(\mathbf{c}_4 - \mathbf{b}_4) - l_4^2 \\ (\mathbf{c}_5 - \mathbf{b}_5)^T(\mathbf{c}_5 - \mathbf{b}_5) - l_5^2 \\ (\mathbf{c}_6 - \mathbf{b}_6)^T(\mathbf{c}_6 - \mathbf{b}_6) - l_6^2 \\ \mathbf{q}_1^T\mathbf{q}_2 \\ \mathbf{q}_1^T\mathbf{q}_3 \\ \mathbf{q}_2^T\mathbf{q}_3 \\ \mathbf{q}_1^T\mathbf{q}_1 - 1 \\ \mathbf{q}_2^T\mathbf{q}_2 - 1 \\ \det(Q) - 1 \end{bmatrix}_{12\times 1} = \mathbf{0}. \tag{4.13}$$

The first 6 equations are related to the lengths of links B_iC_i. The following three equations represent the orthogonal nature of the vectors composing a rotation matrix. The next two equations correspond to the fact that the vectors composing the rotation matrix must be unit vectors. Finally, the last equation ensures that the last column of the rotation matrix is a unit vector and that the matrix is a proper orthogonal matrix (not a reflection). The solution of the DKP consists in finding a pose of the platform that satisfies all the equations in Eq.4.13, from given encoder readings. From the encoder readings, vectors $\mathbf{b}_i$ are readily computed. Also, from an estimated pose of the platform, vector $\mathbf{s}$ and position vectors $\mathbf{c}_i$ are readily computed. The limited Taylor expansion of Eq. 4.13 is then written as

$$\mathbf{f}(\mathbf{s}) = \mathbf{f}(\mathbf{s}_0) + d\mathbf{f}/d\mathbf{s}\Delta_{\mathbf{s}} \tag{4.14}$$

Since it is desired to have $\mathbf{f}(\mathbf{s}) = \mathbf{0}$, one has

$$\Delta_{\mathbf{s}} = -(d\mathbf{f}/d\mathbf{s})^{-1}\mathbf{f}(\mathbf{s}_0) \tag{4.15}$$

where $d\mathbf{f}/d\mathbf{s}$ is the (12×12) Jacobian matrix of the system of equations in Eq.4.13, which is readily obtained analytically. Equation4.15 is used iteratively, until a solution to Eq.4.13 is found within a prescribed error threshold. With appropriate conditioning for the equations, the algorithm is fast and robust.

4.5 Jacobian Matrices

The Jacobian matrices provide the velocity relationships between the controlled joint coordinates and the end effector coordinates. To obtain these matrices, equation (1) is first rewritten as

$$h_i^2 = b_i^2 + (c_i - a_i)^T(c_i - a_i) - 2(c_i - a_i)^T(b_i - a_i) \tag{4.16}$$

Differentiating Eq.4.16 with respect to time and noting that $\dot{\mathbf{a}}_i = \mathbf{0}$ then yields

$$(c_i - a_i)^T\dot{c}_i = (c_i - a_i)^T\dot{b}_i + (b_i - a_i)^T\dot{c}_i \tag{4.17}$$

which can be rearranged as

$$(c_i - b_i)^T\dot{c}_i = (c_i - a_i)^T\dot{b}_i. \tag{4.18}$$

Furthermore, one has

$$\dot{\mathbf{b}}_i = \theta_i\mathbf{u}_i \times (\mathbf{b}_i - \mathbf{a}_i) \tag{4.19}$$

and,

$$\dot{\mathbf{c}}_i = \dot{\mathbf{p}} + \boldsymbol{\omega} \times (\mathbf{c}_i - \mathbf{p}) \tag{4.20}$$

where $\dot{\mathbf{p}}$ is the velocity of vector point P of the end effector and $\boldsymbol{\omega}$ is the angular velocity of the end effector.

Substituting Eq.4.19 and Equation 4.20 into Eq.4.18 then leads to

$$\begin{aligned}((\mathbf{b}_i - \mathbf{a}_i) \times (\mathbf{c}_i - \mathbf{a}_i))^T\mathbf{u}_i\dot{\theta}_i =&(\mathbf{c}_i - \mathbf{b}_i)^T\mathbf{t} \\ &+ ((\mathbf{c}_i - \mathbf{p}) \times (\mathbf{c}_i - \mathbf{b}_i))^T\boldsymbol{\omega}\end{aligned} \tag{4.21}$$

This equation can be written in matrix form as :

$$\mathbf{K}\dot{\boldsymbol{\theta}} = \mathbf{J}\dot{\mathbf{x}} \tag{4.22}$$

with $\dot{\boldsymbol{\theta}} = \begin{bmatrix} \dot{\theta}_1 & \dot{\theta}_2 & \dot{\theta}_3 & \dot{\theta}_4 & \dot{\theta}_5 & \dot{\theta}_6 \end{bmatrix}^T$ the joint velocity vector and $\dot{\mathbf{x}} = \begin{bmatrix} \boldsymbol{\omega} & \dot{\mathbf{p}} \end{bmatrix}^T$ the generalised end-effector velocity, and where the Jacobian matrices are written as

$$\mathbf{K} = diag(((\mathbf{b}_i - \mathbf{a}_i) \times (\mathbf{c}_i - \mathbf{a}_i))^T \mathbf{u_i}, i = 1..6) \tag{4.23}$$

$$\mathbf{J} = \begin{bmatrix} ((\mathbf{c}_1 - \mathbf{p}) \times (\mathbf{c}_1 - \mathbf{b}_1))^T & (\mathbf{c}_1 - \mathbf{b}_1)^T \\ ((\mathbf{c}_2 - \mathbf{p}) \times (\mathbf{c}_2 - \mathbf{b}_2))^T & (\mathbf{c}_2 - \mathbf{b}_2)^T \\ ((\mathbf{c}_2 - \mathbf{p}) \times (\mathbf{c}_2 - \mathbf{b}_2))^T & (\mathbf{c}_2 - \mathbf{b}_2)^T \\ ((\mathbf{c}_2 - \mathbf{p}) \times (\mathbf{c}_2 - \mathbf{b}_2))^T & (\mathbf{c}_2 - \mathbf{b}_2)^T \\ ((\mathbf{c}_2 - \mathbf{p}) \times (\mathbf{c}_2 - \mathbf{b}_2))^T & (\mathbf{c}_2 - \mathbf{b}_2)^T \\ ((\mathbf{c}_2 - \mathbf{p}) \times (\mathbf{c}_2 - \mathbf{b}_2))^T & (\mathbf{c}_2 - \mathbf{b}_2)^T \end{bmatrix} \tag{4.24}$$

4.6 Workspace

In this application, the robot is brought close to the task. Hence, the target workspace is a sphere with a diameter of approximately 12 centimetres. To ensure that this goal is reached, design tools were developed to assess and adjust the capabilities of the robot. The static workspace of the robot is considered, meaning that singularities cannot be overcome with momentum and that the workspace must be free from singularities. This choice is made to avoid specific control limitations.

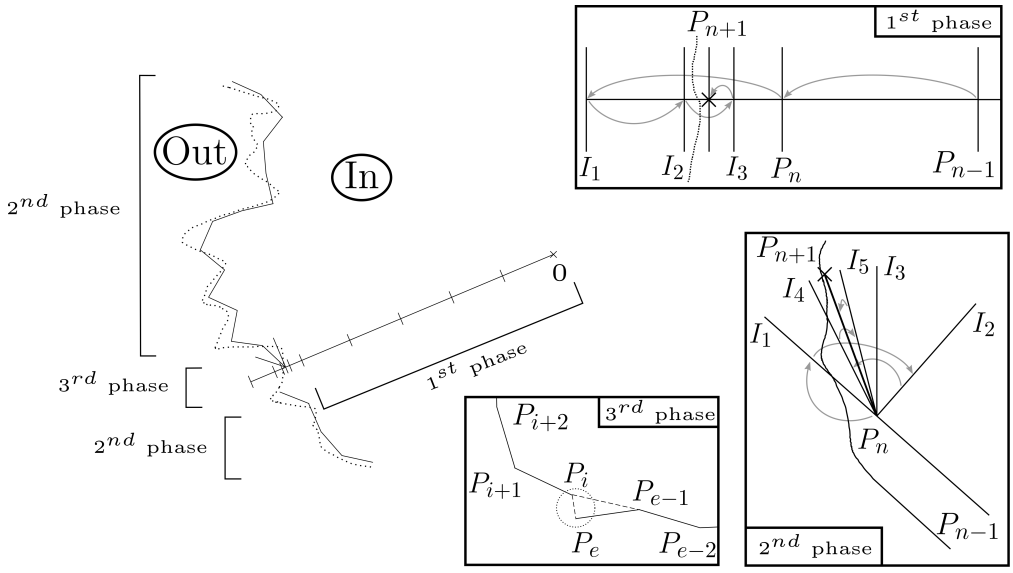

FIGURE 4.3 – Model representation for the geometric workspace detection algorithm.

To estimate the workspace of the robot, a numerical method based on the geometric equations derived above is used. Figure4.3 illustrates the principle of the algorithm. The workspace is defined here as the set of possible poses (position and orientation) of the end-effector. These

poses correspond to all the potential solutions of the IKP and thus all the solutions of Eq.4.9. The IKP gives a solution when its discriminant Δ is greater than or equal to zero, thus

$$\Delta_i = 4(M_i^2 - K_i^2 + L_i^2) \geq 0. \tag{4.25}$$

This condition must be verified for all 6 legs of the robot for a given pose to be a potential configuration. If this condition is met, the robot is in a "In" state, refering to Fig.4.3, otherwise it is in a "Out" state. A numerical approach has been selected because it allows one to include as many constraints as needed, in addition to the limitations given by Eq.4.25, such as joint limits, mechanical interferences and others. The goal of the algorithm is to find the boundaries of the workspace for the end-effector reference point. The robot has 6 degrees of freedom, and hence its workspace is embedded in a six-dimensional space, which cannot be simply visualized. Moreover, computing a six-dimensional workspace can be computationally intensive, which is not ideal in a context of design, where this operation must be completed repetitively to adjust the design parameters. Therefore, the orientation of the platform is prescribed and then the algorithm to generate the position workspace is used. The result is a closed surface within which it is required to evaluate the performance of the robot.

The three-dimensional space is sliced into a number of layers according to one of the directions, and each layer is treated separately. The algorithm works like a search algorithm in a planar space : it operates in 3 phases. First, a reference position of the robot is chosen for the prescribed orientation. This position must belong to the workspace of the robot, and is usually easily determined. In the first phase, the robot follows a line from the initial point by increments of distance in a chosen arbitrary direction. At each new location, the algorithm checks if the condition of Eq.4.25 is still valid for each leg. The increment distance must be chosen small enough so that the robot does not immediately step over the workspace boundary but large enough so that this first phase does not take too long. After the first "Out" configuration is encountered, it means that the workspace limit in this direction is between the previous position and the current one. The algorithm then searches more precisely the location of this boundary using a bisection method. This is shown in the top right corner of Fig.4.3. P_n is the last point before an "Out" configuration is reached and I_1 the first "Out" point. The dashed line represents the exact unknown location of the boundary. The first step of the bisection algorithm is to select a new point in the same direction, I_2, which is the mid-point between P_n and I_1. Then, point I_2 is checked to determine whether it is "In" or "Out". If I_2 is "In", then the boundary is between I_1 and I_2, whereas if I_2 is "Out" (like in Fig.4.3), the boundary is between P_n and I_2. Then, the process is repeated with the new points enclosing the boundary. The result of the bisection algorithm is a new valid point P_{n+1}.

The first phase described above is first used to determine the limits of the workspace in the "z" direction of the base frame. Then, a chosen number of positions are set between z_{min} and z_{max}

as a set of layers to form the workspace. Then, each layer is treated as a two-dimensional case and the boundaries are determined in the (x, y) plane. The algorithm repeats the first phase in an arbitrary direction in the plane. It gives an estimate of one position on the boundary. The first phase of the algorithm could be repeated from the initial point with different directions but this approach has proven not sufficiently robust. The method used instead is the second phase. During the second phase, the algorithm starts at the last valid point found, referenced as P_n. Then it will advance in the direction defined by P_n and P_{n-1} by another set distance. Like in the first phase, the process is repeated until an "Out" point is found. Then, an angular approach is chosen to find the next boundary point. It enables the algorithm to search in various unset directions instead of only one and the accuracy is much more consistent because of the set advance length. When an "out of bound" is found, the algorithm searches clockwise the closest point that belongs to the workspace. In Fig.4.3, I_1 is the first "Out" point, a bisection is then performed on the angle. The clockwise direction is preferred because one must be chosen and it does not have any noticed effect on the performance, it however defines the direction in which the boundary will be detected. In the example shown in Fig.4.3, the boundary is discovered clockwise, which is why the new points are constructed upwards instead of downwards. The bisection algorithm works in a similar way as in phase 1 : I_2 is created and, because it is "In", the boundary is expected to be between I_1 and I_2. I_3 is still "In", so I_4 is between I_3 and I_1 and so on. Eventually the threshold is reached and P_{n+1} is defined. The increment threshold is an angle in this case and it is still required for the selected point to be a "In" point.

After many trials, the successive iterations of the second phase eventually find the boundary of the workspace rather accurately. However, it is necessary to find a method to finish the search procedure. Therefore, the third phase is introduced. The schematic shown in Fig.4.3 only shows when the third phase activates, but in fact it makes a check with each new point that the second phase produces. The third phase consists in checking the distance between the new boundary point found and the initial point when the second phase first occurred. If this distance is considered small enough referring to another threshold, the algorithm stops. This is shown in the bottom right corner of Fig.4.3. P_i is the first point processed with the second phase. P_{i+1}, P_{i+2}, ... are the next points in the process. P_e is the first point that meets the "close enough" condition. The dashed lines and the dashed circle represent the fact the point preceding point P_e, referred to as P_{e-1}, is too far for the closure condition to be satisfied but P_e is close enough. It is worth noticing that some care must be taken using this method. Indeed, as usual, some specific cases must be taken care of to ensure that the algorithm does not fall in a deficient state. For example, if the proximity distance threshold of phase 3 is larger than the advance distance of phase 2, then the phase 3 condition will be met immediately after the first iteration of phase 2 despite being far from really finishing and the result will be incorrect. To avoid this situation, the threshold distance of phase 3 should be set significantly smaller than the advance distance of phase 2, at least 3 times shorter. However,

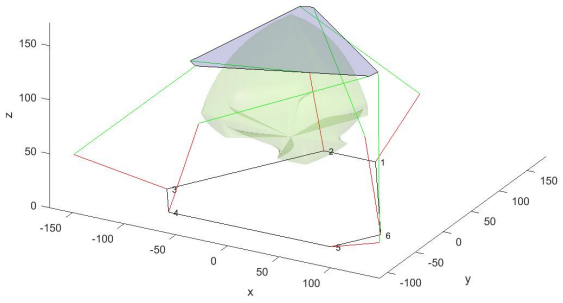

FIGURE 4.4 – Representation of the geometric workspace of the robot in a 80° Torsion orientation from its reference orientation.

because a small distance is preferable for phase 2 in order to obtain a more accurate depiction of the boundaries and a short distance for phase 3 can cause the right matching timing to be missed, other solutions can be preferable depending on the case applied. Another solution is to take care of the first iterations of phase 2. Because it is intended for phase 2 to make a reasonable number of iterations, ignoring the check condition of phase 3 for some iterations at the start can be an appropriate solution. This algorithm is obviously not flawless and the exception cases addressed here do not cover all possible deficiencies. However, it proved to produce satisfying results. Despite the robustness flaws discussed, its strengths should not be ignored. It is still solving a quite complex mathematical problem in a reasonable computation time. The final part of the procedure is to produce the surface boundary in the 3d space. Once all layers are computed, the algorithm has different sets of points, one for each layer, with varying number of points, that must be matched to produce the surface. Linear interpolation is then used to set all layers to the same number of points which correspond to the largest number of points found in a layer. The same starting direction for phase 1 must be chosen in each layer, so that the indices are correct matches for the plotting.

The final result is shown in Fig.4.4. The robot's limbs are shown in the initial configuration chosen for the algorithm, which is a 80° Torsion orientation from its reference orientation. The estimated workspace is the surface in the middle and corresponds to all reachable positions for the reference point on the end-effector.

However, it is known that the workspace of a robot is not only limited by the reachable space. Singular configurations (also referred to as singularities, see Cleary and Arai (1991); Liu et al. (2003); Huang et al. (2003)for general insights on sigularities for parallel manipulators or Kong and Gosselin (2002); Ebrahimi et al. (2007); Gallardo-Alvarado et al. (2006) for more specific examples) are a limiting working condition for robots, especially parallel robots. These configurations are configurations in which where the behaviour of the robot can change unexpectedly. For instance, in singular configurations, the force output possible in some di-

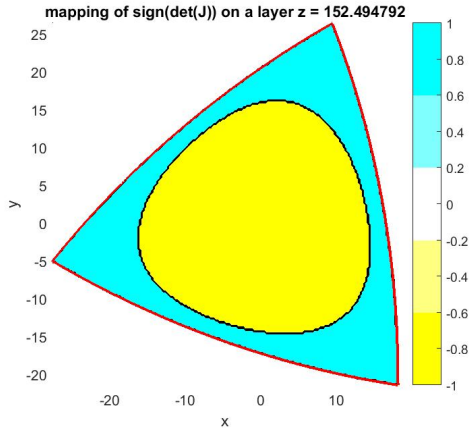

FIGURE 4.5 – Singularity locus detection in a section of the workspace of the robot, the robot is in a 80° Torsion orientation from its reference orientation.

rection drops considerably. Parallel robots are known to have singular configurations that can be located within the boundaries of their reachable workspace. Therefore, a separate analysis must be conducted in order to identify the singular configurations. However, the workspace analysis greatly reduces the area to study and consequently improves speed and accuracy of the singularity analysis. In each of the layers considered above, within the boundaries defined above, the determinant of matrix **J** is computed. A singular configuration is reached when the determinant reaches zero (see Leu and Pai (1992); Ben-Horin and Shoham (2009); Zhao (2013); Kim et al. (1999) for analysis of the roots of the determinant to study singular configurations). The numerical method to search for zeros is to check the sign of the determinant.

Figure4.5 shows the computation of the sign of the determinant. For each point representing a location in the workspace, a positive sign is indicated by a yellow dot and a negative sign by a blue one. The black boundary between yellow and blue represents the singularity locus. In this example, only the yellow zone could be exploited. It is computed in each layer to give an insight on the spatial singularity locus. Hence, the actual workspace may be considerably reduced by singularities, as illustrated in Fig. 4.5. In a context of design, the goal is to find design parameters that will yield the largest possible useful workspace with simple shapes, in order for the robot to be easy to exploit in practice. The parameters of the robot, especially the location of points A_i and direction of motor axes $\mathbf{u}_i$ greatly affect the results. Several iterations on the design were completed in order to obtain the best possible results.

4.7 Force Capabilities

In this section, a mathematical model is developed in order to determine the force capabilities of the robot. This analysis is important in order to assess the tasks that can be performed

by the manipulator. The model used to estimate the forces is the static model, obtained from the principle of virtual power. We can write that the input and output virtual powers must be equal, namely

$$P_{in} = P_{out} \tag{4.26}$$

$$\dot{\boldsymbol{\theta}}^T \mathbf{c} = \dot{\mathbf{x}}^T \mathbf{f} \tag{4.27}$$

where $\dot{\boldsymbol{\theta}}$ is the vector of actuated joint velocities, $\mathbf{c}$ is the vector of joint torques, $\dot{\mathbf{x}}$ is the vector of Cartesian velocities and $\mathbf{f}$ is the vector of Cartesian forces and torques. Substituting Eq.4.22 into Eq.4.27, one then has

$$\dot{\boldsymbol{\theta}}^T \mathbf{c} = \left[\mathbf{J}^{-1}\mathbf{K}\dot{\boldsymbol{\theta}}\right]^T \mathbf{f} \tag{4.28}$$

which yields

$$\dot{\boldsymbol{\theta}}^T \mathbf{c} = \dot{\boldsymbol{\theta}}^T \mathbf{K}^T \mathbf{J}^{-T} \mathbf{f}. \tag{4.29}$$

For this relation to remain true for any value of $\dot{\boldsymbol{\theta}}$, the following relation must be satisfied :

$$\mathbf{c} = \mathbf{K}^T \mathbf{J}^{-T} \mathbf{f} \tag{4.30}$$

This is a simplified expression of the generalized formula shown in Salisbury and Craig (1982). From this relation, for a known load applied on the effector, we can estimate the required actuator torques. For instance, the estimated weight of the mobile parts is 200g, overestimated at 300g. It leads to a 3N force applied at the effector. The direction of the gravity is set in different possibilities.

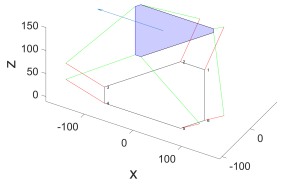

FIGURE 4.6 – Model of the robot used for the force analysis. The arrow at the top indicates the direction of the force.

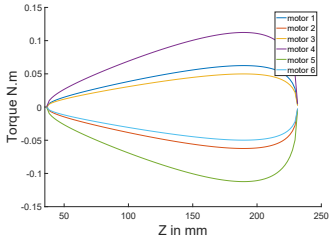

FIGURE 4.7 – Torques required at the motors with a 3N force applied at the effector in the $-X$ direction.

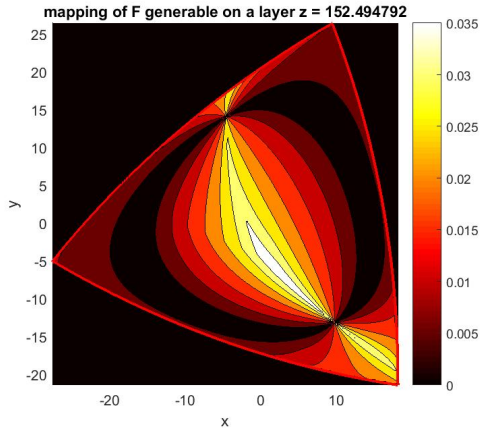

FIGURE 4.8 – Force ratio potency of the robot in the X direction in a section of its workspace, the robot is in a 80° Torsion orientation from its reference orientation.

Figure4.7 shows a computation of the required torque along a displacement on the vertical axis. Figure4.7 represents the robot in one of the configuration and the arrow at the top on the end-effector shows the direction of the force applied. It shows that the worst configuration requires a little more than 0.1Nm. No reduction stage was introduced here at the actuated joints in order to keep the transmission easily backdrivable. With such an arrangement, the mechanism can allow compliant movements , which is desirable for interactions with the task. Furthermore, end force impacts on the motor current is not scaled down by the reduction ratio and could be measured with enough accuracy to be included in the control scheme.

Figure4.8 shows the same section of the workspace as Fig.4.5 but presents the force transmission ratio in the "X" direction. It can be observed that the force transmission ratio is close to zero in the areas close to the singular configurations.

The above design tools were used to tune the geometric parameters of the robot. Among others, the force ratio was used to ensure the capabilities of the robot. The method of computation is as follows. First, a force/moment direction is chosen. This is the direction along which the force ration of the robot is to be computed. It is comprised in vector $\mathbf{f}$, for instance, a force in the "Y" direction corresponds to $\mathbf{f} = \begin{bmatrix} 0 & 1 & 0 & 0 & 0 & 0 \end{bmatrix}^T$. The magnitude of $\mathbf{f}$ is not important in this step. Then, the actuator torques are computed using Eq.4.30. The result is then normalized, i.e., the result is adjusted so that when multiplied by the maximum available torque, the maximum possible force in the chosen direction is obtained. Force ratios are defined as :

$$\frac{F_{output}}{F_{input}} = R \tag{4.31}$$

However, there are six inputs instead of one for one output. Therefore, for a set of intended

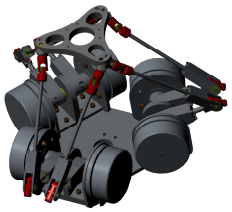

FIGURE 4.9 – CAD model of the final design of the 6-URS robot.

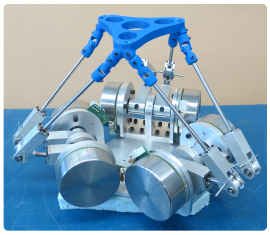

FIGURE 4.10 – Photography of the manufactured 6-URS robot.

similar actuators with the same maximum available torque, the above results are multiplied by a coefficient so that the maximum absolute value of torque is 1 (in the wanted unit, Nm for instance). If actuators with different force capabilities are intended, coefficients should be applied accordingly. Then, Eq.4.30 is applied in the reverse direction :

$$\mathbf{f} = \mathbf{J}^T \mathbf{K}^{-T} \mathbf{c} \tag{4.32}$$

The result gives a coefficient when multiplied by the maximum force of the chosen type of actuator (maximum continuous torque for a motor / maximum peak torque depending the intended process of use) gives the potential maximum force that the robot can produce in this direction. Because the Jacobian matrices change with the configuration, the result changes with the location. That is why this method is computed for all the configurations in the previously bounded workspace. An example of result is presented through a contour plot in Fig.4.8 for a 80° twist orientation. Overall, we estimate the real workspace as the reachable space not crossed by singularities in which sufficient force capabilities can be deployed. Because of the 6 DOFs, the impact of the design parameters on the properties of the parallel architecture can be difficult to predict. However, the above analysis allowed an iterative design exercise that led to an architecture for which the workspace and force capabilities where judged sufficient. Using the tilt and torsion convention (proposed originally in Bonev and Ryu (1999) as a novel three-angle orientation representation), we estimate that the following orientations can be reached in most positions :

Angle	Value
Tilt	±30 degrees
Torsion	±60 degrees

4.8 Prototyping

The CAD model of the robot is shown in Fig.4.9 and a photo of the manufactured prototype is shown in Fig.4.10. The dimension of the parts were chosen based on beam theory and finite

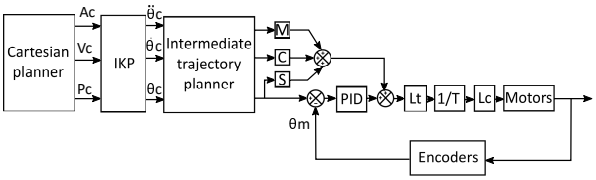

FIGURE 4.11 – Position control scheme.

element computations. Bearings, bushings, retaining rings and screws are used with care to produce an easy to build mechanism with low friction motions. It was decided to not have gears to get a backdriveable mechanism for further tests, therefore, the motor needed to be able to produce high torques by themselves with a relatively low need for high velocities. The selected motors are Maxons EC90 Flat, brushless, 260W with 4096 count per turns encoders, two channels. They can reach 1 Nm constant torque output.

4.9 Control Schemes

4.9.1 Position Control

Position control is a standard first step in the process of controlling a robot. It validates the mathematical model and the tools developed for it are useful for further models.

The position control scheme is shown in Fig.4.11. It works as follows. First, a pose must be input as the desired pose of the robot, a pose being the location of the reference point as well as the orientation of the end-effector. This can be extended as a trajectory, meaning a set of poses. That is why the input of the control scheme is referred to as a planner. In the case of a trajectory, acceleration and velocity information should be provided as well to include the complete kinematic behaviour in the scheme. The Cartesian pose or trajectory is converted to joint coordinates using the solution of the IKP (Eqs.4.10 and 4.11 determined in Subsection 4.4.1). Then, a closed control loop is applied using the data collected by the encoders. The angle difference between the desired position of the actuated joints and the measured one is fed to the PID regulator. The output is considered as a torque, to which an estimated required torque based on the desired trajectory is added. Then, a torque limiter L_t limits the maximum torque sent. Afterwards, this torque value is converted to a current value with the motor current to torque ratio T, using its inverse in this case. Then, another limiter is added for the current L_c. Two limiters are redundant but they cater to different limiting reasons and are therefore useful as a simple means of guaranteeing basic motor protection. The vector of joint velocities $\dot{\boldsymbol{\theta}}$ is obtained using Eq.4.22, namely

$$\dot{\boldsymbol{\theta}} = \mathbf{K}^{-1}\mathbf{J}\dot{\mathbf{x}} \tag{4.33}$$

with $\mathbf{K}$ and $\mathbf{J}$ the matrices developed in Eqs.4.23 and 4.24. The joint accelerations $\ddot{\boldsymbol{\theta}}$ are

obtained by differentiating Eq.4.33 with respect to time, which yields

$$\ddot{\boldsymbol{\theta}} = \mathbf{K}^{-1}(\mathbf{J}\ddot{\mathbf{x}} + \dot{\mathbf{J}}\dot{\mathbf{x}} - \dot{\mathbf{K}}\dot{\boldsymbol{\theta}}) \tag{4.34}$$

with the following expressions for $\dot{\mathbf{J}}$ and $\dot{\mathbf{K}}$,

$$\dot{\mathbf{J}} = \begin{bmatrix} \Big((\dot{\mathbf{c}}_1 - \dot{\mathbf{p}}) \times (\mathbf{c}_1 - \mathbf{b}_1) + \mathbf{c}_1 - \mathbf{p}) \times (\dot{\mathbf{c}}_1 - \dot{\mathbf{b}}_1)\Big)^T & (\dot{\mathbf{c}}_1 - \dot{\mathbf{b}}_1)^T \\ \Big((\dot{\mathbf{c}}_2 - \dot{\mathbf{p}}) \times (\mathbf{c}_2 - \mathbf{b}_2) + \mathbf{c}_2 - \mathbf{p}) \times (\dot{\mathbf{c}}_2 - \dot{\mathbf{b}}_2)\Big)^T & (\dot{\mathbf{c}}_2 - \dot{\mathbf{b}}_2)^T \\ \Big((\dot{\mathbf{c}}_3 - \dot{\mathbf{p}}) \times (\mathbf{c}_3 - \mathbf{b}_3) + \mathbf{c}_3 - \mathbf{p}) \times (\dot{\mathbf{c}}_3 - \dot{\mathbf{b}}_3)\Big)^T & (\dot{\mathbf{c}}_3 - \dot{\mathbf{b}}_3)^T \\ \Big((\dot{\mathbf{c}}_4 - \dot{\mathbf{p}}) \times (\mathbf{c}_4 - \mathbf{b}_4) + \mathbf{c}_4 - \mathbf{p}) \times (\dot{\mathbf{c}}_4 - \dot{\mathbf{b}}_4)\Big)^T & (\dot{\mathbf{c}}_4 - \dot{\mathbf{b}}_4)^T \\ \Big((\dot{\mathbf{c}}_5 - \dot{\mathbf{p}}) \times (\mathbf{c}_5 - \mathbf{b}_5) + \mathbf{c}_5 - \mathbf{p}) \times (\dot{\mathbf{c}}_5 - \dot{\mathbf{b}}_5)\Big)^T & (\dot{\mathbf{c}}_5 - \dot{\mathbf{b}}_5)^T \\ \Big((\dot{\mathbf{c}}_6 - \dot{\mathbf{p}}) \times (\mathbf{c}_6 - \mathbf{b}_6) + \mathbf{c}_6 - \mathbf{p}) \times (\dot{\mathbf{c}}_6 - \dot{\mathbf{b}}_6)\Big)^T & (\dot{\mathbf{c}}_6 - \dot{\mathbf{b}}_6)^T \end{bmatrix} \tag{4.35}$$

and

$$\dot{\mathbf{K}} = diag\left(\left(\dot{\mathbf{b}}_i \times (\mathbf{c}_i - \mathbf{a}_i) + (\mathbf{b}_i - \mathbf{a}_i) \times \dot{\mathbf{c}}_i\right)^T \mathbf{u}_i, i = 1..6\right) \tag{4.36}$$

where the expressions for $\dot{b}_i$ and $\dot{c}_i$ are given in Eq.4.19 and in Eq.4.20.

The estimation of the motor positions, velocities and accelerations enables to estimate the required torque during the trajectories with the following expression :

$$\mathbf{t}_q = \mathbf{M}\ddot{\boldsymbol{\theta}} + \mathbf{C}\dot{\boldsymbol{\theta}} + \mathbf{S}\boldsymbol{\theta}. \tag{4.37}$$

with $\mathbf{M}$ the inertia matrix of the mobile parts, $\mathbf{C}$ the damping matrix and $\mathbf{S}$ the stiffness matrix. The system does not include viscous or elastic components and the material properties that could introduce such variables were considered negligible. The inertia matrix includes the inertia reflected for each motor, the parts being mobile, these values change while the robot is moving. An average inertia was estimated from the design software. Albeit less accurate than a complete analysis, it was still an interesting addition to the control while not requiring much time to implement. This predictive control allows the regulator to be less solicited and more efficient thanks to a more accurate understanding of the physics of the mechanism.

The PID scheme is shown in Fig.4.12. It is a classical parallel PID regulator architecture, the parameters were determined from an estimation of the average inertia seen by the motors from the CAD model.

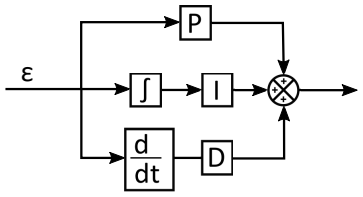

FIGURE 4.12 – Parallel PID model used in the control scheme.

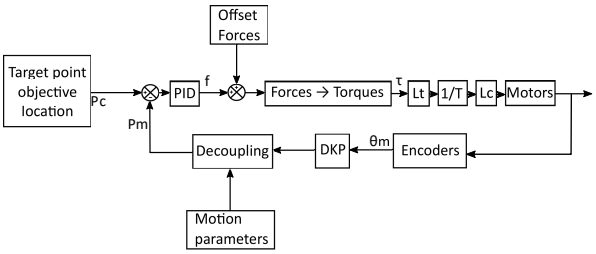

FIGURE 4.13 – Hybrid force/position control scheme.

4.9.2 Hybrid Control

The position control is effective to move the robot in planned trajectories with a complete control over the motion of the robot. However, in a collaborative environment, some uncertainties are introduced by the actions of humans or by contacts with the environment and this position control is no longer adapted. In order to address these issues, a hybrid position/force control scheme was developed.

This control scheme is shown in Fig.4.13. As mentioned above, the robot is backdrivable. This property can be used to enhance the collaborative behaviour of the robot. Indeed, the interaction between the environment (operator, external objects) and the end-effector of the robot can be used to produce behaviours that mimic the action of passive spring based RCC mechanisms (see Whitney (1982) as reference) with the benefit of being programmable and supporting additional control features such as vision detection. This approach is similar to admittance control (discussed in Keemink et al. (2018) for instance) but no force sensors are involved. The "force" is determined by how much the end part is moved from the desired controlled position, i.e., impedance control is implemented. In other words, this deviation is assimilated to a force similar to how a spring would behave. For this reason, it is important to determine the pose of the end-effector, which is obtained through the solution of the direct kinematic problem (determined in Subsection 4.4.2), from the encoder readings.

The objective of this control scheme is to emulate the behavior of a RCC mechanism. It means that the robot must be able to produce an elastic behavior near a chosen point for the six degrees of freedom. The advantages of the emulation of the RCC are that the location of the

target point can be changed arbitrarily and the elastic stiffness can be changed independently with any value. The control scheme is shown in Fig.4.13. The location of the target Cartesian configuration is chosen in the Cartesian block, specified in the "Motion parameters" block. The real location of the robot is measured with the encoders and the computation of the solution of the direct kinematic problem. The position differences must generate proportional forces multiplied by the elastic coefficient ; for the PID, only a P regulator is used if the desired behavior is purely elastic. However, some derivative coefficient can be added to damp the oscillations. Then, these Cartesian forces are converted to motor torques with the forces to torques relation (special case of Salisbury and Craig (1982)), one has :

$$\tau = \mathbf{K}^T \mathbf{J}^{-T} \begin{bmatrix} \mathbf{f}_t \\ \mathbf{f}_r \end{bmatrix} \tag{4.38}$$

where f_t is the vector of translational Cartesian forces and f_r the vector of Cartesian torques. These efforts are chosen to have proportional behaviour with the deviation between the targeted location and the measured one :

$$\mathbf{f}_t = \mathbf{K}_p \Delta t \tag{4.39}$$

$$\mathbf{f}_r = \mathbf{K}_\theta \Delta \theta \tag{4.40}$$

with

$$\mathbf{K}_t = \begin{bmatrix} k_{tx} & 0 & 0 \\ 0 & k_{ty} & 0 \\ 0 & 0 & k_{tz} \end{bmatrix} \tag{4.41}$$

$$\mathbf{K}_\theta = \begin{bmatrix} k_{\theta x} & 0 & 0 \\ 0 & k_{\theta y} & 0 \\ 0 & 0 & k_{\theta z} \end{bmatrix} \tag{4.42}$$

with "k_{xx}" the chosen elastic coefficient.

One important aspect is the handling of the rotations. Preferably, the rotations should be decoupled from one another to get a proper consistent behaviour, which is not compatible with Euler angles where the angles are multiplied to get the orientation matrix. To get decoupled rotations around the Cartesian axes, quaternions are used instead. The transformation formula from the orientation matrix to quaternions and reversed are presented in Zhang (1997). Quaternions are useful to produce a continuous model for the representation of orientation space, as discussed in Evans (1977), which is important for the convergence of the algorithm. The quaternions yield three independent angles around the axes of the reference frame, and the deviation between these angles and the targeted angles produce the torques to reproduce the behaviour of torsion springs around the axes.

Another aspect explored was the introduction of damping in the control scheme. Passive RCC mechanisms do not have damping elements but it was easy to introduce them here by adding another force based on the derivative of Δp and $\Delta\theta$ with other coefficient matrices $\mathbf{D}_t$ and $\mathbf{D}_\theta$. Eqs.4.39 and 4.40 become

$$\mathbf{f}_t = \mathbf{K}_t \Delta t + \mathbf{D}_t \dot{\Delta} t \tag{4.43}$$

$$\mathbf{f}_r = \mathbf{K}_\theta \Delta\theta + \mathbf{D}_\theta \dot{\Delta}\theta \tag{4.44}$$

with

$$\mathbf{D}_t = \begin{bmatrix} d_{tx} & 0 & 0 \\ 0 & d_{ty} & 0 \\ 0 & 0 & d_{tz} \end{bmatrix} \tag{4.45}$$

$$\mathbf{D}_\theta = \begin{bmatrix} d_{\theta x} & 0 & 0 \\ 0 & d_{\theta y} & 0 \\ 0 & 0 & d_{\theta z} \end{bmatrix} \tag{4.46}$$

with "d_{xx}" the chosen damping coefficient. The introduction of damping significantly reduces the oscillations produced by high stiffness coefficients but lessens the similarities with the behaviour of a conventional RCC.

The hybrid control scheme simulates the behaviour of a RCC mechanism, with the adding benefits of changeable coefficients for the stiffness. The location of the centre of rotation can also be changed. This is a very interesting feature because a centre of rotation far from the contact point is difficult to achieve with passive mechanism. Moreover, the centre of rotation of the original RCC design is not fixed, only allowing small motions to keep a consistent behaviour, which is not a problem for the control scheme. However, the robot used in this case is not suited to really far virtual centre of rotation because of singularities, different designs should be explored to benefit from this aspect of the control scheme.

4.9.3 Vision Control

The third control scheme explored in this work makes use of a camera and computer vision algorithms to guide the motion of the robot. In the intended work scenario, the human operator brings the robot close to the task to be performed and then the robot performs the task using computer vision to guide the motion of the end-effector.

Some state-of-the-art methods were explored to detect the pose of the parts like SIFT (see Lowe (2004) for the original reference) and ORB (see Rublee et al. (2011) for the original reference) feature detection. Although these tools have proven very effective for detection

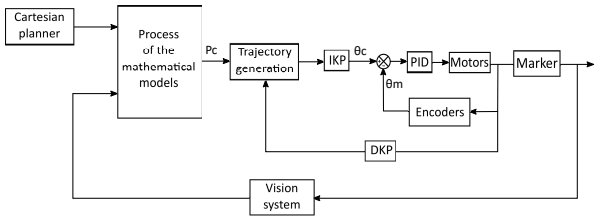

FIGURE 4.14 – Vision based control scheme.

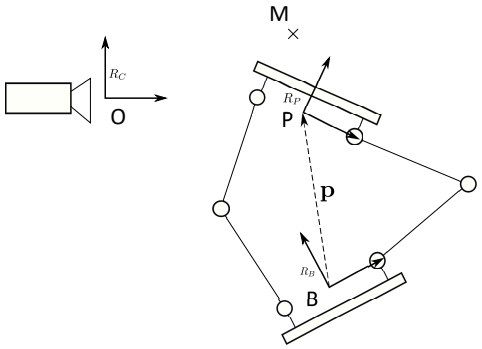

FIGURE 4.15 – Geometric model to solve the relative positions and orientations required for the vision based control scheme.

problems in general, ARUCO marker detection (see Rekimoto (1998)) was selected here due to its robustness and ease of implementation despite requiring hardware constraints. Indeed, in an industrial environment, robustness is of paramount importance. Several options exist on the placement of the ARUCO markers and the camera. For example, the camera could be mounted on the end-effector of the robot and markers could be placed in known locations in the environment. In this work, we chose to place the camera in a set known location in the environment and one marker is placed on the end-effector of the robot. The detection of the marker is handled by a python script that uses the ARUCO library. The script creates packages of the location and orientation data and sends them to a port in the target node computer used to process the Simulink Realtime control scheme of the robot. A "UDP retrieve" block in simulink collects the data package in the port, unpacks it and uses it for the control. The marker detection and the control process run on two different machines and are not synchronized. Therefore, the processing speed of one does not influence the processing speed of the other. One main challenge is to solve the mathematical problem giving the desired inputs for the command of the robot. The control scheme is shown in Fig.4.14. The Cartesian planner processes the desired poses of the robot, the vision system measures the pose of the marker in the camera frame. Because the marker‘s location on the end-effector is known, the measurement of the vision system gives indirectly the pose of the end-effector.

The solution of the mathematical model requires the knowledge of the pose of the robot relative

to the base because the pose of the base (which is mobile) must be determined. Therefore, instead of using another sensor, the pose of the robot is determined using the solution of direct kinematic problem presented above, making use of the encoders. This information is taken from the output of the trajectory generation block. Indeed, in order to smoothen the movement of the robot, several points are generated between the current pose of the robot and the desired pose. Figure4.15 illustrates the geometric modelling of the robot and camera. Three reference frames are used, namely : one attached to the camera referred to as R_C, one attached to the base referred to as R_B and one attached to the effector/platform referred to as R_P. The main points of interest are M_m, the current location of the marker on the platform, and M_o, the targeted location for the marker, which corresponds to the desired pose of the robot. We introduce $\mathbf{B}_{i/j}$ the rotation matrix from frame i to frame j. For instance, $\mathbf{B}_{B/P}$ is the rotation matrix from R_B to R_P. We have the following result :

$$[\mathbf{m}_o]_{R_B} = [\mathbf{o}]_{R_B} + \mathbf{B}_{C/B}[\mathbf{m}_o]_{R_C} \tag{4.47}$$

$$\mathbf{B}_{C/B} = \mathbf{B}_{C/P}\mathbf{B}_{P/B} \tag{4.48}$$

where $\mathbf{m}_o$ and $\mathbf{o}$ are respectively the position vectors of points M_o and O and where the subscripts of the brackets indicate in which frame the vectors are expressed. The kinematic closed loop then leads to

$$[\mathbf{o}]_{R_B} = [\mathbf{p}]_{R_B} + \mathbf{B}_{P/B}[\mathbf{m}_m]_{R_P} - \mathbf{B}_{C/B}[\mathbf{m}_m]_{R_C} \tag{4.49}$$

where $\mathbf{p}$ and $\mathbf{m}_m$ are the position vectors of points P and M_m respectively. Then, substituting Eq.4.47 into Eq.4.49 and using Eq.4.48 yields the final expression for $[\mathbf{m}_o]_{R_B}$, namely

$$\begin{aligned}[\mathbf{m}_o]_{R_B} =& [\mathbf{p}]_{R_B} + \mathbf{B}_{P/B}[\mathbf{m}_m]_{R_P} \\ &+ \mathbf{B}_{C/P}\mathbf{B}_{P/B}([\mathbf{m}_o]_{R_C} - [\mathbf{m}_m]_{R_C})\end{aligned} \tag{4.50}$$

where all quantities are known. The desired pose is sent to the IKP block that provides the corresponding angles for the motors. Then, the previous control method is applied for a closed-loop control of the angles of the motors with the encoders. The vision-guided control mode can be used to provide a very effective assistance to the human operator.

4.10 Multimedia Material

The implementation of the algorithms discussed above is presented in a video. The video can be found at : [Video hosted on Youtube] (clickable link, if it does not work, enter the URL : $https://youtu.be/25f1Rli_Q5U$). The first part of the video shows the position control discussed in Section 4.9.1 through pick&place type trajectories and a circular trajectory.

Then, the hybrid control is presented, manipulation of the end-effector with hands illustrates the backdriveable property of the robot. Moreover, pulling the end-effector in a direction produces a return motion followed by a back-and-forth around a neutral configuration, which illustrates the spring-like behaviour expected regarding the control scheme discussed in Section 4.9.2. The robot is mounted on a passive mechanism to simulate the remote aspect of the assembly task set in this context. The passive mechanism allows the three translations as well as one rotation close to the base of the robot, control with a pulley-driving belt that enables the human operator to control the rotation from afar. The passive mechanism also act as a weight support, reducing greatly the weight the human operator feels, at the cost of added inertia. A first peg-in-hole type insertion test follows to show that the compliance of the robot already helps the human operator in achieving the task. Afterwards, the target pose of the robot is change from a fixed pose to a spiral trajectory with a constant orientation. The idea is to introduce a search strategy to the robot, similar to the work in Matsuno et al. (2004), to ease the search of the hole. However, albeit the following test shows some kind of help, the context is here different than in Matsuno et al. (2004). Indeed, the base of the robot is not fixed, the robot does not work by itself but in collaboration with a human operator, making search trajectories inconsistent because if the human operator moves the base before the robot has finished searching, it is impossible to guarantee the work area is correctly explored. The search trajectory can even go against the intent of the human operator, making this strategy a potential detriment for him. Then, the different parameters of the model are changed to explore the flexibility of the robot as a configurable RCC over the fixed-by-design passive alternative. A model with the centre of rotation set 15 centimetres below the end-effector is shown first, then the centre of rotation is set 15 centimetres above the end-effector. To illustrate that the centre of rotation can be placed everywhere, it is place in the plane of the effector, shifted on the side upwards. The behaviour of the robot in an insertion scenario is then compared with the centre of rotation below and above the end-effector. The fundamental benefit of RCC mechanisms is to set the centre of rotation further in front of the tool, to obtain an alignment change produced by the reaction force between the parts favourable for the insertion. The alignment change is generally unfavourable is the centre of rotation is below, despite being the easiest behaviour to design, and make orientation a challenge in assembly tasks. The close-up views in the video shows this phenomenon, despite the robot is not specifically designed to perform this task, with a centre of rotation set below, the peg does not align correctly when touching the surface, whereas with a centre of rotation above, the peg aligns itself correctly. However, the design of this robot is not ideal for large orientation changes, this control strategy would work better with a different architecture.

The last part of the video deals with the vision control scheme discussed in 4.9.3. The robot attempts to reach a pose defined in the frame of the camera, which would be a pose required to perform an assembly task correctly. This target position is set in the centre of the camera at a 55 centimetres distance from the optical centre for the test. The workspace of the robot is fixed

in a constant orientation and constrained in a 10 centimetres diameter sphere in the control to avoid bad configurations. The introduction of changes in orientation as well as optimization of the workspace would greatly increase the task of implementing this control scheme. One can notice if the robot is pulled or pushed too much, the spherical constraint prevent it to reach the target position. The robot follows a trajectory in the direction of the constantly changing target objective in the frame of the robot with a Cartesian velocity limitation. Two different velocity limitations are presented. The higher the speed limit, the faster the accuracy correction on paper, however, this parameter requires to reconsider the regulation parameters of the PID to keep the robot efficient. The last segment of the video emphasizes the planar correction to see clearly the behaviour of the robot in the camera feed.

4.11 Conclusion

In this article, a novel 6-dof parallel robot designed to work in a collaborative environment is presented. The kinematics of the robot are introduced, then a numerical algorithm is used to compute the geometrical workspace of the robot. The singularities of the robot are discussed, followed by an analysis of its force capabilities. A prototype is then presented that implements the characteristics previously discussed. Finally, three control schemes are proposed, each for different application purposes.

4.12 Bibliographie

Albertus Hendrawan Adiwahono, Billy Saputra, Tai Wen Chang, and Zhi Xiang Yong. Autonomous stair identification, climbing, and descending for tracked robots. In *Control Automation Robotics & Vision (ICARCV), 2014 13th International Conference on*, pages 48–53. IEEE, 2014.

Rafiq Ahmad and Peter Plapper. Safe and automated assembly process using vision assisted robot manipulator. *Procedia CIRP*, 41 :771–776, 2016.

Patricia Ben-Horin and Moshe Shoham. Application of grassmann—cayley algebra to geometrical interpretation of parallel robot singularities. *The International Journal of Robotics Research*, 28(1) :127–141, 2009.

Ilian A Bonev and Jeha Ryu. Orientation workspace analysis of 6-dof parallel manipulators. In *Proceedings of the ASME*, pages 1–8, 1999.

Alexandre Campeau-Lecours, Pierre-Luc Belzile, Thierry Laliberté, Simon Foucault, Boris Mayer-St-Onge, Dalong Gao, and Clément Gosselin. An articulated assistive robot for intuitive hands-on-payload manipulation. *Robotics and Computer-Integrated Manufacturing*, 48 :182–187, 2017.

Kevin Cleary and Tatsuo Arai. A prototype parallel manipulator : Kinematics, construction, software, workspace results, and singularity analysis. In *Proceedings. 1991 IEEE International Conference on Robotics and Automation*, pages 566–567. IEEE Computer Society, 1991.

Iman Ebrahimi, Juan A Carretero, and Roger Boudreau. 3-prrr redundant planar parallel manipulator : Inverse displacement, workspace and singularity analyses. *Mechanism and Machine Theory*, 42(8) :1007–1016, 2007.

Denis J Evans. On the representatation of orientation space. *Molecular physics*, 34(2) :317–325, 1977.

Jaime Gallardo-Alvarado, José María Rico-Martínez, and Gürsel Alici. Kinematics and singularity analyses of a 4-dof parallel manipulator using screw theory. *Mechanism and Machine Theory*, 41(9) :1048–1061, 2006.

Zhen Huang, LH Chen, and YW Li. The singularity principle and property of stewart parallel manipulator. *Journal of Robotic Systems*, 20(4) :163–176, 2003.

Arvid QL Keemink, Herman van der Kooij, and Arno HA Stienen. Admittance control for physical human–robot interaction. *The International Journal of Robotics Research*, 37(11) : 1421–1444, 2018.

Doik Kim, Wankyun Chung, and Youngil Youm. Singularity analysis of 6-dof manipulators with the analytical representation of the determinant. In *Proceedings 1999 IEEE International Conference on Robotics and Automation (Cat. No. 99CH36288C)*, volume 2, pages 889–894. IEEE, 1999.

Xianwen Kong and Clement M Gosselin. Kinematics and singularity analysis of a novel type of 3-crr 3-dof translational parallel manipulator. *The International Journal of Robotics Research*, 21(9) :791–798, 2002.

Jörg Krüger, Terje K Lien, and Alexander Verl. Cooperation of human and machines in assembly lines. *CIRP annals*, 58(2) :628–646, 2009.

Pascal D Labrecque, Thierry Laliberte, Simon Foucault, Muhammad E Abdallah, and Clement Gosselin. uman : A low-impedance manipulator for human-robot cooperation based on underactuated redundancy. *IEEE/ASME Transactions on Mechatronics*, 2017.

Ming-Chuan Leu and DK Pai. Genericity and singularities of robot manipulators. 1992.

Guanfeng Liu, Yunjiang Lou, and Zexiang Li. Singularities of parallel manipulators : A geometric treatment. *IEEE Transactions on Robotics and Automation*, 19(4) :579–594, 2003.

Guilin Liu, Zhonghua Xi, and Jyh-Ming Lien. Nearly convex segmentation of polyhedra through convex ridge separation. *Computer-Aided Design*, 78 :137–146, 2016.

David G Lowe. Distinctive image features from scale-invariant keypoints. *International journal of computer vision*, 60(2) :91–110, 2004.

Greg R Luecke, Kok-Leong Tan, and Sean Mahrt. Control of lift assist devices for performance enhancement. In *Mobile Robots XV and Telemanipulator and Telepresence Technologies VII*, volume 4195, pages 260–272. International Society for Optics and Photonics, 2001.

Takayuki Matsuno, Toshio Fukuda, and Yasuhisa Hasegawa. Insertion of long peg into tandem shallow hole using search trajectory generation without force feedback. In *IEEE International Conference on Robotics and Automation, 2004. Proceedings. ICRA'04. 2004*, volume 2, pages 1123–1128. IEEE, 2004.

James Mure-Dubois and Heinz Hügli. Embedded 3d vision system for automated micro-assembly. In *Two-and Three-Dimensional Methods for Inspection and Metrology IV (Proceedings of SPIE)*, volume 6382, pages 1–11. International Society for Optical Engineering (SPIE), 2008.

SM Mizanoor Rahman, Ryojun Ikeura, and Haoyong Yu. Novel biomimetic control of a power assist robot for horizontal transfer of objects. In *Robotics and Biomimetics (ROBIO), 2011 IEEE International Conference on*, pages 2181–2186. IEEE, 2011.

Jun Rekimoto. Matrix : A realtime object identification and registration method for augmented reality. In *Proceedings. 3rd Asia Pacific Computer Human Interaction (Cat. No. 98EX110)*, pages 63–68. IEEE, 1998.

Ethan Rublee, Vincent Rabaud, Kurt Konolige, and Gary Bradski. Orb : An efficient alternative to sift or surf. In *2011 International conference on computer vision*, pages 2564–2571. Ieee, 2011.

J Kenneth Salisbury and John J Craig. Articulated hands : Force control and kinematic issues. *The International journal of Robotics research*, 1(1) :4–17, 1982.

KJ Waldron, Shih-Liang Wang, and SJ Bolin. A study of the jacobian matrix of serial manipulators. 107(2) :230–237, 1985.

Daniel E Whitney. Quasi-static assembly of compliantly supported rigid parts. *Journal of Dynamic Systems, Measurement, and Control*, 104(1) :65–77, 1982.

Fuzhen Zhang. Quaternions and matrices of quaternions. *Linear algebra and its applications*, 251 :21–57, 1997.

Yongjie Zhao. Singularity, isotropy, and velocity transmission evaluation of a three translational degrees-of-freedom parallel robot. *Robotica*, 31(2) :193, 2013.

Conclusion

Le projet de cette thèse était de concevoir des robots collaboratifs pour l'assemblage de pièces à distance. Dans un premier temps, les efforts se sont concentrés sur des mécanismes passifs, plus simples mais plus limités dans leurs possibilités. Certaines tâches d'assemblage ont été sélectionnées et analysées. L'objectif était de mieux comprendre comment elles fonctionnent, acquérir des données importantes en vue des futures étapes de conception et déterminer de quelles façons il est possible de répondre à la problématique. Le premier objectif dans la conception d'un mécanisme d'aide à l'accomplissement d'une tâche est que ce dernier soit en mesure d'accomplir la tâche en partie ou totalement par lui-même. L'étude des snap-fit a mené à la conception de l'impacteur, décrit dans la partie 1. Les retours provenant de personnes travaillant sur les chaînes d'assemblage indiquaient que ces tâches étaient plus faciles à réaliser à l'aide d'impacts. L'idée principale derrière la conception de l'impacteur était de pouvoir générer des impacts avec un certain contrôle sur la fréquence et l'amplitude de ces derniers. Utilisé manuellement, l'impacteur permet de transformer un effort mieux réparti dans le temps tout en générant les impacts utiles pour l'assemblage. Mais l'impacteur a aussi été conçu pour être facilement équipé d'un moteur qui fournit alors la puissance de travail nécessaire, comme montré à la fin des démonstrations de la partie 2. Les tuyaux ont été traités différemment des snap-fit. Lors des phases d'observation, ces derniers se sont révélés avoir un comportement bien plus complexe et imprévisible que les snap-fit, des étapes supplémentaires d'observation ont alors été planifiées. La partie 1 montre des recherches concernant la potentielle utilisation de mouvements spécifiques lors de l'insertion d'un tuyau. Des mécanismes vibrants ont aussi été étudié. Les mouvements spécifiques se sont révélés intéressants mais leur introduction dans un mécanisme a été jugée trop ambitieuse pour le temps alloué au projet. Les vibrations, quant à elles, supposées intéressantes par la recherche bibliographique, se sont révélées décevantes lors des mesures.

La seconde problématique était de répondre au besoin de conserver la tâche simple et rapide bien qu'elle s'exécute désormais de loin. La principale difficulté identifiée pour conserver la performance de l'opérateur était que ce dernier manque de précision lorsqu'il se trouve loin de la zone d'assemblage. Soit il échoue, soit il a besoin d'un temps supplémentaire pour accomplir la tâche, temps précieux pour conserver une production efficace sur les chaînes d'assemblage. La suite du projet a donc porté sur les mécanismes permettant de pallier le manque de précision

lors d'un assemblage. Le mécanisme existant le plus connu dans ce domaine est le RCC, il servit donc de base à la suite de l'étude. Différents mécanismes furent explorés, comme montrés dans la partie 2. Le RCC possède une faiblesse majeure, il ne fonctionne que sur une plage de correction très restreinte. Cette faiblesse est en général contrebalancée par le fait qu'il est utilisé avec des robots, déjà très précis de base, son action se limite donc à une très légère, mais tout de même très utile, correction en position et angle. Cependant, dans un contexte de travail avec un humain, les erreurs de pose attendues sont bien plus importantes qu'avec un robot et donc l'architecture classique du RCC se révèle inadaptée. La limite de fonctionnement du RCC se situe principalement dans le fait que le centre de rotation qu'il introduit ne reste pas au même endroit s'il est sujet à des déplacements trop importants. Le mécanisme proposé dans la partie 2 a donc pour particularité d'introduire un centre de rotation fixe, la plage de fonctionnement est donc considérablement augmentée. Cependant, des contraintes de temps ont obligé la conception du prototype à se concentrer sur une correction uniquement en position et non en orientation. Le prototype présenté possède une architecture plus simple, mais sa fabrication a induit un certain nombre de défis tels que la transmission des efforts d'impact, le maintien efficace de la pièce à insérer et la résistance du mécanisme aux impacts nécessaires à l'assemblage.

Le correcteur de précision passif est un mécanisme intéressant, mais comme prévu, il est limité dans son usage. La suite du projet a donc porté sur la conception d'un mécanisme actif, qui pourrait être utilisé de différentes façons, notamment grâce à des ajustements sur son schéma de contrôle. La grande liberté permise dans la conception de ce robot a mené à l'étude de plusieurs architectures potentielles. Ces études ont produit l'analyse présentée dans la partie 3. L'analyse de ce robot permettait de résoudre des problèmes géométriques intéressants et utiles pour la suite du projet. La méthode d'estimation de l'espace de travail, de la détermination des lieux de singularité ainsi que des capacités en effort du robot ont d'ailleurs été réutilisées pour la conception du robot présenté dans la partie 4.

La partie 4 présente le robot correcteur de position actif. Les étapes de conception sont présentées, puis une attention particulière est dédiée aux schémas de contrôle du robot. Un contrôle en position classique est présenté comme base de contrôle du robot, puis les concepts discutés lors de l'élaboration du mécanisme passif sont introduits. Le second schéma de contrôle simule le comportement d'un RCC, tout en apportant la possibilité d'être reconfigurable a volonté sans modification matérielle. Ce schéma de contrôle est alors testé pour des cas d'assemblage de type 'peg-in-hole', qui sont les assemblages classiques pour l'usage d'un RCC. Le dernier schéma de contrôle explore le fonctionnement conjoint du robot avec un système de vision. Une caméra est introduite dans le modèle et permet une correction de position en se servant des informations sur l'environnement recueillies par la caméra. Ce test montre de quelle façon un tel robot pourrait être inclus dans un contexte réaliste.

Les différentes étapes résumées ici ont permis de concevoir des mécanismes qui proposent

des solutions potentielles au problème de l'assemblage efficace de pièce à distance sur une chaîne d'assemblage. Les différentes solutions présentées ici ne sont pas parfaites, mais elles alimentent les discussions sur ce type de problème et pourraient aider à concevoir des solutions industrielles.

Annexe A

Annexes de l'aricle 3 : KINEMATIC AND WORKSPACE MODELLING OF A 6-PUS PARALLEL MECHANISM

Appendix A : Determination of the parametric form an ellipse from its implicit form

The general implicit form of the ellipse can be written as :

$$ax^2 + by^2 + cxy + dx + ey = f \tag{A.1}$$

where a, b, c, d, e and f are constant parameters. Factoring this expression to isolate y in one member leads to :

$$(\sqrt{a}x + \frac{cy+d}{2\sqrt{a}})^2 + (B_1 y + B_0)^2 = R \tag{A.2}$$

where :

$$B_0 = \frac{1}{2\sqrt{b - \frac{c^2}{4a}}}(e - \frac{cd}{2a}) \tag{A.3}$$

$$B_1 = \sqrt{b - \frac{c^2}{4a}} \tag{A.4}$$

$$R = f + \frac{d^2}{4a} + \frac{(e - \frac{cd}{2a})}{4(b - \frac{c^2}{4a})}. \tag{A.5}$$

The parameter θ is then introduced to get the typical parametric form of an ellipse. Therefore

$$\sqrt{R}\cos\theta = \sqrt{a}x + \frac{cy+d}{2\sqrt{a}} \tag{A.6}$$

$$\sqrt{R}\sin\theta = B_1 y + B_0 \tag{A.7}$$

which is then substituted in Eqn. (A.2) to yield

$$y = \frac{\sqrt{R}}{B_1}\sin\theta - \frac{B_0}{B_1} \tag{A.8}$$

$$x = \sqrt{\frac{R}{a}}\cos\theta - \frac{\sqrt{R}}{B_1}\frac{c}{2B_1}\sin\theta - \frac{d}{2a} + \frac{cB_0}{2aB_1}. \tag{A.9}$$

For a better numerical accuracy, if the absolute value of parameter b is larger than the absolute value of parameter a, another solution obtained by isolating x instead of y can be more appropriate. In the end, the ellipse is described in the following general parametric form :

$$x(\theta) = C_x\cos\theta + S_x\sin\theta + K_x \tag{A.10}$$

$$y(\theta) = C_y\cos\theta + S_y\sin\theta + K_y. \tag{A.11}$$

Appendix B : Solution of the intersection of a straight line with an ellipse

The chosen representation of the ellipse is the parametric form from Eqn. (A.10) and Eqn. (A.11). The description of the line is :

$$ax + by + c = 0 \tag{A.12}$$

In our case the line comes from the intersection of two planes. The first plane is defined by a normal vector $\mathbf{u} = [u_1, u_2, u_3]^T$ and a point P_{ref}. The second plane is defined by its third component being constant ($z = Z_c$) so that the equation for the line is

$$\mathbf{u}^T(P - P_{ref}) = 0 \tag{A.13}$$

$$u_1 x + u_2 y + u_3 Z_c - \mathbf{u}^T P_{ref} = 0 \tag{A.14}$$

Substituting the parametric form of the ellipse given in Eqn. (A.10) and Eqn. (A.11) into Eqn. (A.12) leads to :

$$(aC_x + bC_y)\cos\theta + (aS_x + bS_y)\sin\theta + (c + aK_x + bK_y) = 0 \tag{A.15}$$

Using the well known trigonometric substitutions

$$\cos\theta = \frac{1-t^2}{1+t^2} \tag{A.16}$$

$$\sin\theta = \frac{2t}{1+t^2} \tag{A.17}$$

where $t = \tan\frac{\theta}{2}$, gives a polynomial equation of degree 2 in t, namely

$$(c + aK_x + bK_y - aC_x - bC_y)t^2 + 2(aS_x + bS_y)t + (c + aK_x + bK_y + aC_x + bC_y) = 0 \quad \text{(A.18)}$$

Solving this equation for t tells if there exist angles in the parametric form of the ellipse where the line intersects and provides the corresponding values.